博士論文

Unusual antiferromagnetic order and *c* - *f* hybridization gap in the Kondo semiconductor $CeOs_2Al_{10}$

近藤半導体 $CeOs_2Al_{10}$ の
特異な反強磁性秩序と *c* - *f* 混成ギャップ

川端　丈

広島大学大学院先端物質科学研究科

2017 年 9 月

目次

１．主論文

Unusual antiferromagnetic order and *c-f* hybridization gap
in the Kondo semiconductor $CeOs_2Al_{10}$
（近藤半導体 CeT_2Al_{10} の特異な反強磁性秩序と *c-f* 混成ギャップ）
川端　丈

２．公表論文

(1) Doping effects on the hybridization gap and antiferromagnetic order in the Kondo semiconductor $CeOs_2Al_{10}$ studied by break-junction experiments,
J. Kawabata, T. Ekino, Y. Yamada, Y. Okada, A. Sugimoto, Y. Muro, and T. Takabatake,
Physical Review B **95**, 035144 /1-9 (2017)

(2) Interplay between hybridization gaps and antiferromagnetic gap in the hole-doped Kondo semiconductor $Ce(Os_{1-y}Re_y)_2Al_{10}$,
J. Kawabata, T. Ekino, Y. Yamada, A. Sugimoto, Y. Muro, and T. Takabatake,
Journal of Physics: Conference Series **807**, 012008 /1-6 (2017).

(3) Hybridization gaps and antiferromagnetic gap in the Kondo semiconductors CeT_2Al_{10} (T = Fe and Os) observed by break-junction tunneling spectroscopy,
J. Kawabata, T. Ekino, Y. Yamada, Y. Sakai, A. Sugimoto, Y. Muro, and T. Takabatake,
Physical Review B **92**, 201113(R) /1-5 (2015).

(4) Suppression of antiferromagnetic order and hybridization gap by electron and hole doping in the Kondo semiconductor $CeOs_2Al_{10}$,
J. Kawabata, T. Takabatake, K. Umeo, and Y. Muro,
Physical Review B **89**, 094404 /1-7 (2014).

(5) Transition from a Kondo semiconducting antiferromagnet to a heavy-fermion antiferromagnet in $Ce(Os_{1-x}Ir_x)_2Al_{10}$,
J. Kawabata, K. Yutani, K. Umeo, T. Takabatake, and Y. Muro,
Journal of Physical Society Conference Proceedings **3**, 012023 /1-6 (2014).

３．参考論文

(1) Uniaxial pressure effects on the unusual antiferromagnetic transition in the Kondo semiconductor $CeOs_2Al_{10}$,
K. Hayashi, K. Umeo, Y. Yamada, J. Kawabata, Y. Muro, and T. Takabatake,
Journal of Physics: Conference Series **807**, 022002 /1-6 (2017).

(2) Dilution effects on the antiferromagnetic Kondo semiconductor $CeOs_2Al_{10}$,
Y. Okada, J. Kawabata, Y. Yamada, Y. Muro, and T. Takabatake,
Journal of Physics: Conference Series **807**, 022003 /1-5 (2017).

(3) Doping effects on the electronic structure of an anisotropic Kondo semiconductor $CeOs_2Al_{10}$: An optical study with Re and Ir substitution,
S. Kimura, H. Takao, J. Kawabata, Y. Yamada, and T. Takabatake,
Journal of the Physical Society of Japan **85**, 123705 /1-4 (2016).

(4) Effect of Si substitution on the antiferromagnetic ordering in the Kondo semiconductor $CeRu_2Al_{10}$,
K. Hayashi, Y. Muro, T. Fukuhara, J. Kawabata, T. Kuwai, and T. Takabatake,
Journal of the Physical Society of Japan **85**, 034714 /1-4 (2016).

(5) Contrasting effect of La substitution on the magnetic moment direction in the Kondo semiconductors CeT_2Al_{10} (T = Ru, Os),
D. T. Adroja, A. D. Hillier, C. Ritter, A. Bhattacharyya, D. D. Khalyavin, A. M. Strydom, P. Peratheepan, B. Fåk, M. M. Koza, J. Kawabata, Y. Yamada, Y. Okada, Y. Muro, T. Takabatake, and J. W. Taylor,
Physical Review B **92**, 094425 /1-10 (2015).

(6) Anisotropic thermopower of the antiferromagnetic Kondo semiconductor $CeOs_2Al_{10}$ doped with 5d electrons and holes,
Y. Yamada, J. Kawabata, T. Onimaru, and T. Takabatake,
Journal of the Physical Society of Japan **84**, 084705 /1-5 (2015).

(7) Anisotropic chemical pressure effect on the antiferromagnetic Kondo semiconductor $Ce(Ru_{1-x}Fe_x)_2Al_{10}$,
K. Hayashi, Y. Muro, T. Fukuhara, T. Kuwai, J. Kawabata, and T. Takabatake,
Physics Procedia **75**, 121-126 (2015).

(8) Contrasting carrier doping effects in the Kondo insulator $CeOs_2Al_{10}$: The influential role of *c-f* hybridization in spin-gap formation,
A. Bhattacharyya, D. T. Adroja, A. M. Strydom, J. Kawabata, T. Takabatake, A. D. Hillier, V. G. Sakai, J. W. Taylor, and R. I. Smith,
Physical Review B **90**, 174422 /1-9 (2014).

(9) Effects of Ga and Si substitutions for Al in $CeRu_2Al_{10}$ on the unusual antiferromagnetic order in the Kondo semiconducting state,
Y. Muro, K. Hida, T. Fukuhara, J. Kawabata, K. Yutani, and T. Takabatake,
Journal of Physical Society Conference Proceedings **3**, 012017 /1-7 (2014).

(10) Magnetic ordering with reduced cerium moments in hole-doped $CeOs_2Al_{10}$,
D. D. Khalyavin, D. T. Adroja, A. Bhattacharyya, A. D. Hillier, P. Manuel, A. M. Strydom, J. Kawabata, and T. Takabatake,
Physical Review B **89**, 064422 /1-5 (2014).

(11) Change of magnetic ground state by light electron doping in $CeOs_2Al_{10}$,
D. D. Khalyavin, D. T. Adroja, P. Manuel, J. Kawabata, K. Umeo, T. Takabatake, and A. M. Strydom,
Physical Review B **88**, 060403(R) /1-4 (2013).

主論文

Unusual antiferromagnetic order and c-f hybridization gap in the Kondo semiconductor $CeOs_2Al_{10}$

[近藤半導体$CeOs_2Al_{10}$の特異な反強磁性秩序とc-f混成ギャップ]

Jo Kawabata

Department of Quantum Matter
Graduate School of Advanced Sciences of Matter
Hiroshima University

March, 2017

Abstract

Most cerium-based intermetallic compounds exhibit Kondo effects in the physical properties and thus are described as Kondo-lattice systems where conduction electrons hybridize with the $4f$ states. A small number of Kondo-lattice systems possess a narrow gap in the c-f hybridized bands at the Fermi level $E_{\rm F}$. They are called as Kondo semiconductors (KSs) exemplified by CeNiSn, CeRhSb, CeRhAs, and $Ce_3Bi_4Pt_3$. Neither of them ordered magnetically as the Ce moments are quenched at low temperatures by the strong c-f hybridization.

A new family of compounds CeT_2Al_{10} (T = Fe, Ru, and Os) with the orthorhombic $YbFe_2Al_{10}$-type structure have been classified into the KSs because the electrical resistivity exhibits the thermal activation behavior, $\rho(T) \propto \exp(\Delta/2k_{\rm B}T)$. The compounds with T = Ru and Os, however, undergo antiferromagnetic (AFM) transitions at $T_{\rm N}$ = 27.0 and 28.5 K, respectively. Here, it raised a question of why the $T_{\rm N}$s for CeT_2Al_{10} with small ordered magnetic moments of $\mu_{\rm AF}$ = 0.3 – 0.4 $\mu_{\rm B}$/Ce are higher than that for the Gd counterparts with 7 $\mu_{\rm B}$/Gd. Furthermore, the magnetic moments are aligned along the c axis although the magnetic susceptibility is largest for $B \parallel a$ in the paramagnetic region.

In the present work, we aimed at understanding the mechanism of the unusual AFM order in CeT_2Al_{10} (T = Ru and Os). The comparison of the magnetic and thermal properties between T = Ru and T = Os indicated that the system with T = Os is located closer to the critical point where the unusual AFM order disappears. Therefore, we have selected $CeOs_2Al_{10}$ for our systematic studies. We have substituted La for Ce, Re and Ir for Os in $CeOs_2Al_{10}$, and measured the magnetic, transport, and thermal properties as well as the differential conductances.

The lattice parameters of the alloys in $Ce_{1-z}La_zOs_2Al_{10}$, $Ce(Os_{1-y}Re_y)_2Al_{10}$, and $Ce(Os_{1-x}Ir_x)_2Al_{10}$ do not change more than 0.3 % for $z \leq 1.0$, $2y \leq 0.2$, and $2x \leq$

0.3. Therefore, the effects of $4f/5d$ holes and $5d$ electrons doping in $CeOs_2Al_{10}$ may be much stronger than the chemical pressure effect. The doped $4f$-hole content is z in $Ce_{1-z}La_zOs_2Al_{10}$ whereas the $5d$ hole and $5d$ electron contents are $2y$ and $2x$ in $Ce(Os_{1-y}Re_y)_2Al_{10}$ and $Ce(Os_{1-x}Ir_x)_2Al_{10}$, respectively.

The magnetization and neutron scattering measurements have revealed that the doping of $4f/5d$ holes and $5d$ electrons differently alter the $4f$ electron state in $CeOs_2Al_{10}$. In $Ce_{1-z}La_zOs_2Al_{10}$, both the effective magnetic moment and paramagnetic Currie temperature θ_P hardly depend on z up to 0.51, indicating the unchanged $4f$ state at high temperatures. With increasing $2y$ in $Ce(Os_{1-y}Re_y)_2Al_{10}$, a broad maximum in $\chi_a(T)$ at around 45 K decreases and disappears at $2y = 0.1$. The magnitude of μ_{AF} decreases from 0.3 μ_B/Ce for $2y = 0$ to 0.18 μ_B/Ce for $2y = 0.06$. These decreases mean that the doping of $5d$ holes leads the $4f$ electron state to be delocalized. The doping of $4f/5d$ holes in $CeOs_2Al_{10}$ maintain the direction of μ_{AF} along c axis. With increasing $2x$ in $Ce(Os_{1-x}Ir_x)_2Al_{10}$, by contrast, the maximum in $\chi_a(T)$ at 45 K changes to a sharp peak with the fivefold increase in the height. For $2x = 0.16$, the direction of μ_{AF} is reoriented form the c-axis to the a-axis in concomitant with the increase of μ_{AF} to 1.0 μ_B/Ce. These changes originate from the localization of the $4f$ state caused by doping $5d$ electrons in $CeOs_2Al_{10}$. Despite of the large increase in μ_{AF}, T_N decreases from 28.5 K for $2x = 0$ to 7.0 K for $2x = 0.3$. The opposite changes in μ_{AF} and T_N with respect to $2x$ suggest that the inter-site AFM interaction between Ce moments depends on neither the magnitude nor direction of μ_{AF} with respect to the crystal axis.

As described above, the $4f/5d$-holes and $5d$-electron doping in $CeOs_2Al_{10}$ changes the c-f hybridization in very different ways. Nevertheless, in all doped systems, the decrease in the transport gap Δ above T_N is well correlated with the increase in the γ value of the specific heat C. This relation indicates that the development of in-gap states at E_F destroys the transport gap. Furthermore, we found the simultaneous suppression of T_N and Δ, suggesting the transport gap to be necessary for the AFM order at unusually high T_N. However, the C/T data for the samples with $z = 0.2$ and $2x = 0.3$ exhibit weak magnetic anomalies at 11.6 and 7.0 K, respectively, although the thermal activation-type behaviors in $\rho(T)$ are no longer observed. Such a change into metallic behavior can be attributed to the appearance of mobile carriers in the in-gap states. The residual

density of states at $E_{\rm F}$, $N(E_{\rm F})$, makes it difficult to judge the presence of hybridization gap from the resistivity data. The thermopower $S(T)$ is in general very sensitive to the energy dependence of the quasiparticle density of states $N(E)$ at the chemical potential. For $CeOs_2Al_{10}$, $S(T)$ only along the b axis bends at $T_{\rm S}$ = 36 K. It evokes a question why S_b decreases above $T_{\rm N}$. Therefore, we have performed the BJTS study of CeT_2Al_{10} (T = Fe, Ru, and Os) and La-, Re-, and Ir- substituted $CeOs_2Al_{10}$ because the break-junction tunneling spectroscopy (BJTS) may provide us with more direct information on the temperature dependences of the gap width and $N(E_{\rm F})$.

The differential conductances of CeT_2Al_{10} (T = Fe, Ru, and Os) have shown the development of two successive gaps V_1 and V_2 on cooling. We found that the gap widths at 4.4 K are well scaled by the Kondo temperature $T_{\rm K}$ among the Ce-based Kondo semiconductors with orthorhombic structures. The scaling implies that V_1 and V_2 are c-f hybridization gaps. For the three compounds, the values of zero-bias conductance [ZBC = $dI/dV(V = 0)$] are finite, confirming the residual $N(E_{\rm F})$. The ZBC is known to be proportional to the square of $N(E_{\rm F})$. The ZBCs for T = Ru and Os bend downward on cooling below T^* = 28 and 36 K ($> T_{\rm N}$), respectively, whose temperature agree with the bending temperature $T_{\rm S}$ in $S_{\rm b}$. Below $T_{\rm N}$, another gap $V_{\rm AF}$ opens, whose magnitude in $CeRu_2Al_{10}$ with $T_{\rm N}$ = 27.0 K is 30 % smaller than that in $CeOs_2Al_{10}$ with $T_{\rm N}$ = 28.5 K.

Furthermore, we have studied the doping effect on the three gap structures in $CeOs_2Al_{10}$. As z is increased to z = 0.35 in $Ce_{1-z}La_zOs_2Al_{10}$, $T_{\rm N}$ and transport gap in $\rho(T)$ disappear, while the differential conductance spectrum remains V-shaped. With increasing $2y$ to 0.04 in $Ce(Os_{1-y}Re_y)_2Al_{10}$, by contrast, an upward cusp appears at zero-bias within the gap structures of V_1 and $V_{\rm AF}$. For $2y$ = 0.1, the upward cusp develops further and then all gap structures disappear. A similar cusp appears at the center of the gaps when $2x$ in $Ce(Os_{1-x}Ir_x)_2Al_{10}$ is increased to 0.08, but the upward cusp vanishes for $2x$ = 0.3, keeping the V-shaped gap structure intact. In this manner, the doping of $4f/5d$ holes and $5d$ electrons in $CeOs_2Al_{10}$ changes the spectrum in very different ways. Nevertheless, in all doping cases, the decrease of V_1 is well correlated with those of T^*, $V_{\rm AF}$ and $T_{\rm N}$, and anti-correlated with the increase of $[{\rm NZBC}]^{1/2}$ as functions of z, $2y$, and $2x$. The asymmetric increase in $[{\rm NZBC}]^{1/2}$ with respect to $2y$ and $2x$ resembles that in the γ value. These findings imply that the three different types of doping in $CeOs_2Al_{10}$ create in-gap

states at $E_{\rm F}$, which destroy all gap structures and the AFM transition. Moreover, only in the doping region where V_1 and $V_{\rm AF}$ coexist, we found the significant decrease in the ZBC on cooling below T^* ($> T_{\rm N}$). The T^* decreases by doping of $4f/5d$ holes and $5d$ electron, whose behavior resembles the decrease in $T_{\rm S}$ of S_b. These observations indicate that the unusual AFM order is proceeded by the decrease in $N(E_{\rm F})$ in the presence of hybridization gap.

Contents

Chapter 1

Introduction

1.1 $4f$-electron systems

The lanthaides are a group of elements with atomic numbers from 57(La) to 71(Lu). These fifteen elements along with scandium and yttrium are called rare-earth elements. The lanthanides have different numbers of electrons in the $4f$ shell. The electronic states of the $4f$ electrons give rise to the magnetism in rare-earth based compounds. As shown in Fig. 1.1, the atomic charge density of $4f$ electrons is localized inside the closed $5s$ and $5p$ shells, whose electron states become itinerant in the intermetallic compounds [1]. The amplitude of the $4f$-electron charge density has important consequences for the $4f$ electron states. The tail of charge density in the $4f$ electrons extends to a large distance, making the $4f$-electrons are shielded incompletely. Thereby, the $4f$ electrons hybridize with conduction electrons (c-f hybridization).

The $4f$-electron systems based on Ce and Yb exhibit a large variety of properties such as dense Kondo effect, heavy fermion behavior, valence fluctuation, and semiconducting behavior [2, 3, 4]. Tuning the c-f hybridization in controlled ways by changing composition, applying pressure or magnetic field allows the ground state to change from a long-range magnetically ordered state to a paramagnetic state.

1.2 Magnetic and transport properties of Kondo compounds

1.2.1 Antiferromagnetic compounds

In an antiferromagnetic state, the magnetic moments of atoms align in a regular pattern with neighboring moments pointing in the opposite direction. Figure 1.2 displays the magnetic susceptibilities $\chi_{||}(T)$ and $\chi_{\perp}(T)$ in a typical antiferromagnetic compound [5], where $\chi_{||}(T)$ and $\chi_{\perp}(T)$ stand for the cases with the magnetic field applied parallel and perpendicular direction for the ordered magnetic moments, respectively. Both $\chi_{||}(T)$ and $\chi_{\perp}(T)$ obey the Curie-Weiss law above $T_{\rm N}$, which is the Néel temperature. The Curie-Weiss law is expressed as

$$\chi = \frac{C}{T - \theta_{\rm P}}, \tag{1.1}$$

where $\theta_{\rm P}$ is a paramagnetic Curie temperature and C is a Curie constant, which is given by

$$C = \frac{N_{\rm A}\mu_{\rm eff}^2}{3k_{\rm B}}, \tag{1.2}$$

where $N_{\rm A}$ is Avogadro's number, $k_{\rm B}$ is Boltzmann's constant, and $\mu_{\rm eff}$ is the effective magnetic moment in the unit of $\mu_{\rm B}$, Bohr magneton.

On cooling below $T_{\rm N}$, $\chi_{||}(T)$ drops continuously to the zero, whereas $\chi_{\perp}(T)$ become constant because of the ordered arrangements of moments. For the Ce-based antiferromagnets, however, $\chi(T)$ often shows anomalous temperature dependence due to competing interaction. In CePtSn [6], for example, $\chi(T)$'s along all orthorhombic principal axes decrease below $T_{\rm N} = 7.5$ K (Fig. 1.3).

A magnetization curve as a function of magnetic field, $M(B)$, for a typical antiferromagnet is shown in Fig. 1.4. By applying a magnetic field parallel to the easy magnetization axis, $M(B)$ displays a discontinuous increase at a critical field B_{sf} (metamagnetic transition). The transition is called a spin-flop transition, where the moments of the two sublattice rotate suddenly from the easy magnetization direction to the perpendicular direction. On further increasing B, $M(B)$ increases linearly with a continuous rotation of magnetic moments.

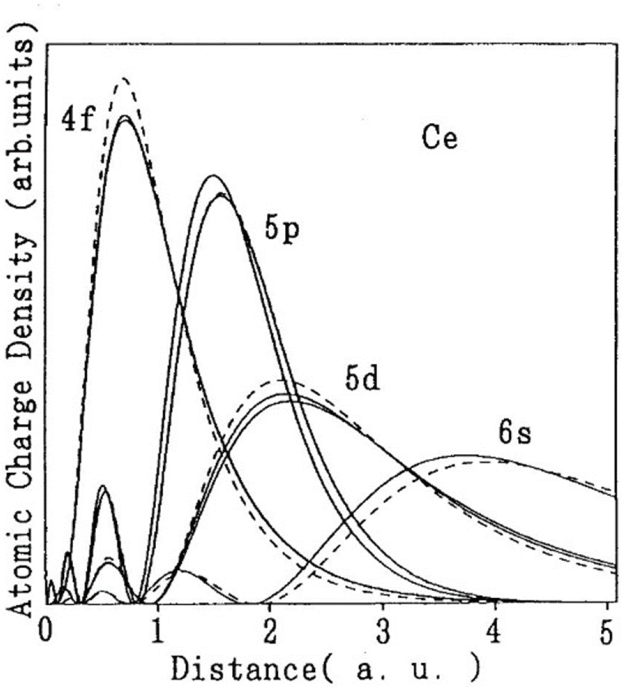

Figure 1.1: The radial components of atomic charge density for Ce with one $4f$ electron [1].

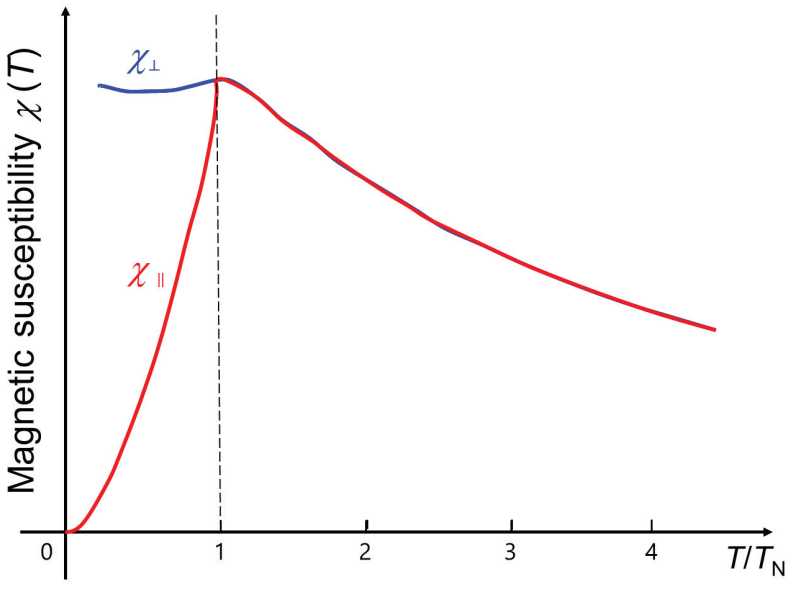

Figure 1.2: Temperature dependence of magnetic susceptibility $\chi(T)$ for a typical antiferromagnet in magnetic field applied parallel and perpendicular to the easy axis [5].

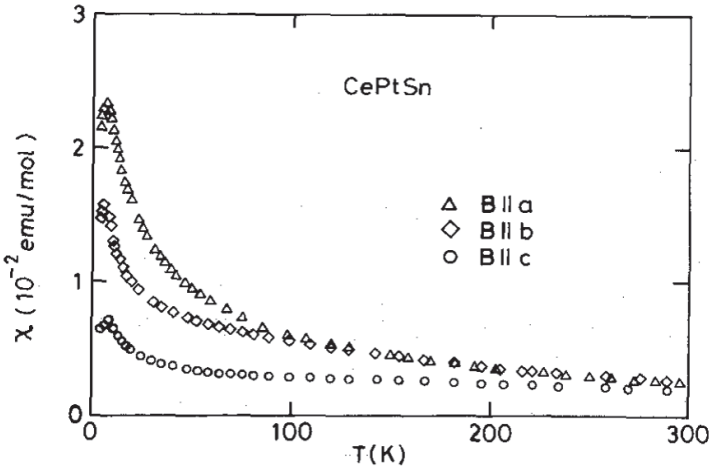

Figure 1.3: Temperature dependence of $\chi(T)$ for the antiferromagnetic Ce compound CePtSn with the orthorhombic structure [6].

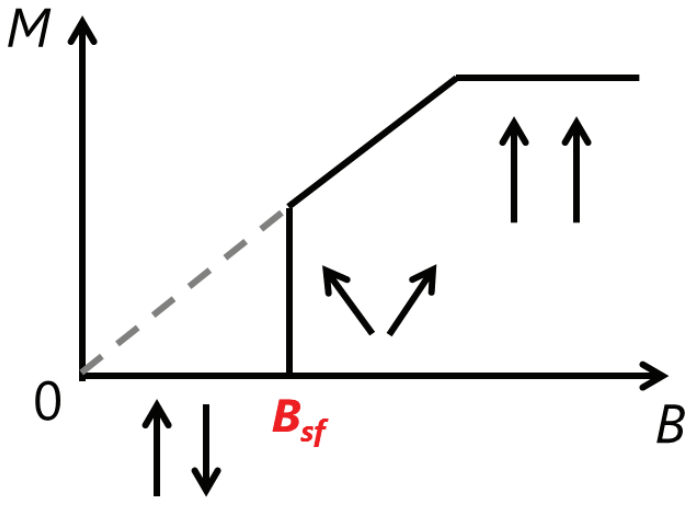

Figure 1.4: Magnetization curve M vs B applied along the easy magnetization axis. The spin-flop transition occurs at $B = B_{\rm sf}$ [5]. The arrows indicate the moments of two sublattices.

1.2.2 RKKY interaction and Kondo effect

RKKY interaction

In rare-earth compounds, an indirect exchange interaction between the localized magnetic moments of $4f$ electrons act via the conduction electrons, which is known as the Ruderman-Kittel-Kasuya-Yosida (RKKY) interaction [1]. This interaction is derived on the assumption that the localized spins in the $4f$ shell interact on site with spin polarization of the conduction band. Figure 1.5 displays the schematic of the RKKY interaction between the localized magnetic moments. A localized magnetic moment on the i^{th} site $\boldsymbol{S}_i$ leads a spin polarization of conduction electrons. The spin polarization interacts with another magnetic moment $\boldsymbol{S}_j$ on the j^{th} site. Therefore, an indirect interaction occurs between the $\boldsymbol{S}_i$ and $\boldsymbol{S}_j$, and leads to a magnetic order in rare-earth compounds. Thereby, the RKKY interaction stabilizes the localized magnetic moment.

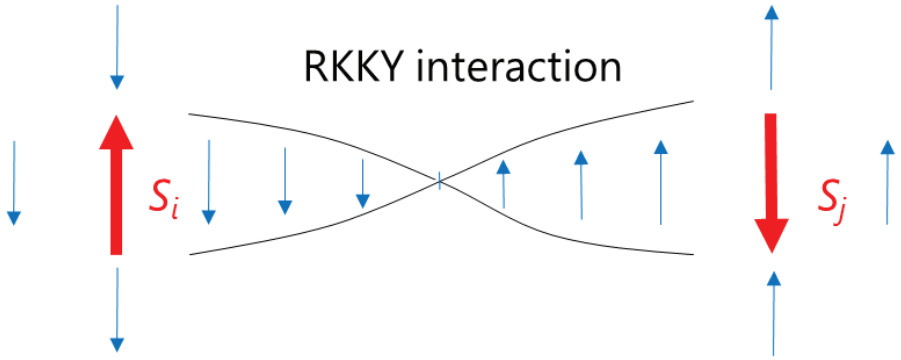

Figure 1.5: Schematic of the RKKY interaction between the localized moments (red arrows) and conduction electrons (blue arrows).

The RKKY interaction between the localized spins is expressed as

$$H_{\text{ff}} = -\sum_{ij} J(R_{ij})\, \boldsymbol{S}_i \cdot \boldsymbol{S}_j, \tag{1.3}$$

$$J(R_{ij}) \propto \frac{-2k_{\text{F}}R_{ij}\cos(2k_{\text{F}}R_{ij}) + \sin(2k_{\text{F}}R_{ij})}{(2k_{\text{F}}R_{ij})^4}, \tag{1.4}$$

where $J(R_{ij})$ is the strength of the RKKY interaction between the localized spins $\boldsymbol{S}_i$ and $\boldsymbol{S}_j$. As shown in Fig. 1.6, $J\ (R_{ij})$ falls off as R_{ij}^3 and oscillates from positive to negative with increasing the distance R_{ij} between neighboring spins (Eq. (1.4)). In rare-earth

compounds, the spin operator is not the good quantum number. Instead, $\boldsymbol{S}_i$ in Eq. (1.3) needs to be replaced by the projection of the total angular momentum $\boldsymbol{J}_i$ to $\boldsymbol{S}_i$ i.e., $(g_J - 1)\,\boldsymbol{J}_i$, where g_J is the Landé g-value. Then, the Hamiltonian of RKKY interaction is given by

$$H_{\rm ff} = -\sum_{ij} (g_J - 1)^2\, J(R_{ij})\, \boldsymbol{J}_i \cdot \boldsymbol{J}_j. \tag{1.5}$$

If the crystal field effect and Kondo effect are neglected, the magnetic transition temperature of a series of RE compounds caused solely by the RKKY interaction can be scaled by the de Gennes factor,

$$dG = (g_J - 1)^2 J(J + 1). \tag{1.6}$$

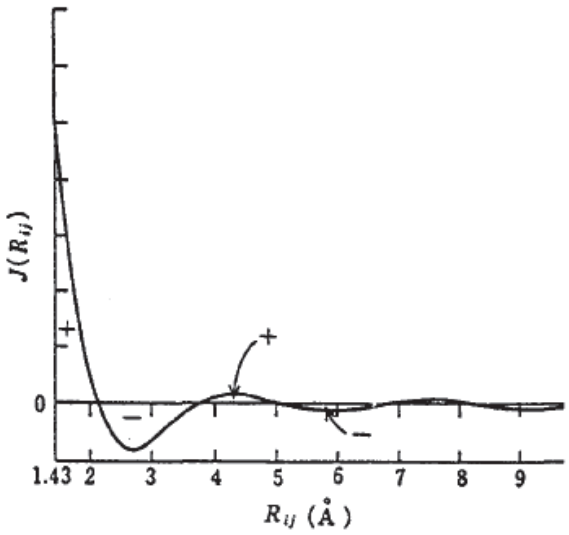

Figure 1.6: The indirect exchange coefficient $J(R_{ij})$ as a function of the distance between neighboring magnetic electrons R_{ij} [1].

Furthermore, the characteristic temperature of the RKKY interaction, $T_{\rm RKKY}$, is expressed as

$$k_{\rm B} T_{\rm RKKY} \propto |J_{cf}|^2 N_c(E_{\rm F}), \tag{1.7}$$

where J_{cf} is the exchange parameter between the $4f$ electron and conduction electrons and $N_c(E_{\rm F})$ is the density of states of conduction electrons at the Fermi energy $E_{\rm F}$. The

c-f exchange interaction J_{cf} is given by

$$J_{cf} \propto \frac{<|V|^2>}{E_F - E_{4f}}, \tag{1.8}$$

where V is the hybridization matrix element and E_{4f} is the $4f$ level. By changing composition of the given compound or applying pressure, the magnitude of J_{cf} can be tuned.

Kondo effect

The existence of localized moments in dilute alloys has an important consequence for the electrical resistivity $\rho(T)$, showing a shallow minimum at low temperatures. The increase at low temperatures is caused by the scattering of conduction electrons by the localized moments. The second-order perturbation of this interaction leads to $-\log T$ increase in $\rho(T)$ with decreasing temperature, as expressed by

$$\rho(T) = \rho_B[1 + 2J_{cf}N_c(E_F)\log\frac{W}{k_B T}], \tag{1.9}$$

where W is the conduction band width. Figure 1.7 represents the temperature variations of the magnetic susceptibility $\chi(T)$, resistance $R(T)$, magnetic specific heat $C_{\rm m}(T)$, and thermopower $S(T)$ [7]. On cooling a Ce dilute system such as La(Ce)B_6 below $T_{\rm K}$ [8], the localized magnetic moment of the Ce ion is screened because the spins of conduction electrons couple antiparallel with the moment of $4f$ electrons. Therefore, $T\chi(T)$ decreases with decreasing T, and a broad maximum appears at a half of $T_{\rm K}$ in both $C_{\rm m}(T)$ and $S(T)$. The Kondo temperature $T_{\rm K}$ is given by

$$k_{\rm B}T_{\rm K} = W\exp\left[\frac{-1}{J_{cf}N_c(E_{\rm F})}\right]. \tag{1.10}$$

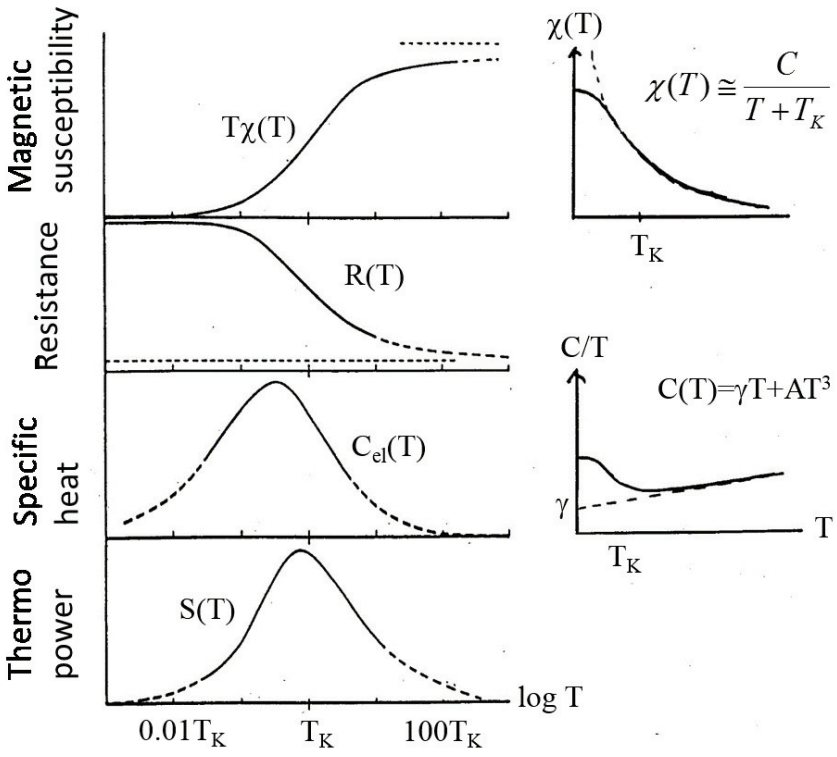

Figure 1.7: Typical Kondo anomalies in the magnetic, transport, and thermal properties [7].

Doniach phase diagram

Magnetic ordering in heavy-fermion compounds is generally influenced by the competition between the RKKY interaction and the Kondo effect. The former stabilizes the localized magnetic moments, while the latter quenches the magnetic moments. As shown in Fig. 1.8, a simple picture for the competition is described by the Doniach phase diagram [9].

In the case of $T_{\rm K} \ll T_{\rm RKKY}$, the magnetic ground states with large moments are observed in Ce compounds such as $CeIn_3$ [10] and $CeAl_2$ [11]. As $T_{\rm K}$ is increased to the order of $T_{\rm RKKY}$, the Néel temperature $T_{\rm N}$ passes through a broad maximum and then disappears at a quantum critical point (QCP). At QCP, non-Fermi-liquid (NFL) behaviors, $C/T \propto -\log T$, $\chi \propto (1-\alpha T^{1/2})$, and $\rho \propto T$, have been reported in Ce-based compounds such as $CeCu_{5.9}Au_{0.1}$ [12] and $Ce_{1-x}La_xRh_2Si_2$ [13]. The ground states of heavy fermion compounds $CeRu_2Si_2$ [14] and $CeCu_6$ [15] can be described by the Landau Fermi-liquid (FL) theory. On further increasing $T_{\rm K}$ ($T_{\rm K} \gg T_{\rm RKKY}$), a paramagnetic ground state becomes stable by the strong Kondo effect. The $4f$ state in this region tends toward an intermediate valence state.

Recently, the Doniach phase diagram has been revised by means of the continuous time quantum Monte Carlo method combined with the dynamical mean-field theory [17]. The nature of the itinerant-localized transition for heavy fermion compounds has been studied based on the Kondo-Heisenberg lattice:

$$H = \sum_{\boldsymbol{k},\sigma} \xi_{\boldsymbol{k}\sigma} c^{\dagger}_{\boldsymbol{k}\sigma} c_{\boldsymbol{k}\sigma} + J_{\rm K} \sum_i \boldsymbol{S}_i \cdot \boldsymbol{s}_{ci} + \frac{J_{\rm H}}{z} \sum_{(ij)} \boldsymbol{S}_i \cdot \boldsymbol{S}_j, \tag{1.11}$$

where $\xi_{\boldsymbol{k}} = \epsilon_{\boldsymbol{k}} - \mu$ with μ being the chemical potential, $J_{\rm K}$ is the Kondo interaction between the localized electron spin $\boldsymbol{S}_i$ and conduction electron spin $\boldsymbol{s}_{ci}$, and $J_{\rm H}$ is the Heisenberg interaction between the localized spins $\boldsymbol{S}_i$ and $\boldsymbol{S}_j$. Figure 1.9 shows the $J_{\rm K}$ variations of Néel temperature $T_{\rm N}$ and characteristic temperature $T_{\rm F}^*$, which corresponds to the effective Fermi temperature. On cooling below $T_{\rm F}^*$, $\rho(T)$ decreases due to the development of coherence in the Kondo lattice. The temperature at the peak of $\rho(T)$ is denoted as $T_{\rm F}^*$ as shown in Fig. 1.9 (b). With increasing $J_{\rm K}$, $T_{\rm F}^*$ decreases and disappears at $J_{\rm K} = J_{c2} = 0.16$, which is located inside the AFM phase. Moreover, $T_{\rm N}$ increases toward $J_{\rm K} = 0.23$, but suddenly decreases and disappears at $J_{\rm K} = J_{c1} = 0.27$, where the

magnetic QCP exists.

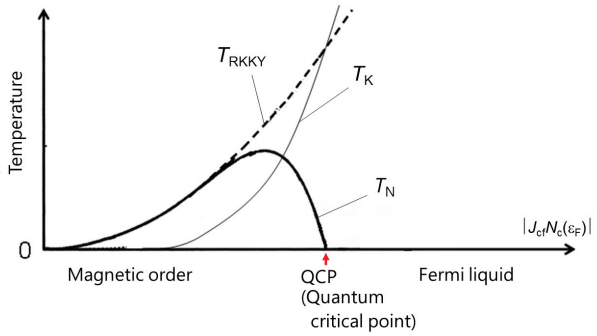

Figure 1.8: The phase diagram based on the Doniach model [9]. T_N (solid line) is the antiferromagnetic tempeature, T_K and T_{RKKY} (dotted lines) are the characteristic temperatures of Kondo effect and RKKY interaction described by Eqs. (1.7) and (1.10), respectively. Non-Fermi liquid behaviors appear at the quantum critical point (QCP). On the right side, the Fermi liquid state recovers [2, 3, 4].

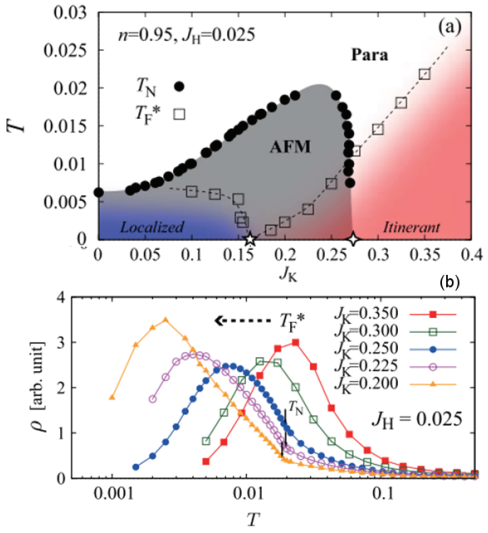

Figure 1.9: (a) Temperature versus Kondo interaction J_K phase diagram based on the Kondo- Heisenberg lattice model [17]. The number of conduction electron and Heisenberg exchanges are fixed as $n = 0.95$ per site and $J_H = 0.025$, respectively. (b) Temperature variation of the electrical resistivity $\rho(T)$ at various J_K. The dotted arrow shows the change of T_F^* with decreasing J_K.

1.2.3 Heavy-fermion compounds

Most heavy-fermion compounds are cerium-, ytterbium-, and uranium-based compounds, which are described as Kondo-lattice systems. The strong correlation of $4f$ electrons with conduction electrons enhances the effective mass m^* of quasiparticles by 100–1000 times at low temperatures [2, 3, 4, 16]. The heavy mass manifests in the specific heat C because the γ value is proportional to m^*, as shown in Eq. (1.13).

$$C/T = \gamma + \beta T^2, \tag{1.12}$$

$$\gamma = \frac{2\pi^2}{3} N(E_{\rm F}) k_{\rm B}^2 = \frac{k_{\rm B}^2 k_{\rm F} m^*}{3\hbar^2}, \tag{1.13}$$

where $\hbar$ is Dirac's constant.

In the Kondo-lattice systems, $\rho(T)$ exhibits different behaviors from that of the Kondo impurity shown in Fig. 1.7. On cooling, the Kondo scattering at each site becomes coherent in the lattice. Far below $T_{\rm K}$, $\rho(T)$ decreases in proportion to T^2 as expressed in Eq. (1.14).

$$\rho = \rho_0 + {\rm A}T^2, \tag{1.14}$$

where ρ_0 is the residual resistivity. The coefficient A reflects the mass enhancement of the electrons because this term originates from electron–electron scattering. The coefficient A reflects the mass enhancement of the electrons because this term originates from electron–electron scattering. Figure 1.10 represents $\rho(T)$ for the typical heavy-fermion compound $CeAl_3$ [18]. A broad maximum in the $\rho(T)$ at around 40 K is a sign of the onset of coherence over the Kondo lattice, and $\rho(T)$ obeys the AT^2 power law at $T < 0.3$ K. The ratio between γ^2 and A has a universal value, ${\rm A}/\gamma^2 \simeq 1.0 \times 10^{-5} \mu\Omega{\rm cmK}^{-2}/({\rm mJK}^{-2}{\rm mol}^{-1})^2$, in various heavy-fermion compounds as shown in Fig. 1.11 [19]. The magnetic susceptibility at $T = 0$ also reflects the mass enhancement as shown in Fig. 1.12 (b) [20]. The $\chi(T)$ tends to be satulated to a largely enhanced value of $2\mu_{\rm B} N(E_{\rm F})$ at $T < T_\chi$ (temperature at the maximum of $\chi(T)$). The values of $T_{\rm N}$, γ in C/T, A in $\rho(T)$, and $\chi(T \to 0)$ for typical heavy-fermion compounds as well as noble metals Ag and Pd are listed in Table 1.1. The mass enhancement in the Ce compounds is manifested therein as compared with Ag and

Pd.

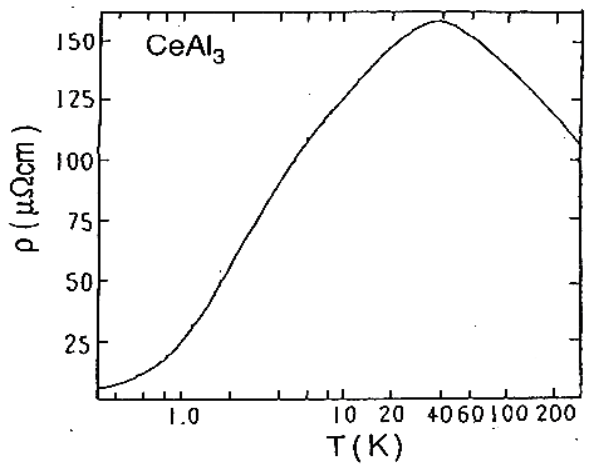

Figure 1.10: The resistivity of a typical heavy fermion compound $CeAl_3$ [18].

Table 1.1: The AFM ordering temperature T_N, γ in C/T, coefficient A in ρ, and $\chi(T \to 0)$ for Ce-based heavy-fermion compounds [2, 3, 4].

Material	T_N or T_{SC} [K]	γ [mJ/molK^2]	$\chi(T \to 0)$ [10^{-2} emu/mol]	A [$\mu\Omega$ cm /K^2]
$CeCu_6$	—	1500	4.5	70
$CeAl_3$	—	1600	5.5	35
$CeCu_2Si_2$ (SC)	0.65	1100	12.0	16
$CeRh_2Si_2$ (AF)	36	23	0.3	1.4×10^{-3}
Ag	—	0.6	0.03	10^{-7}
Pd	—	9.4	0.8	10^{-5}

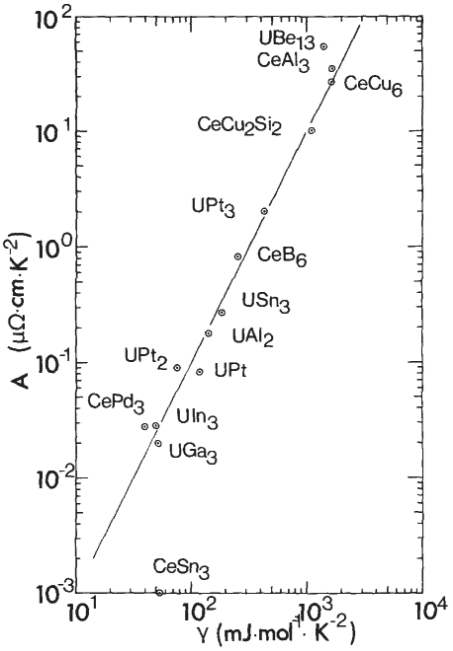

Figure 1.11: Kadowaki-Woods plot of A in $\rho(T)$ and γ in $C(T)$. The linear line gives the universal ratio $A/\gamma^2 = 1.0 \times 10^{-5}\mu\Omega\text{cm}/(\text{mol K/mJ})^2$ [19].

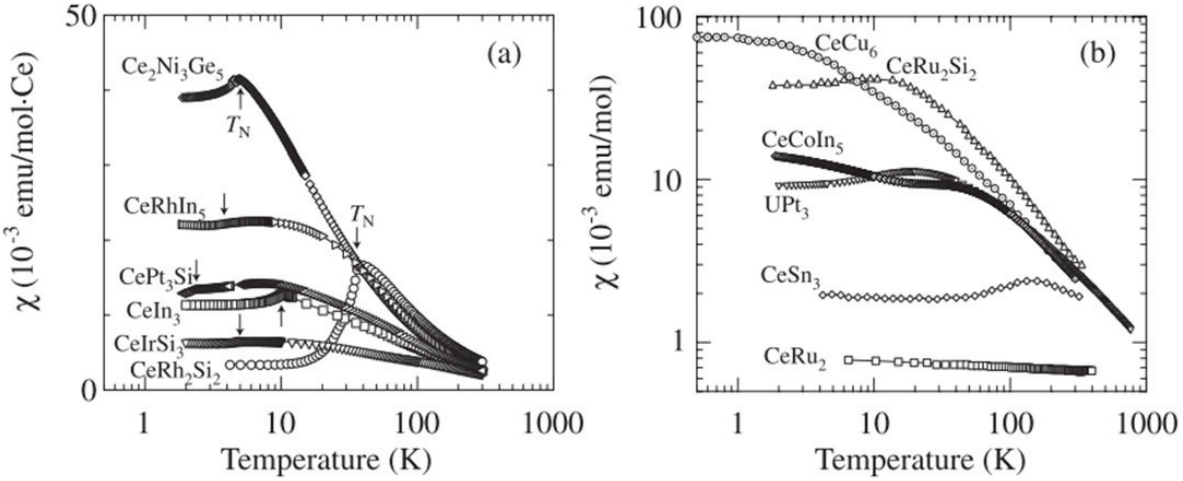

Figure 1.12: Temperature dependences of the magnetic susceptibility $\chi(T)$ in Ce-based heavy-fermion compounds (a) with and (b) without magnetic order [20]. The arrows indicate $T_{\rm N}$.

1.2.4 Kondo semiconductors

A small number of heavy-fermion compounds possess a narrow gap in the vicinity of $E_{\rm F}$ in the hybridized bands [27]. They are called as Kondo semiconductors (KSs) exemplified by CeNiSn [21, 22, 41, 39], CeRhSb [23, 24, 41, 40], and CeRhAs [25, 26]. Below $T_{\rm K}$, these $\rho(T)$s exhibit semiconducting or semimetallic behaviors in concomitant with decreasing thermopowers $S(T)$s as shown in Fig. 1.13 (a, b) [28]. These narrow gap formations is thought to play the key role in the hybridization between the $4f$ electron states and conduction bands.

We recall here the DOS for a typical semiconductor Si with a gap of $\sim$ 1 eV in the band structure. The band gap shown in Fig. 1.14 (a) hardly depends on the temperature. By contrast, the hybridization gap (1 – 100 meV) for KSs develops in the hybridized band on cooling when the number of conduction electrons in the unit cell is equal to the number of $4f$ electrons. Figure 1.14 (b, c) shows the gap formation in Kondo semiconductors. The DOS displays a Kondo resonance peak at $T \sim T_{\rm K}$, wherein a V-shaped gap develops on cooling below $T_{\rm K}$. As shown in Fig. 1.15, $\chi(T)$ of CeNiSn and CeRhSb exhibits a maximum at around 20 K. The decrease in $\chi(T)$ below 20 K is not due to an AFM order but due to the decrease in DOS at $E_{\rm F}$ [28].

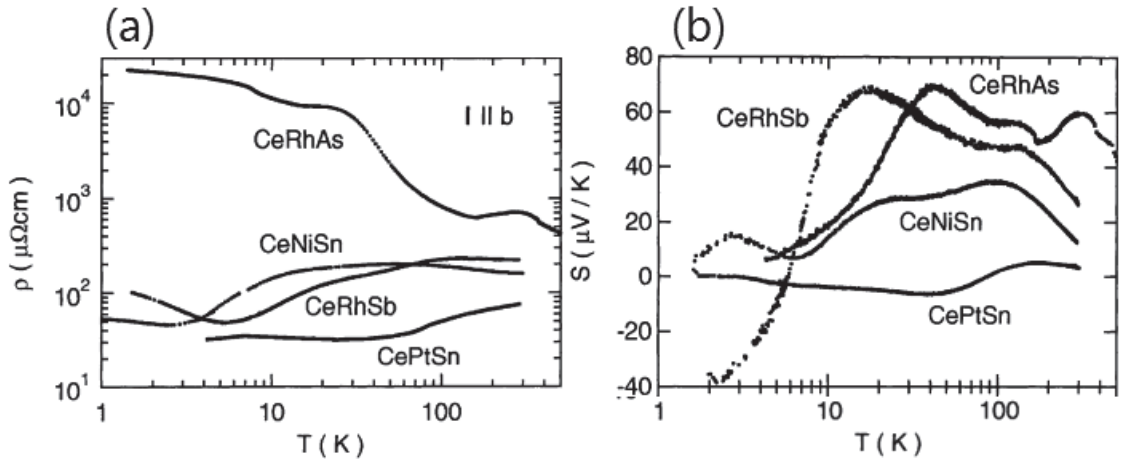

Figure 1.13: Temperature dependences of (a) electrical resistivity $\rho(T)$ and (b) thermopower along the orthorhombic b axis for single crystals of CeNiSn, CeRhSb, and CeRhAs [28, 29].

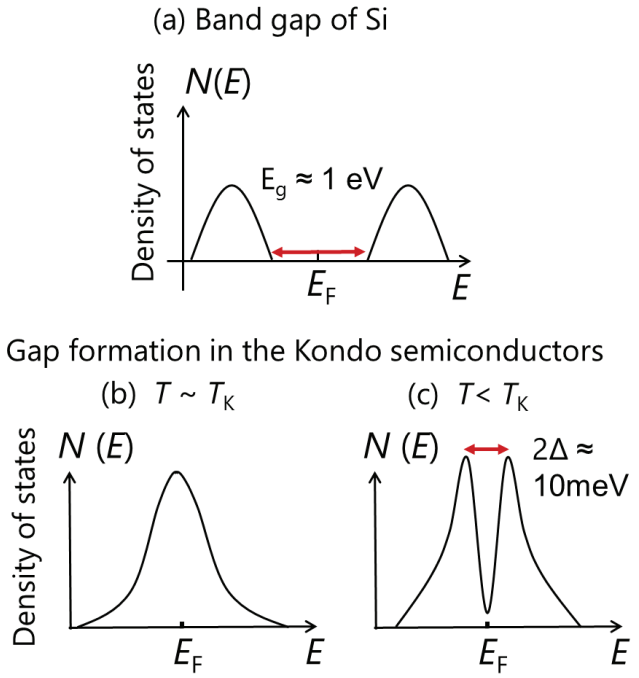

Figure 1.14: Density of states $N(E_{\mathrm{F}})$ for (a) the band semiconductor Si and (b, c) Kondo semiconductors at $T \sim T_{\mathrm{K}}$ and $T < T_{\mathrm{K}}$, respectively.

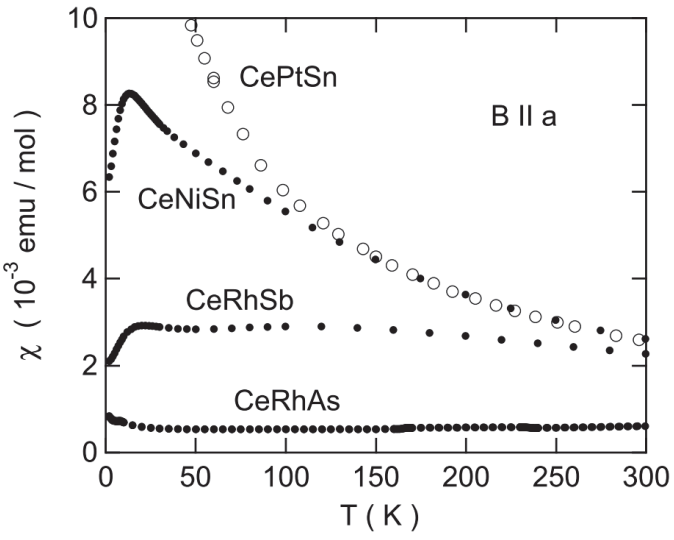

Figure 1.15: Magnetic susceptibility $\chi(T)$ for single crystals of Kondo semiconductors CeNiSn, CeRhSb, and CeRhAs and a localized $4f$ system CePtSn along the orthorhombic a axis [28].

The crystal structures, transport gaps and $T_{\rm K}$s of KSs are listed in Table 1.2. The cubic systems $Ce_3Bi_4Pt_3$ [30, 31] and YbB_{12} [32, 33] have well-defined energy gaps of the order of $T_{\rm K}$ which magnitudes are estimated by the transport measurements. On the other hand, an incomplete gap opens in CeNiSn and CeRhSb with the orthorhombic ϵ-TiNiSi-type structure [28]. The latter reflects the anisotropic gap which closes in a particular direction due to the anisotropy of the c-f hybridization [38]. The hybridization gaps in the KSs have been observed by several methods. Nuclear magnetic/quadruple resonance (NMR/NQR) investigations on ^{119}Sn in CeNiSn and ^{139}Sb in CeRhSb showed unusual T-dependence of the nuclear spin-lattice relaxation rates $1/T_1$. As shown in Fig. 1.16, $1/T_1$ decreases below 30 K and then follows a T^3 power dependence from 7 to 2 K [39, 40]. Below 0.4 and 0.6 K for CeNiSn and CeRhSb, respectively, $1/T_1T$ becomes constant. These temperature dependences first evidenced the opening of V-shaped pseudogap with the residual $N(E_{\rm F})$. As shown in Fig. 1.17, the magnetic specific heat divided by temperature $C_{\rm m}/T$ for CeNiSn and CeRhSb shows the broad maximum and then decreases on cooling, confirming the formation of the V-shaped gap [41].

Table 1.2: Crystal structure, transport gap, and Kondo temperature T_K of Kondo semiconductors.

Compound	Structure type	Transport gap (K)	$T_{\rm K}$ (K)	Ref.
SmB_6	Cubic CaB_6	53 – 80	160	[34, 35]
YbB_{12}	Cubic UB_{12}	124 – 136	240	[32, 33]
$Ce_3Bi_4Pt_3$	Cubic $Y_3Sb_4Au_3$	84 – 100	240	[30, 31]
$Ce_3Sb_4Pt_3$	Cubic $Y_3Sb_4Au_3$	950	1200	[36]
CeNiSn	Orthorhombic ϵ–TiNiSi	14 – 21	39	[21, 22, 41, 39]
CeRhSb	Orthorhombic ϵ–TiNiSi	28	360	[23, 24, 41, 40]
CeRhAs	Orthorhombic ϵ–TiNiSi	290	1300	[25, 26]
$CeOs_4Sb_{12}$	Cubic $LaFe_4P_{12}$	10	90	[37]

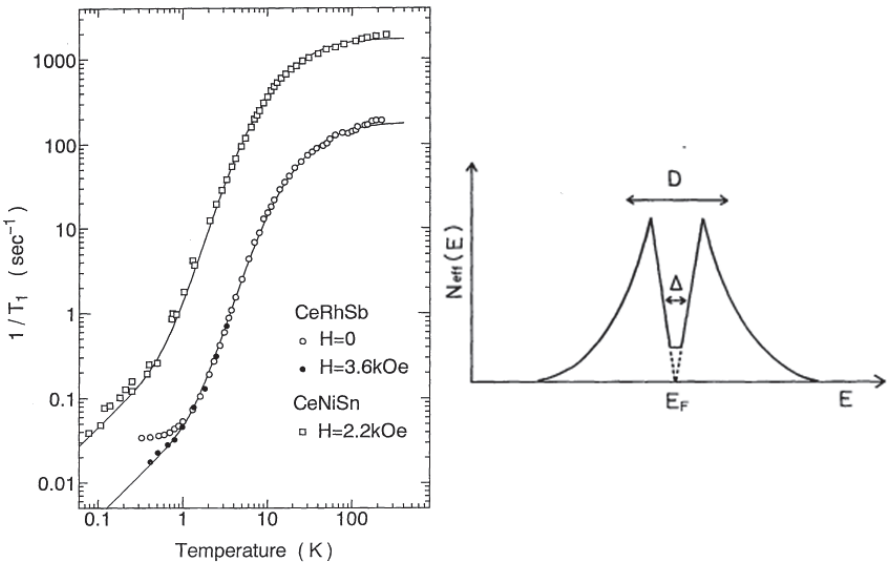

Figure 1.16: Temperature dependences of spin-lattice relaxation rate $1/T_1$ of ^{119}Sn for CeNiSn and ^{123}Sb for CeRhSb. Solid lines in both compounds are $1/T_1$ calculated by using the V-shaped DOS with the residual $N(E_{\rm F})$ as shown on the right side [39, 40].

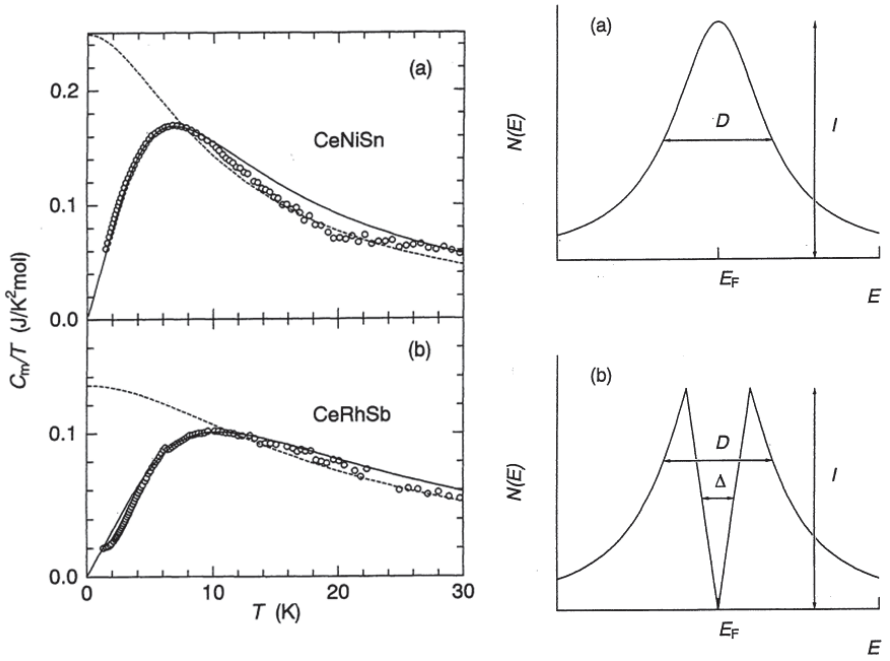

Figure 1.17: Temperature dependences of magnetic specific heat for CeNiSn and CeRhSb. Solid lines are calculated with the V-shaped gap model as shown on the right side, and the dotted line are calculated with the Lorentzian shape DOS [41].

Photoemission spectroscopy and optical conductivity measurements are direct probes to observe the temperature development gaps. Figures 1.18 and 1.19 represent, respectively, the temperature variations of the photoemission spectra and optical conductivity spectra for CeRhSb [42, 44], CeRhAs [42, 44], and YbB_{12} [43, 45]. On cooling, all spectra exhibit shoulder structures, which represent the development of the gaps.

Another method to observe the development of hybridization gaps is the break-junction tunneling spectroscopy. The spectra of differential conductance dI/dV versus bias voltage V in CeNiSn, CeRhSb, and CeRhAs have well-defined gap structures of V_1 and V_2 with a finite value at $V = 0$ as displayed in Figs. 1.20 and 1.21 (a). There are a pair of peak structures at V_2, which become obvious on cooling. The finite zero-bias conductance (ZBC), dI/dV at $V = 0$, is the indication of the residual $N(E_F)$ because the ZBC is proportional to the square of $N(E_F)$. In the cubic Kondo semiconductor YbB_{12}, on the other hand, the dI/dV spectrum has a U-shaped structure without in-gap states as shown in Fig. 1.21 (b) [49].

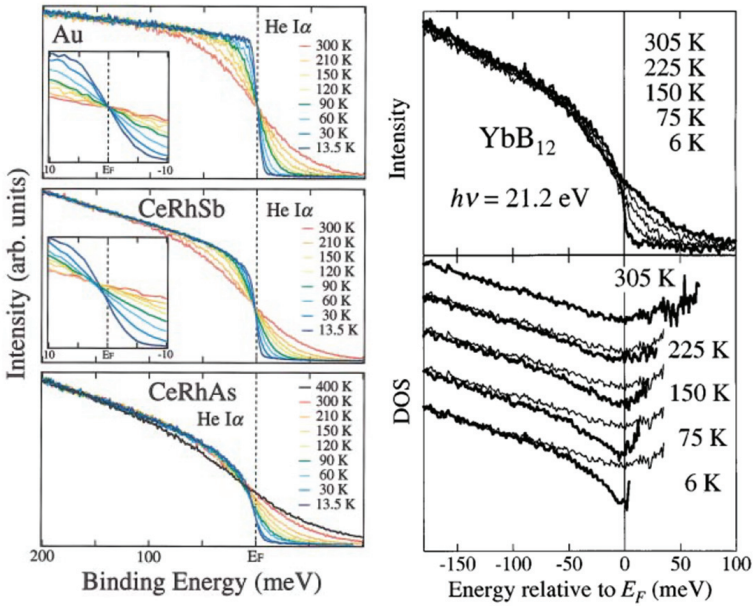

Figure 1.18: Temperature dependent photoemission spectra for CeRhSb (Δ_{PES} = 30–35 meV), CeRhAs (Δ_{PES} = 90–100 meV), and YbB_{12} (Δ_{PES} = ∼100 meV) measured with He Iα (21.2 eV) radiation [42, 43].

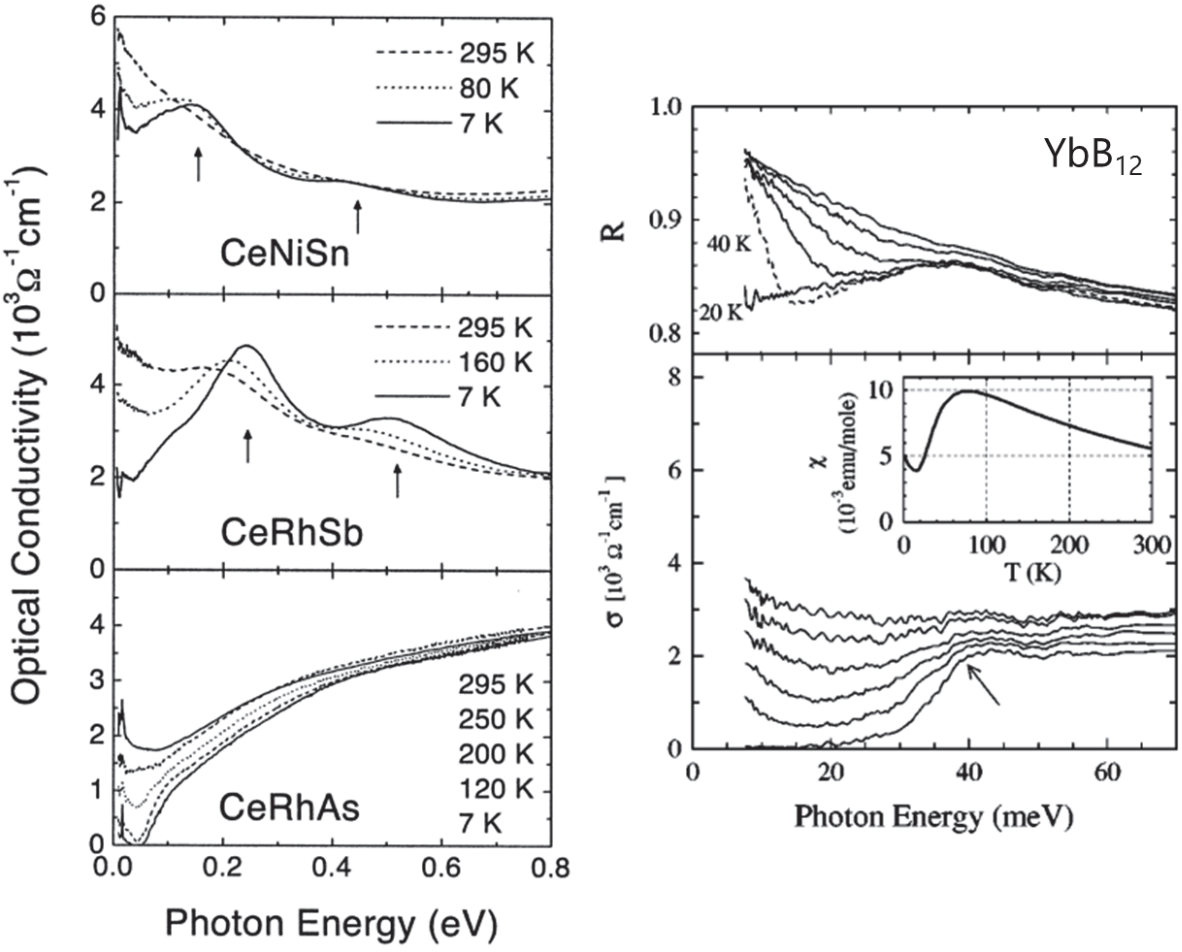

Figure 1.19: Temperature dependence of optical conductivity spectra for CeNiSn ($\Delta_{\rm Opt} = \sim 10$ meV), CeRhSb ($\Delta_{\rm Opt} = \sim 15$ meV), CeRhAs ($\Delta_{\rm Opt} = \sim 100$ meV), and YbB_{12} ($\Delta_{\rm Opt} = \sim 40$ meV) [44, 45], where $\Delta_{\rm opt}$ is the optical gap. The arrows indicate the mid-IR peaks.

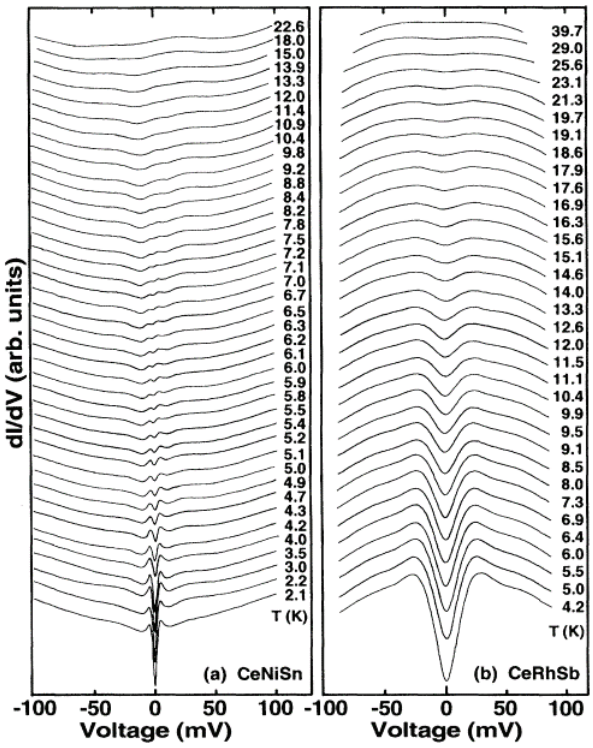

Figure 1.20: Temperature dependence of tunneling spectra for the orthorhombic Kondo semiconductors CeNiSn ($eV_2/2 = \simeq$10 meV) and CeRhSb ($eV_2/2 = \simeq$27 meV) [46, 47].

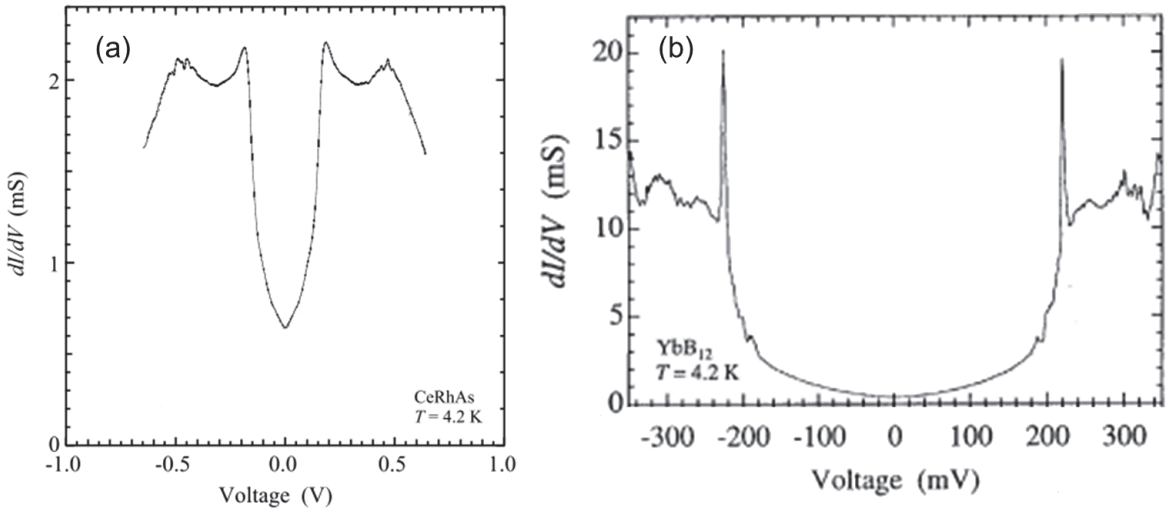

Figure 1.21: Tunneling spectrum at 4.2 K for (a) the orthorhombic Kondo semiconductor CeRhAs ($eV_1^{\mathrm{P-P}}/2 \simeq$500 meV and $eV_2^{\mathrm{P-P}}/2 \simeq$180 meV) and (b) the cubic Kondo semiconductor YbB_{12} ($eV^{\mathrm{P-P}}/2 \simeq$220 meV) [48, 49].

Theoretical models of Kondo semiconductors

Theoretical studies of Ce-based KSs have been performed on the basis of the periodic Anderson model (PAM) [38, 50, 51, 52]. In Ce compounds with non cubic symmetry, the sixtet of the total angular moment $J = 5/2$ is split into three Krammers doublets by the crystalline electric field (CEF). The ground state doublet determines the anisotropy of hybridization of KSs. In Ce-based orthorhombic KSs, the $\boldsymbol{k}$-dependece of the hybridization matrix element between f- and conduction electrons gives rise to an anisotropic hybridization [38, 51, 52]. The anisotropic hybridization induces the nodes in the energy gap along a certain direction in the $\boldsymbol{k}$ space, leading to a V-shaped DOS. Ikeda and Miyake treated the following Hamiltonian [38],

$$\begin{aligned} H &= \sum_{\boldsymbol{k},\sigma} \epsilon_{\boldsymbol{k}\sigma} c^{\dagger}_{\boldsymbol{k}\sigma} c_{\boldsymbol{k}\sigma} \\ &\quad + \sum_{\boldsymbol{k},\mu} E_{\mu} f^{\dagger}_{\boldsymbol{k}\mu} f_{\boldsymbol{k}\mu} + \sum_{\boldsymbol{k}\mu\sigma} \Big(V^{*}_{\boldsymbol{k}\mu\sigma} f^{\dagger}_{\boldsymbol{k}\mu} c_{\boldsymbol{k}\sigma} + \text{h.c.} \Big) \\ &\quad + \frac{U}{2} \sum_{\boldsymbol{k},\boldsymbol{k'},\boldsymbol{q},\mu\neq\mu'} f^{\dagger}_{\boldsymbol{k}-\mathbf{q}\mu} f^{\dagger}_{\boldsymbol{k'}+\mathbf{q}\mu'} f_{\boldsymbol{k'}\mu'} f_{\boldsymbol{k}\mu}. \end{aligned} \tag{1.15}$$

where $c^{\dagger}_{\boldsymbol{k}\sigma}$ and $\epsilon_{\boldsymbol{k}\sigma}$ are the creation operator and energy of conduction electron in the plane wave state labeled by wave vector $\boldsymbol{k}$ and spin σ, respectively, where $\sigma = +1$, -1 denote up and down spins. E_{μ} and $f^{\dagger}_{\boldsymbol{k}\mu}$ are the energy of f-level and the creation operator of f electron, respectively, where μ represents index of f state: $\mu = \pm 1,\ \pm 2,\ \pm 3$. U is the Coulomb repulsion between f electrons. The plane wave states of conduction electrons and $4f$ electrons around the site i ($\boldsymbol{r}_i$) could be written as follow,

$$\begin{aligned} |\boldsymbol{k}\sigma\rangle &= \frac{1}{\sqrt{V}} \mathrm{e}^{i\boldsymbol{k}\cdot\boldsymbol{r}} \chi_{\sigma} \\ &= \frac{4\pi}{\sqrt{V}} \mathrm{e}^{i\boldsymbol{k}\cdot\boldsymbol{r}} \sum_{l=0}^{\infty} i^{l} j_{l}(k|\boldsymbol{r} - \boldsymbol{r}_i|) \\ &\quad \times \sum_{m=-l}^{l} Y^{m}_{l}(\Omega_{\boldsymbol{k}}) Y^{m}_{l}(\Omega_{\boldsymbol{r}-\boldsymbol{r}_i}) \chi_{\sigma}, \end{aligned} \tag{1.16}$$

$$|M\rangle = \sum_{\mu} B^{M}_{\mu} \sum_{m\sigma} A^{\mu}_{lm\sigma} Y^{m}_{l}(\Omega_{\boldsymbol{r}-\boldsymbol{r}_i}) \chi_{\sigma}, \tag{1.17}$$

where χ_{σ} is the spin function, $j_l(kr)$ is the spherical Bessel function, Y^{m}_{l} is the spherical harmonics with the argument of solid angle $\Omega_{\boldsymbol{r}}$ of the position vector $\boldsymbol{r}$ or $\Omega_{\boldsymbol{k}}$ of the

wave vector $\boldsymbol{k}$, V is the volume of the crystal, μ is the z-component of the total angular momentum, J, and $A^{\mu}_{lm\sigma}$ are the Clebsch-Gordan coefficients, and B^{M}_{μ} are coefficients specifying the crystal-field level.

The mixing potential $V_{\boldsymbol{k},\mu,\sigma}$ between f electron and conduction electrons in Eq. (1.15) is given by

$$V_{\boldsymbol{k},\mu,\sigma} = \sqrt{4\pi} V_{kl} \sum_{M} B^{M}_{\mu} \sum_{m} A^{M}_{lm\sigma} Y^{m}_{l}(\theta_k, \varphi_k) \tag{1.18}$$

Here, V_{kl} has the angular variations of the mixing matrix. When $V_{\boldsymbol{k},\mu,\sigma}$ is regarded as independent of σ, the $\boldsymbol{k}$-dependence of $V_{\boldsymbol{k}}$ is calculated. Assuming the crystal-field ground state of $|J_z\rangle = |\pm 3/2\rangle$ under the trigonal local structure, the results can be expressed as,

$$V^{2}_{\pm m}(\boldsymbol{k}) = V^{2}(1 - k_z^2)(1 + 15k_z^2) \tag{1.19}$$

where m is the magnetic quantum number. As derived from Eqs. (1.15)–(1.19), the gap function $\Delta_{\boldsymbol{k}}$ is given by

$$\Delta(k_z) = T_{\mathrm{K}}(1 - k_z^2)(15k_z^2 + 1), \tag{1.20}$$

and the quasiparticle DOS is calculated as follows:

$$\begin{aligned} \tilde{N}(\epsilon) &= \sum [\delta(\omega - E^{+}_{\mathrm{k}}) + \delta(\omega - E^{-}_{\mathrm{k}})] \\ &= N_{\mathrm{F}} \int_{0}^{1} d\tilde{k_z} \int_{-D}^{D} dE (1 + \frac{\tilde{V}^{2}_{f}(\tilde{k_z})}{E^2}) \times \delta(\omega - E)\ \theta(|E| - \Delta(\tilde{k_z})). \end{aligned} \tag{1.21}$$

Figure 1.22 shows the quasiparticle DOS obtained from Eq. (1.21). The DOS has the well-defined two gap structure with a residual DOS at E_{F}. Moreover, the ratio of Δ_1/Δ_2 equals to $\sim$4.2.

For the hexagonal symmetry, Fig. 1.23 shows the DOS as a function of ω and anisotropy of hybridization gap along the path from k_z–axis to k_x–k_y plane in (a, b) $|J_z\rangle = |\pm 5/2\rangle$, (c, d) $|J_z\rangle = |\pm 3/2\rangle$, and (e, f) $|J_z\rangle = |\pm 1/2\rangle$ [50]. In the case of the $|J_z\rangle = |\pm 5/2\rangle$, there is no gap, but a sharp peak at E_{F} (Fig. 1.23 (a)), which is caused by two point nodes at $k_z = \pm 1$ (Fig. 1.23 (b)). For $|J_z\rangle = |\pm 3/2\rangle$, two distinct gaps with a residual DOS at E_{F} manifests as shown in Fig. 1.23 (c). For $|J_z\rangle = |\pm 1/2\rangle$, there is no point node so that a perfect gap opens over the Fermi surface (Fig. 1.23 (e, d)).

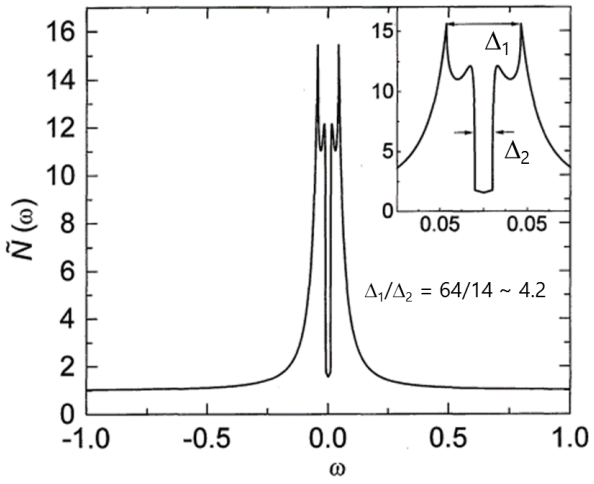

Figure 1.22: Quasiparticle density of states as a function of energy ω. The Fermi level is located at $\omega = 0$ [38, 51, 52].

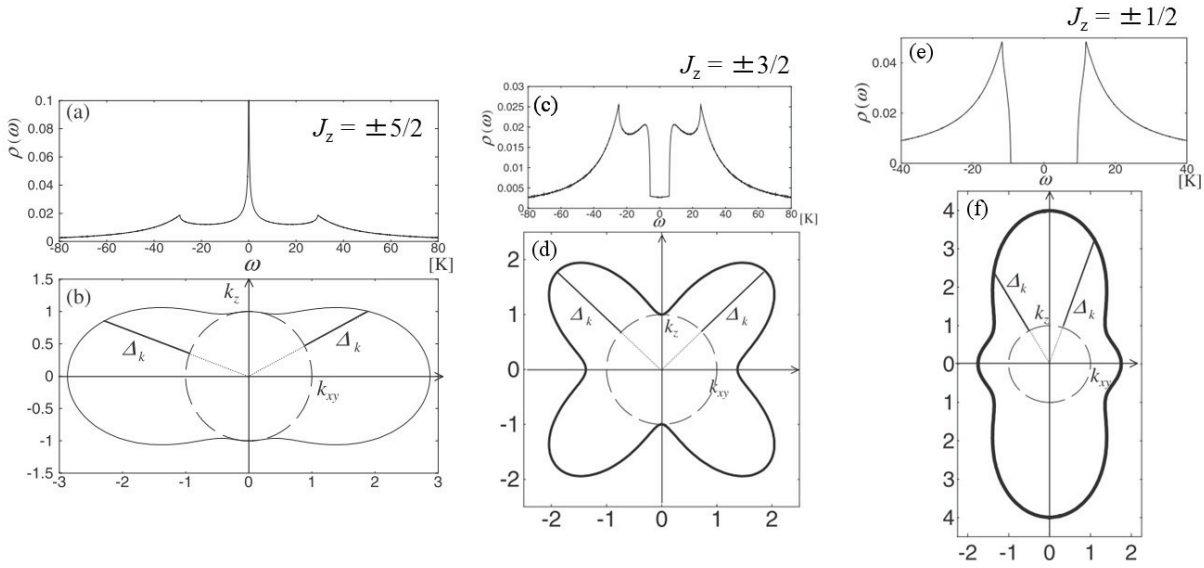

Figure 1.23: DOS as a function of energy ω and anisotropy of hybridization gap along the path from k_z–axis to k_x–k_y plane in (a, b) $|J_z\rangle = |\pm 5/2\rangle$, (c, d) $|J_z\rangle = |\pm 3/2\rangle$, and (e, f) $|J_z\rangle = |\pm 1/2\rangle$ in the hexagonal symmetry [50].

1.2.5 Doping studies of Kondo semiconductors

The Kondo semiconductor CeNiSn belongs to the valence fluctuating regime. This compound does not order magnetically at low temperatures because the $4f$ moments are quenched by the strong c-f hybridization. However, doping of $3d$ electrons in CeNiSn by Cu substitution for Ni at 10∼20% induces a long-range antiferromagnetic (AFM) order as shown in Fig. 1.24 (a, c) [53, 54, 55]. The emergence of AFM order was attributed to the weakened c-f exchange interaction which is a consequence of the increase of the Fermi energy with respect to the $4f$ level. On the other hand, doping of $3d$ holes in CeNiSn by Co substitution for Ni (Fig. 1.24 (b)) suppresses the maximum of $\chi(T)$, indicating that the doping enhances the c-f hybridization [54].

Figure 1.25 displays the semilogarithmic plots of $S(T)$ along c axis. For non-doped CeNiSn, $S(T)$ increases from 300 to 100 K due to Kondo scattering. On cooling below 20 K, $S(T)$ successively decreases and then shows the minimum. The decrease reflects the opening of the hybridization gap because the $S(T)$ is proportional to the energy differential of quasiparticle DOS at the chemical potential as will be described in Experimental. When 5% Co is substituted for Ni, the minimum changes to a large peak of 63 μV/K at 7 K. The $3d$ hole doping shifts the Fermi energy $E_{\rm F}$ downward so that the energy derivative of the DOS at $E_{\rm F}$ in $CeNi_{0.95}Co_{0.05}Sn$ become larger than that in CeNiSn. For $CeNi_{0.66}Co_{0.34}Sn$, the resistivity and magnetic susceptibility show the valence fluctuating behavior [59]. The $S(T)$ is expected to show similar behavior of the valence fluctuating compound CeNi as depicted in Fig. 1.25 (b) [57, 58]. By contrast, $S(T)$ for the 5% Cu substituted sample becomes negative at 6 K. The small and negative value at low temperatures is similar to the behavior of the localized $4f$ electron compound CePtSn as shown in Fig. 1.25 [29, 60]. The negative $S(T)$ at low temperatures indicates the appearance of antiferromagnetic spin correlation [29, 57]. These results reveal that the localization tendency of $4f$ electrons manifests as the change in $S(T)$ to a negative value.

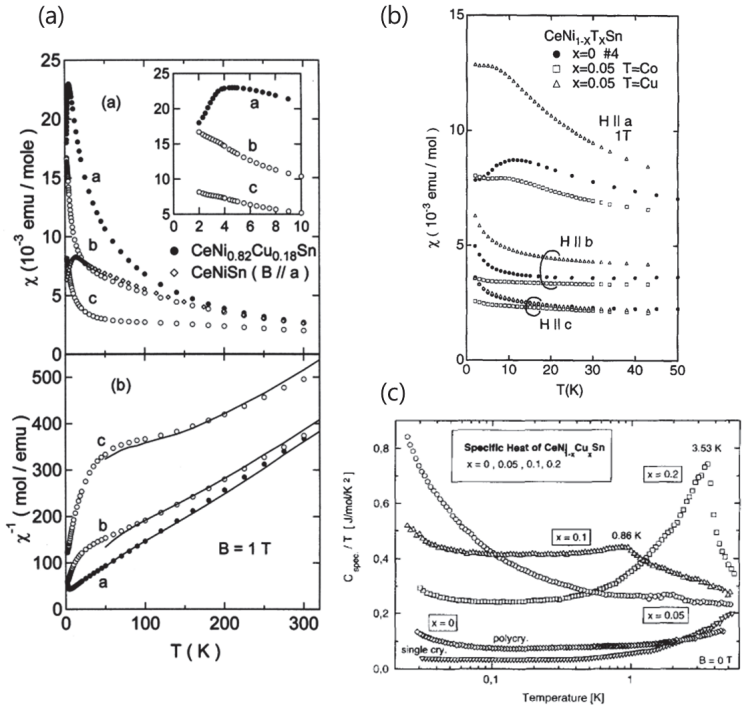

Figure 1.24: Temperature dependences of (a, b) magnetic susceptibility $\chi(T)$ and (c) specific heat divided by T for the $3d$-hole and $3d$-electron doped Kondo semiconductor $CeNi_{1-x}Co_xSn$ ($0 \leq x \leq 0.05$) and $CeNi_{1-x}Cu_xSn$ ($0 \leq x \leq 0.2$) [53, 54, 55].

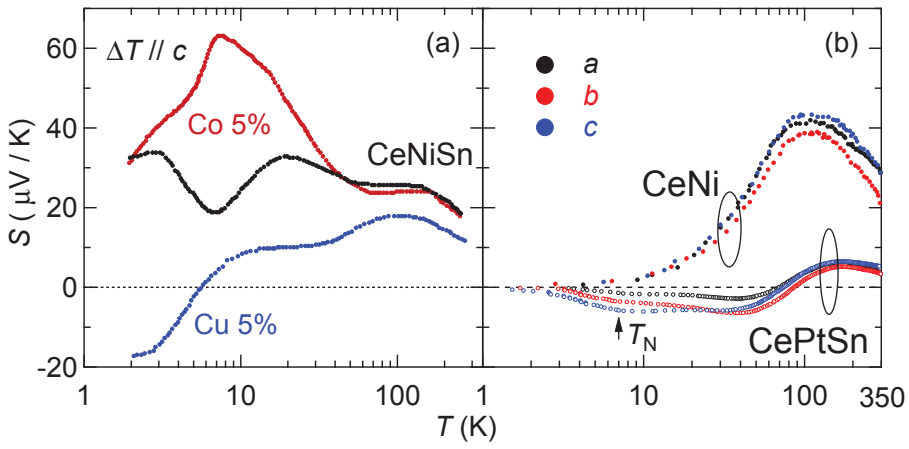

Figure 1.25: Temperature variations of thermopower $S(T)$ for (a) CeNiSn and 5% Co/Ni substituted samples along the c-axis [56] and (b) valence fluctuating compound CeNi [57, 58], localized $4f$ electron compound CePtSn along the principle axes [29, 60].

The $4f$-doped Kondo semiconductor CeRhAs was investigated by the break-junction tunneling spectroscopy on $Ce_{1-x}La_xRhAs$ [61]. As shown in Fig. 1.26 for $x = 0.01$, the two hybridization gaps in the dI/dV spectra broaden in concomitant with the appearance of a pair of humps near $V = 0$. The emergence of such in-gap states within the hybridization gap inhibits $\rho(T)$ from showing a semiconducting behavior as seen in the inset of Fig. 1.26.

Theoretical models

Figures 1.27–1.29 display the results of the DOS calculated for doped KSs on the basis of PAM. Assuming diluted Kondo holes in the $4f$ sublattice with the density of $4f$ and conduction electrons of $n^f + n^c = 2 - x$, the DOS exhibits an peak at E_F as shown for $x = 0.1$ in Fig. 1.27 [62]. With increasing the Kondo hole concentration x, the peak develops, keeping the hybridization gap width unchanged. At $x = 0.8$, there is a sharp peak at E_F without gap edge. Figure 1.28 shows the gap structure in DOS calculated for a slightly dispersive $4f$ band [63]. The Hamiltonian is also represented by the Eq. (1.15) and the quasiparticle dispersion relations $E^{\pm}(k)$ of the hybridized bands are given by

$$E^{\pm} = \frac{E_f(k) + \epsilon(k)}{2} \pm \sqrt{\left(\frac{E_f(k) - \epsilon(k)}{2}\right)^2 + |V(k)|^2}. \tag{1.22}$$

The calculation was done for a k-independent hybridization $V = 0.5\ t$, tight-binding conduction band $6t$, and a weak dispersion of the $4f$ band $t' = 0.03t$, $0.04t$, and $0.05t$. The f-f hopping strength t' lowers E_F toward the top of the lower c-f hybridization band, making hole pockets in the vicinity of the E_F. Therefore as t' increases, the gap edge is broadened, the gap width is suppressed, and an upward peak develops inside the gap,. In addition, non-magnetic impurities induce the impurity bands at E_F as shown in Fig. 1.29 [64]. The theory introduces rewritting the perturbed Green function in term of self-energy of $4f$ electrons in order to produce the non-magnetic impurities scattering effect [64].

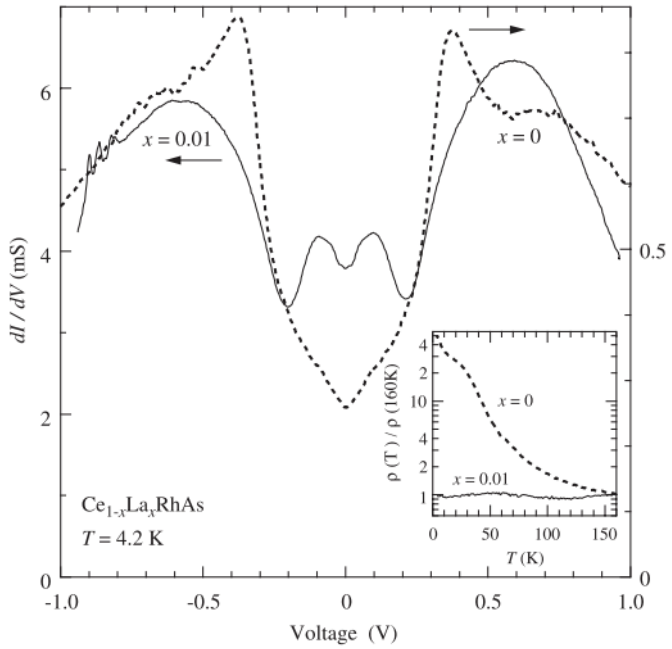

Figure 1.26: Break-junction tunneling spectra of $Ce_{1-x}La_xRhAs$ ($x = 0$ and 0.01) at 4.2 K. The inset shows the electrical resistivity data normalized by the value at 160 K [61].

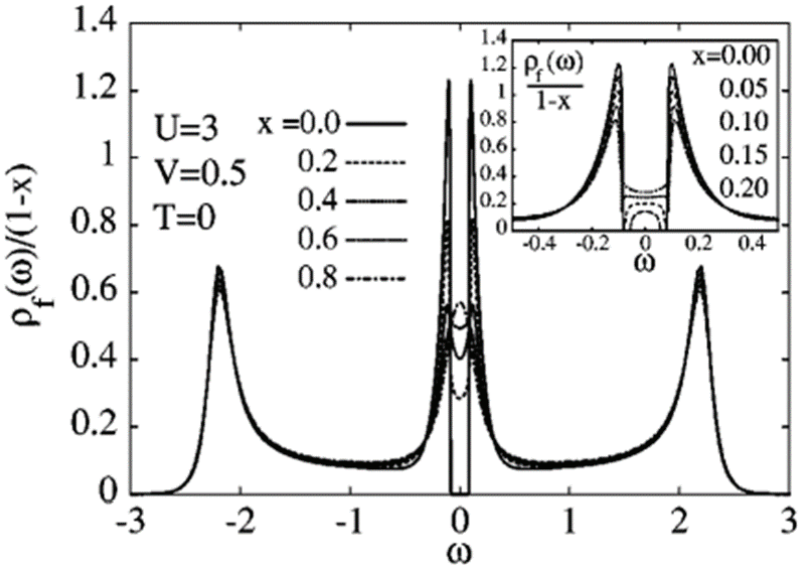

Figure 1.27: Quasiparticles density of states for a Kondo semiconductor doped with different amounts of holes as a function of energy ω, calculated by the dynamical mean-field theory. The Fermi level is located at $\omega = 0$ [62].

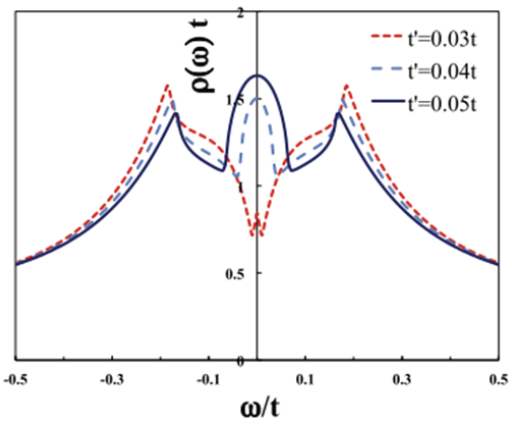

Figure 1.28: Quasiparticles density of states as function of energy ω for Kondo semimetal with various f-band hopping strength t'. The Fermi level is located at $\omega = 0$ [63].

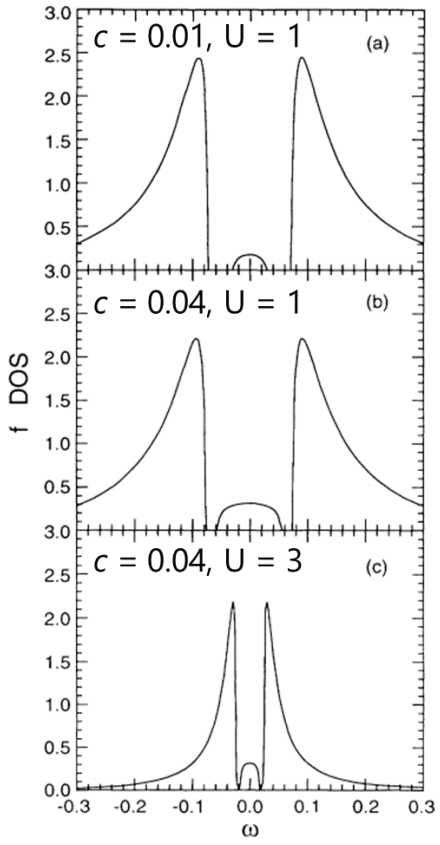

Figure 1.29: Quasiparticles density of state as function of energy ω for a Kondo semiconductor with the non-magnetic impurity concentration c and the Coulomb repulsion U. The Fermi level is located at $\omega = 0$ [64].

1.3 Kondo semiconductors CeT_2Al_{10} (T = Fe, Ru, and Os)

An orthorhombic compound $CeRu_2Al_{10}$ has been classified into the KSs because the electrical resistivity exhibits the thermal activation behavior, $\rho(T) \propto \exp(\Delta/2k_BT)$ [66]. This work triggered the systematic studies of CeT_2Al_{10} (T = Fe, Ru, and Os).

1.3.1 Crystal structure

The crystal structure of CeT_2Al_{10} (T = Fe, Ru, and Os) is shown in Fig. 1.30 [67, 68, 69, 66, 72, 75]. It crystallizes in the orthorhombic $YbFe_2Al_{10}$-type structure with the space group of *Cmcm*, No.63. The structural parameters of $CeOs_2Al_{10}$ are listed in Table 1.3 [69]. The Ce atom is surrounded by a polyhedron formed by 4 T and 16 Al atoms [69, 66, 72, 75]. There are two zigzag chains: one consists of the nearest Ce ions (blue solid line) and the other is Ce–T–Ce zigzag chain(green dotted line). Furthermore, the local inversion symmetry at the Ce site with respect to the b axis is absent, which allows the on-site mixing on $4f$- and $5d$- states of the Ce ion [70]. The lattice parameters, unit cell volume and Ce–Ce and Ce–T interatomic distances given by neutron diffraction investigations are listed in table 1.4 [69, 83]. The atomic distance between the nearest Ce–Ce atoms ($\sim$ 5.2 Å) is larger than those between the Ce and T or Al atoms. When going form Fe, Os to Ru, the values of unit cell volume V and interatomic distances Ce–Ce and Ce–T increase by 2%, 0.8%, 0.7%, respectively.

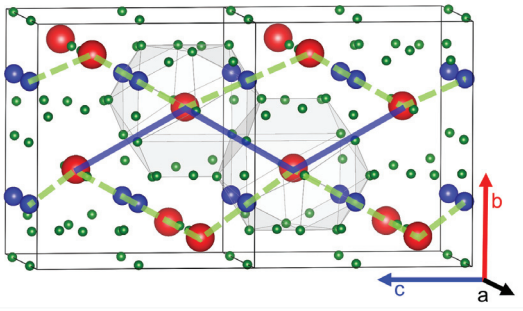

Figure 1.30: $YbFe_2Al_{10}$-type crystal structure of CeT_2Al_{10}. The blue solid line and green dotted line represent the nearest Ce–Ce and Ce–T–Ce zigzag chains [66, 68, 69, 72, 75].

Table 1.3: Structural parameters of $CeOs_2Al_{10}$ in the orthorhombic $YbFe_2Al_{10}$-type structure with *Cmcm* space group determined from the neutron diffraction experiment at 2 K [83].

atom	site	x	y	z
Ce	4c	0	0.1257(2)	0.25
Os	8d	0.25	0.25	0
Al 1	8g	0.2240(2)	0.36530(2)	0.25
Al 2	8g	0.3494	0.1324(2)	0.25
Al 3	8f	0	0.1579(2)	0.6020(2)
Al 4	8f	0	0.3779(3)	0.0485(2)
Al 5	8e	0.2240(2)	0	0

Table 1.4: Lattice parameters and interatomic distances of Ce–Ce and Ce–T for CeT_2Al_{10} (T = Fe, Ru and Os) determined by neutron diffraction experiments at 300 K [69, 83].

T	a (Å)	b (Å)	c (Å)	V (Å^3)	Ce–Ce (Å)	Ce–T (Å)	Ce–Al1 (Å)
Fe	9.0159	10.2419	9.0882	839.204	5.2032	3.4467	3.1726
Ru	9.1320	10.2871	9.1933	863.635	5.2604	3.4828	3.1971
Os	9.1386	10.2662	9.1852	861.744	5.2500	3.4711	3.1469

1.3.2 Magnetic, transport, and thermal properties of CeT_2Al_{10} (T = Fe, Ru, and Os)

Figures 1.31 (a)–(f) display the temperature variations of the resistivity $\rho(T)$ and magnetic susceptibility $\chi(T)$ for CeT_2Al_{10} (T = Fe, Ru, and Os) [66, 71, 72, 73, 75, 77, 78, 79, 83, 88, 98]. The CeT_2Al_{10} systems are classified into Kondo semiconductors because their $\rho(T)$ display semiconducting behaviors at high temperatures [66, 71, 72, 73, 98, 75, 77]. For T = Fe, where the c–f hybridization is strongest among the three, the ground state remains in a paramagnetic state [75, 77]. On the contrary, the compounds with T = Ru and Os undergo antiferromagnetic (AFM) orders at unexpectedly high temperatures T_N = 27.0 and 28.5 K, respectively, although the Ce moments are reduced to 0.3–0.4 μ_B/Ce by the Kondo effect [78, 83, 84].

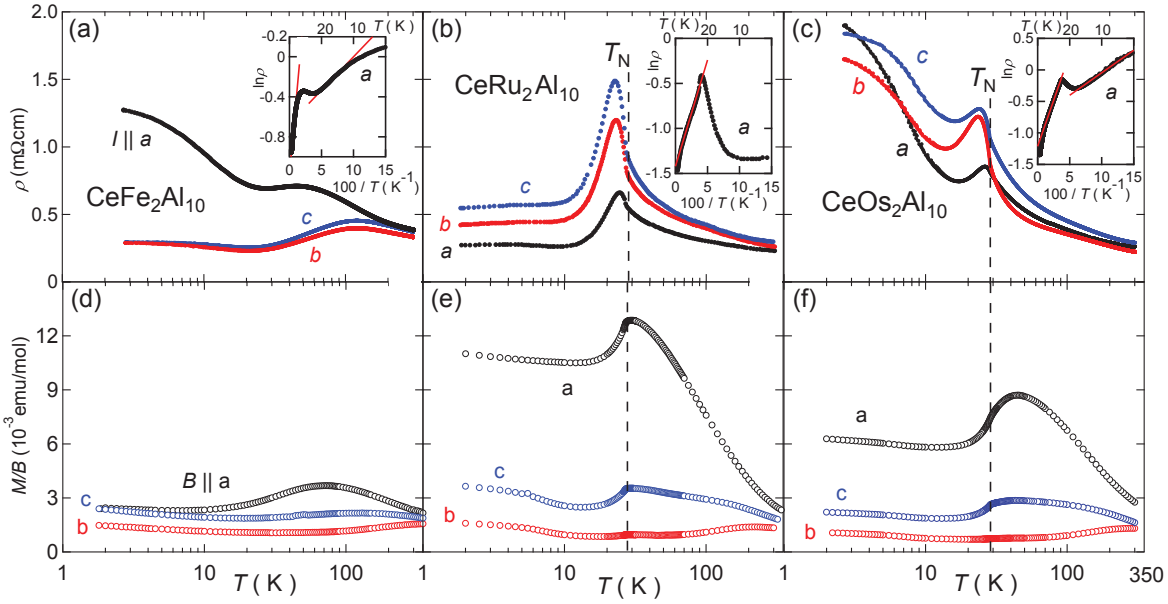

Figure 1.31: Temperature variations of the resistivity $\rho(T)$ and magnetic susceptibility $\chi(T)$ for CeT_2Al_{10} (T = Fe, Ru, and Os) [66, 71, 72, 73, 75, 76, 77, 98]. The dotted lines indicate the AFM ordering temperature T_N. The insets show the Arrhenius plot of $\rho(T)$.

Figure 1.32 shows the magnetic structure of CeT_2Al_{10} (T = Ru and Os) determined by neutron diffraction experiments [78, 83, 84]. As shown in Fig. 1.33, the magnetic Bragg peaks of (0 1 0) and (0 1 1) develop below 28.5 K for $CeOs_2Al_{10}$ [84]. In the AFM state, collinear AFM moments are aligned alternately along the c axis with the propagation vector of (0 1 0). It is noteworthy that the ordered Ce moments are oriented along the c axis although the a axis is the easy magnetization axis in the paramagnetic state [78, 83, 84]. We summarize the magnetic, transport, and thermal properties for the CeT_2Al_{10} systems in the next paragraph.

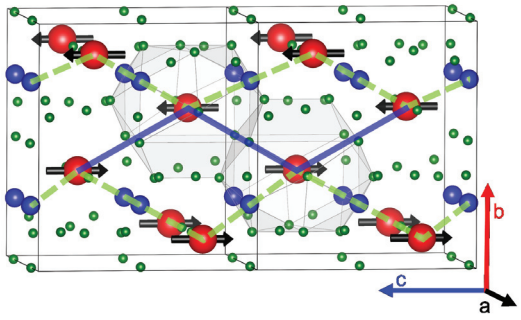

Figure 1.32: Antiferromagnetic structure of CeT_2Al_{10} (T = Ru and Os). The blue solid and green dotted lines represent the nearest Ce–Ce and Ce–T–Ce zigzag chains, respectively [68, 69, 66, 72, 75].

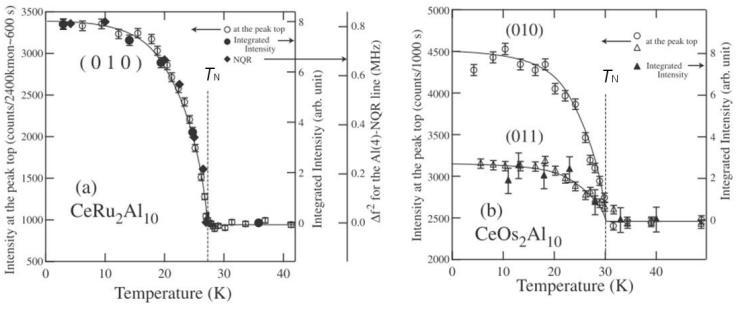

Figure 1.33: Temperature dependence of magnetic peak intensities of CeT_2Al_{10} with (a) T = Ru and (b) T = Os. The open symbols display the heights of the peak top and closed symbols are the integrated intensities.

The temperature dependence of the resistivity $\rho(T)$ for the Fe compound is shown in Fig. 1.31 (a). As shown by the ln$\rho(T)$ versus $100/T$ plot in the inset, a thermal activation behavior, $\rho(T) \propto \exp(\Delta/2k_{\rm B}T)$ with the transport gap Δ, appears in the two regions of 210 – 140 K and 21 – 11 K [75]. Moving our attention to the $\rho(T)$ data for $T =$ Ru and Os in Fig. 1.31 (b, c) [66, 71, 72, 73], we find that $-\log T$ dependence from 300 to 100 K is followed by a thermal activation-type behavior in the range of 80 – 30 K. By fitting the data in the inset of Fig. 1.31 (b, c), the values of $\Delta_a/k_{\rm B}$, $\Delta_b/k_{\rm B}$, and $\Delta_c/k_{\rm B}$ are estimated to be 42, 50, and 58 K for $T =$ Ru and 56, 83, and 65 K for $T =$ Os [72, 76], respectively. Below $T_{\rm N}$, $\rho(T)$ for $T =$ Ru and Os increases abruptly, which can be attributed to the formation of a superzone gap on the Fermi surface [90, 91]. The $T_{\rm N}$ was taken as the midpoint of the jump in the specific heat divided by temperature C/T, as will be described below. Such a superzone gap is formed by the folding of the Brillouin zone associated with the AFM order. Thereby, it should be taken into account that the Ce sublattice changes from the base-centered orthorhombic lattice in the paramagnetic state to the primitive orthorhombic lattice in the AFM ordered state, as shown in Fig. 1.34. Upon cooling below $T_{\rm N}$, $\rho(T)$ passes through a peak at 22 and 24 K for $T =$ Ru and Os, respectively. At $T <$ 20 K, $\rho(T)$ for $T =$ Ru decreases and becomes constant, whereas that for $T =$ Os continues to increase. The reason for this different behavior in $\rho(T)$ will be clarified later.

Figure 1.35 displays the thermopower $S(T)$. At a glance, we notice that the anisotropy in thermopower $S(T)$ is stronger than in $\rho(T)$ especially for $T =$ Os. Below 300 K, $S_i(T)$'s for the three compounds increase to a broad peak at the temperature T_{Smax}. At T_{Smax}, the absolute values of $S_a(T_{Smax})$ and $S_c(T_{Smax})$ increase from 10 μV/ K for $T =$ Ru, 20 μV/K for $T =$ Os, to 40 μV/K for $T =$ Fe. On the other hand, only along the b axis, $S(T_{Smax})$ for $T =$ Os is the largest among the three systems. Below $T_{\rm N}$ for $T =$ Ru and Os, S_a and S_c increase but S_b decreases. The reason for this anisotropic behavior in $S(T)$ will be discussed later.

The temperature variations of magnetic susceptibility $\chi(T)$ for $T =$ Fe are shown in Fig. 1.31 (d) [75, 77]. The $\chi(T)$ in $B \parallel a$ obeys the Curie-Weiss law from 300 to 100 K, and then passes through a broad maximum at around 75 K. The Curie-Weiss fit gives the paramagnetic Curie temperature $\theta_{\rm P} = -260$ K. The large negative value of $\theta_{\rm P}$ means

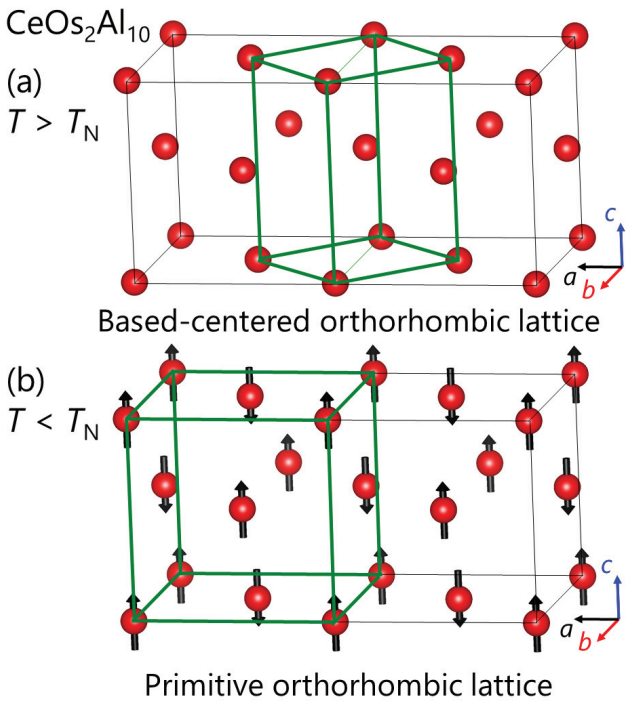

Figure 1.34: The Ce sublattice of $CeOs_2Al_{10}$ forms the base-centered orthorhombic lattice at $T > T_N$ and the primitive orthorhombic lattice at $T \leq T_N$ [72, 76].

strong c–f hybridization because $|\theta_P|$ is proportional to the Kondo temperature T_K [92]. In Fig. 1.31 (e, f), $\chi_a(T)$ for $T =$ Ru and Os also shows the Curie–Weiss behavior from 300 to 150 K, which is followed by the maximum at 30 and 45 K, respectively [66, 71, 72, 73, 98]. The magnitude of T_K was estimated as $3T_\chi$, where T_χ is the temperature at the maximum of the $\chi_a(T)$. Then, T_K increases from 90 K for $T =$ Ru, 135 K for $T =$ Os, to 220 K for $T =$ Fe. This increasing order in T_K for the three compounds is consistent with that in the effective hybridization strength, $V_{\rm eff}(T = \text{Ru}) < V_{\rm eff}$ $(T = \text{Os}) < V_{\rm eff}(T = \text{Fe})$, that was derived from the experiments of hard x-ray photoemission spectroscopy [79]. Below T_N, $\chi(T)$ along the three principal axes drop. This result was reproduced by the calculation by using the dynamical mean field theory and the continuous-time quantum Monte Carlo with the bipartite Kondo lattice model [82]. Moreover, the analysis of combined data of anisotropic magnetic susceptibility and x-ray absorption spectra indicated that the crystal-field ground state of the $4f$ state in the systems with $T =$ Ru and Os is dominated by $|J_z\rangle = |\pm 3/2\rangle$ when the c axis is taken as the quantization axis [80, 81]. The $4f$ state

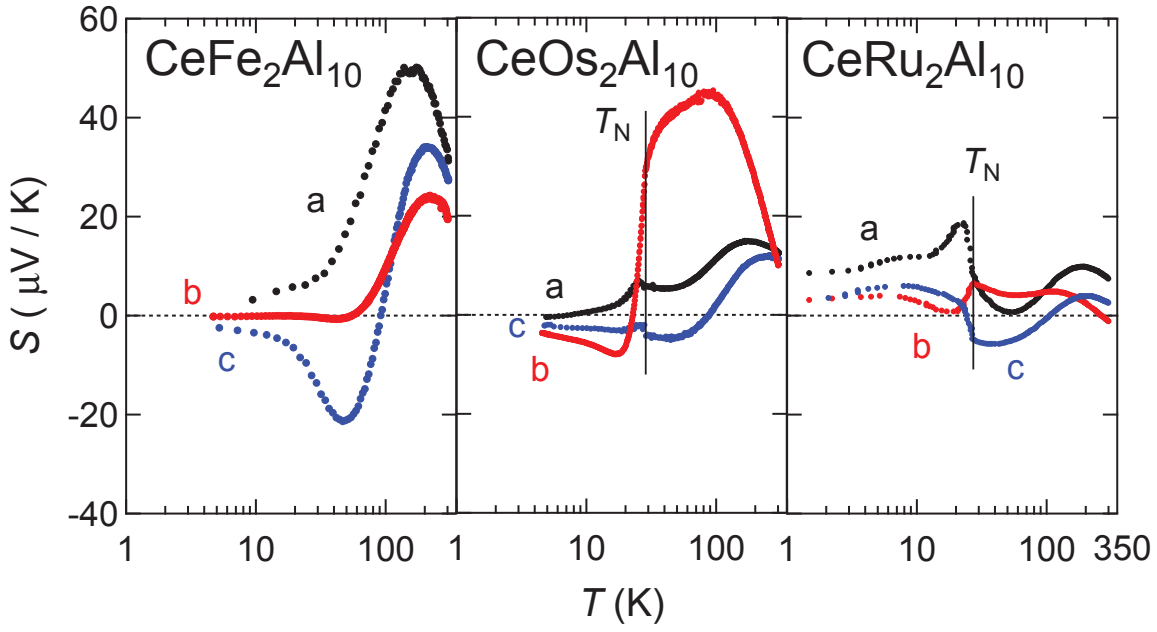

Figure 1.35: Temperature variations of themopower $S(T)$ along the three principal axes for single crystals of CeT_2Al$_{10}$ (T = Fe, Ru, Os). The AFM ordering temperatures T_N are denoted by solid lines [99].

with $|J_z\rangle = |\pm 3/2\rangle$ allows a pseudogap structure with residual DOS at E_F as shown in Fig. 1.23 and 1.22 [38, 51, 50, 52].

The temperature dependences of specific heat C divided by temperature, C/T, for CeT_2Al$_{10}$ are shown in Fig. 1.36 (a). That for the Fe compound displays no anomaly, whereas those for the Ru and Os compounds show sharp peaks. The midpoint temperature of the jump in C/T is taken as $T_N = 27$ and 28.5 K, as marked by the arrows in Fig. 1.36 (a). The extrapolation of the plot C/T vs T^2 in the inset of Fig. 1.36 gives the Sommerfeld coefficients $\gamma = 18$, 10, and 7 mJ/K^{2}mol for T = Fe, Ru, and Os, respectively. The rather large values of γ indicate the presence of residual DOS at E_F in the gapped state. This is in agreement with the calculation of the anisotropic gap with nodes for the orthorhombic Kondo semiconductors [38, 51, 50, 52]. Figure 1.36 (b) shows the temperature variations of the magnetic part of specific heat C_m plotted in the form of C_m/T for CeT_2Al$_{10}$. To

estimate the values of $C_{\rm m}$, the values of C for LaT_2Al$_{10}$ are subtracted from those of CeT_2Al$_{10}$. The $C_{\rm m}/T$ for T = Fe shows a broad maximum at 30 K, which may be attributed to the hybridization gap of 8.6 meV observed by neutron inelastic scattering (Fig. 1.17). For typical Kondo semiconductors CeNiSn (gap energy = 4.4 meV) and CeRhSb (gap energy = 7.7 meV), the maximum in $C_{\rm m}/T$ was explained by the Lorentzian DOS with a V-shaped gap [39, 40, 41]. For T = Ru and Os, however, sharp peaks appear at $T_{\rm N}$ in the $C_{\rm m}/T$, respectively, where the jump for T = Ru is much larger than that for T = Os. Below $T_{\rm N}$, $C_{\rm m}/T$s decrease exponentially, following the description of AFM magnon dispersion ($C_{\rm m}/T \propto T^2 \exp(-\Delta_{\rm m}/T)$), where $\Delta_{\rm m}$ is the magnon gap. The inset of Fig. 1.36 (b) shows the magnetic entropy $S_{\rm m}$ estimated by integrating $C_{\rm m}/T$ versus T over the entire temperature range. At $T_{\rm N}$, $S_{\rm m}$ bends downward at the values 0.65 Rln2 for T = Ru and 0.35 Rln2 for T = Os.

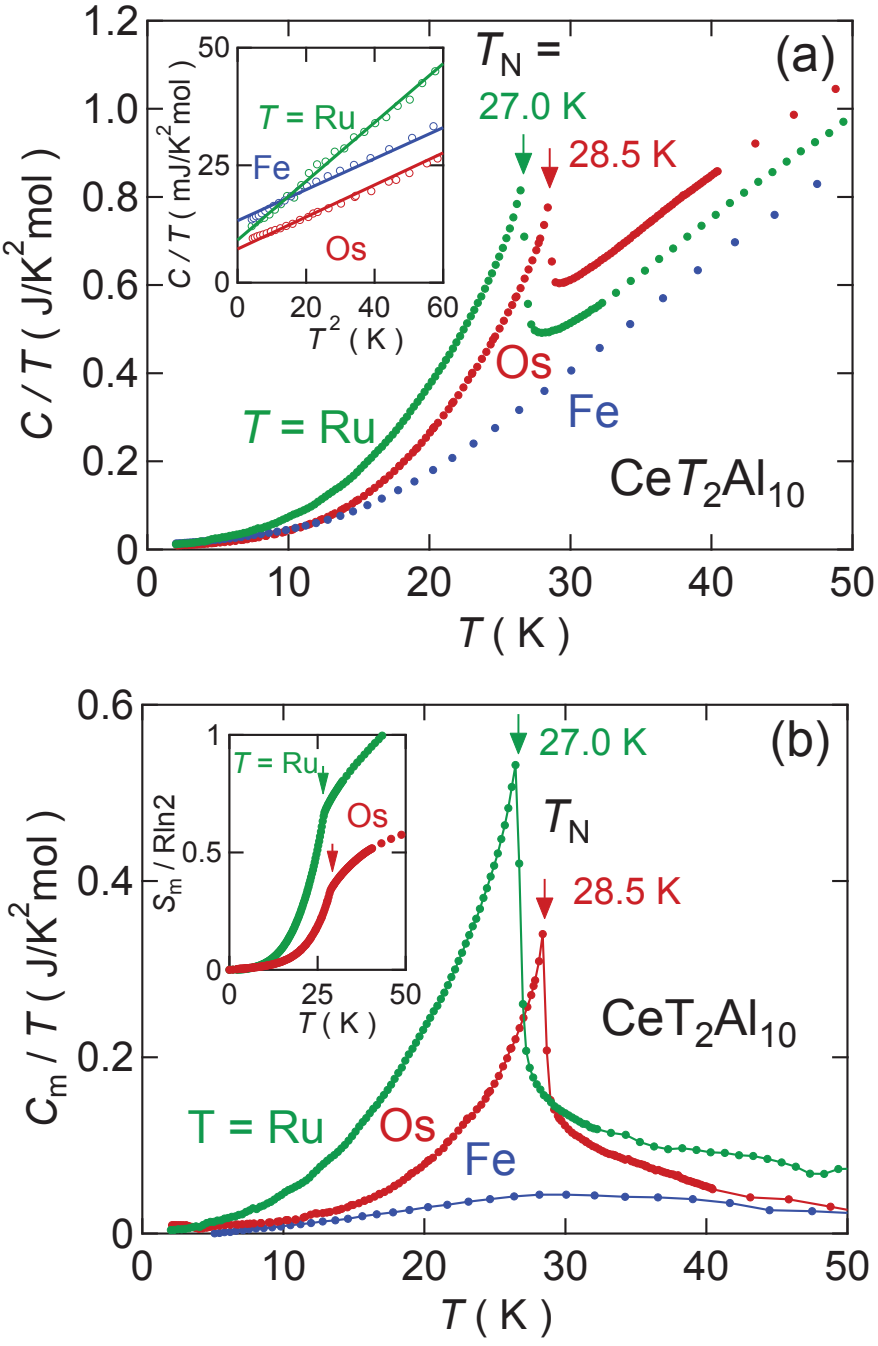

Figure 1.36: Temperature dependences of the specific heat C and magnetic part $C_{\rm m}$ plotted in the forms of (a) C/T and (b) $C_{\rm m}/T$ for CeT_2Al_{10} (T = Fe, Ru, and Os) [66, 71, 72, 73, 75, 76, 77, 98]. The arrows indicate $T_{\rm N}$ at the midpoint of the jump in C/T. The insets of (a) and (b), respectively, show C/T vs T^2 and the magnetic entropy $S_{\rm m}$ divided by Rln2 vs T.

Out of de Gennes scaling of T_N

Figure 1.37 shows the magnetic transition temperatures of the series of $Ln\mathrm{Os_2Al_{10}}$ (Ln = Ce, Nd, Sm, and Gd) versus the de Gennes factor $dG = (g_J - 1)^2 J(J+1)$, where g_J is the Landé g-value and J is the total angular momentum of $\mathrm{Ln^{3+}}$ ion [71, 88, 89]. For R = Ce, a large deviation from the dG scaling by factors of 150 is seen. Namely, T_N for $\mathrm{CeOs_2Al_{10}}$ with 0.3 μ_B/Ce is higher than those of the Gd counterpart with 7μ_B/Gd. This fact indicates that the high T_N for $\mathrm{Ce}T_2\mathrm{Al_{10}}$ (T = Ru and Os) can not be explained by the simple RKKY interaction between the localized magnetic of moments of $\mathrm{Ce^{3+}}$ ions. We need to take into account of the c-f hybridization effect and crystal field effect.

Gap structures

The gap formation in $\mathrm{Ce}T_2\mathrm{Al_{10}}$($T$ = Fe, Ru, Os) has been investigated by nuclear quadruple resonance (NQR) [85, 86, 87], photoemission spectroscopy [94], and optical conductivity [95, 96]. Figure 1.38 shows the temperature variation of ^{27}Al nuclear spin-lattice relaxation rate $1/T_1$ at the Al(5) site. On cooling $\mathrm{CeFe_2Al_{10}}$, $1/T_1$ decreases and behaves as T_1T = const (Korringa law). The T-dependence is similar to that in the Kondo semiconductors CeNiSn and CeRhSb, implying that the gap develops in $\mathrm{CeFe_2Al_{10}}$ leaving a residual $N(E)$ at E_F. In fact, the calculated $1/T_1$ under the assumption of V-shaped density of states is drawn by the solid line in Fig. 1.38, which reproduces experimental data for T = Fe. However, $1/T_1$ for $\mathrm{Ce}T_2\mathrm{Al_{10}}$ (T = Ru and Os) drastically decreases at around T_N and deviates from the calculation for the V-shaped DOS.

Figure 1.39 displays the energy dependences of PES spectra for $\mathrm{Ce}T_2\mathrm{Al_{10}}$ at various temperatures. Upon cooling the sample with T = Fe, two hybridization gaps successively appear in the PES spectra, while one hybridization gap and an AFM gap open for T = Ru and Os [94]. At around T_N, no obvious reduction in the DOS at E_F was observed.

The polarized optical conductivity spectra $\sigma(\omega)$ with the electric field along the orthorhombic principal axes are represented in Fig. 1.40 (a)–(c) [95, 96]. Broad shoulders gradually evolve on cooling at around 55, 45, and 40 meV, respectively, for T = Fe, Os, and Ru. The shoulders were attributed to hybridization gap because the shoulders are similar to those of typical KSs as shown in Fig. 1.19. Furthermore, it is remarkable that a peak develops at 20 meV only along the b axis for T = Ru and Os, as shown in Fig. 1.40

(d, e), respectively. Figure 1.40 (f) displays the temperature dependence of effective electron numbers ($N_{\rm eff}$) involved in the shoulders for T = Ru and Os. The effective electron number ($N_{\rm eff}$) was calculated by using the function,

$$N_{\rm eff} = \frac{4m_0}{h^2e^2} = \int_0^\infty \Delta\sigma(\hbar\omega)\ d\hbar\omega, \tag{1.23}$$

where h is the Planck constant, e is elementary charge, and m_0 is the electron rest mass. The shape of the back ground originating from the c-f hybridization gap is almost linear with the energy. In order to evaluate the intensity of the peak at 20 meV, the intensity for the background was subtracted from the total $\sigma(\hbar\omega)$ as shown in Fig. 1.40 (d). The temperature dependence of $N_{\rm eff}$ indicates that the peak structures at 20 meV evolve as temperature decreases below 32 K for T = Ru and 38 K for T = Os.

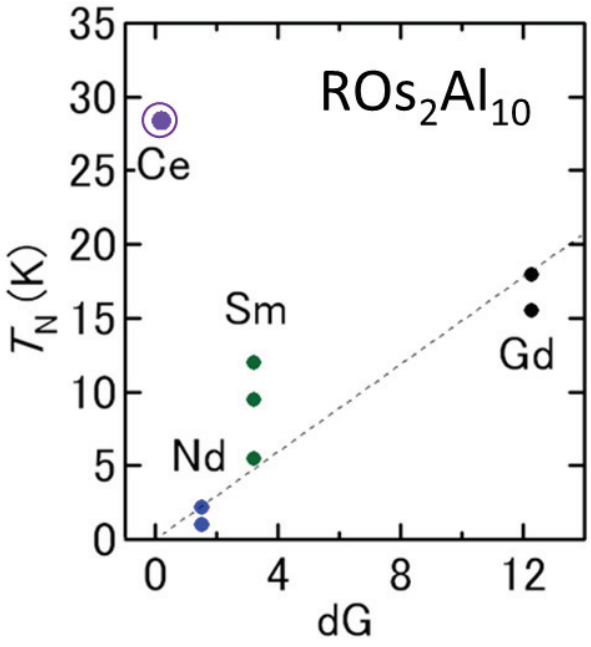

Figure 1.37: Magnetic transition temperatures of the series of LnOs$_2$Al$_{10}$ (Ln = Ce, Nd, Sm, and Gd) against the de Gennes factor $dG = (g_J - 1)^2 J(J+1)$ [71, 88, 89].

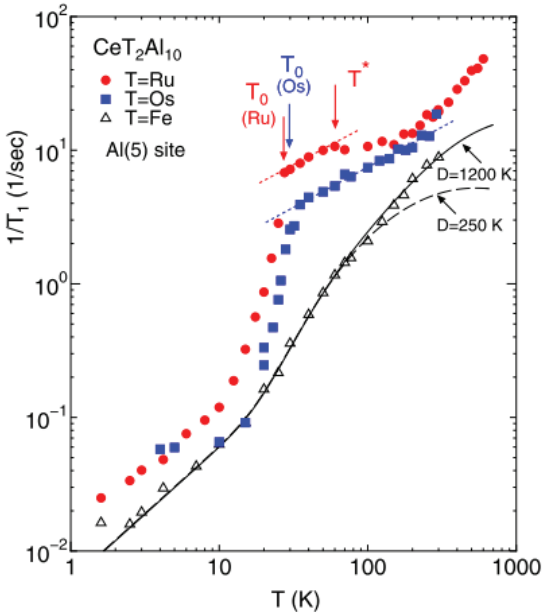

Figure 1.38: Temperature dependences of nuclear spin-lattice relaxation rate of ^{27}Al NQR in CeT_2Al$_{10}$ (T = Fe, Ru, and Os) [85, 86, 87].

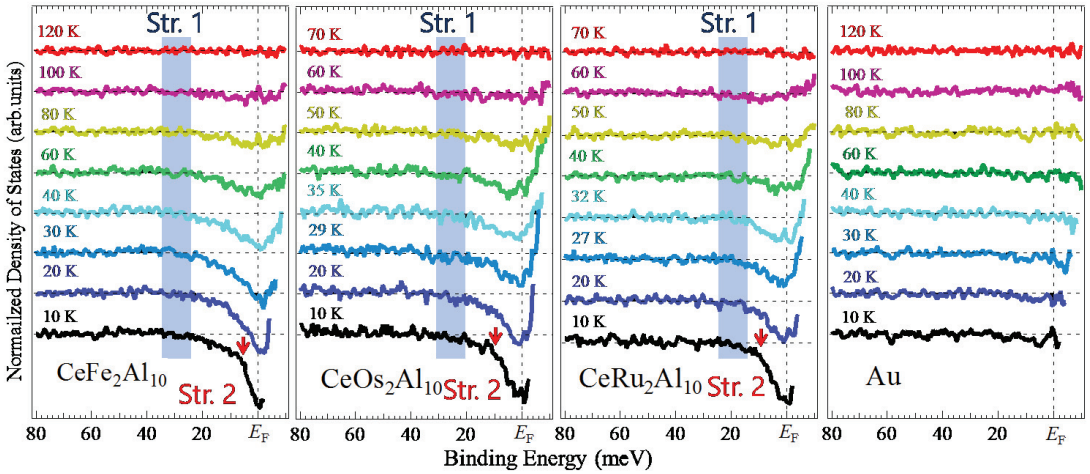

Figure 1.39: Temperature variations of PES spectra near E_F for CeT_2Al$_{10}$ (T = Fe, Ru, and Os) and gold [94]. The blue belts represent the energy region where the DOS decreases due to the opening of the hybridization gap. The red arrows indicate the shoulder structures.

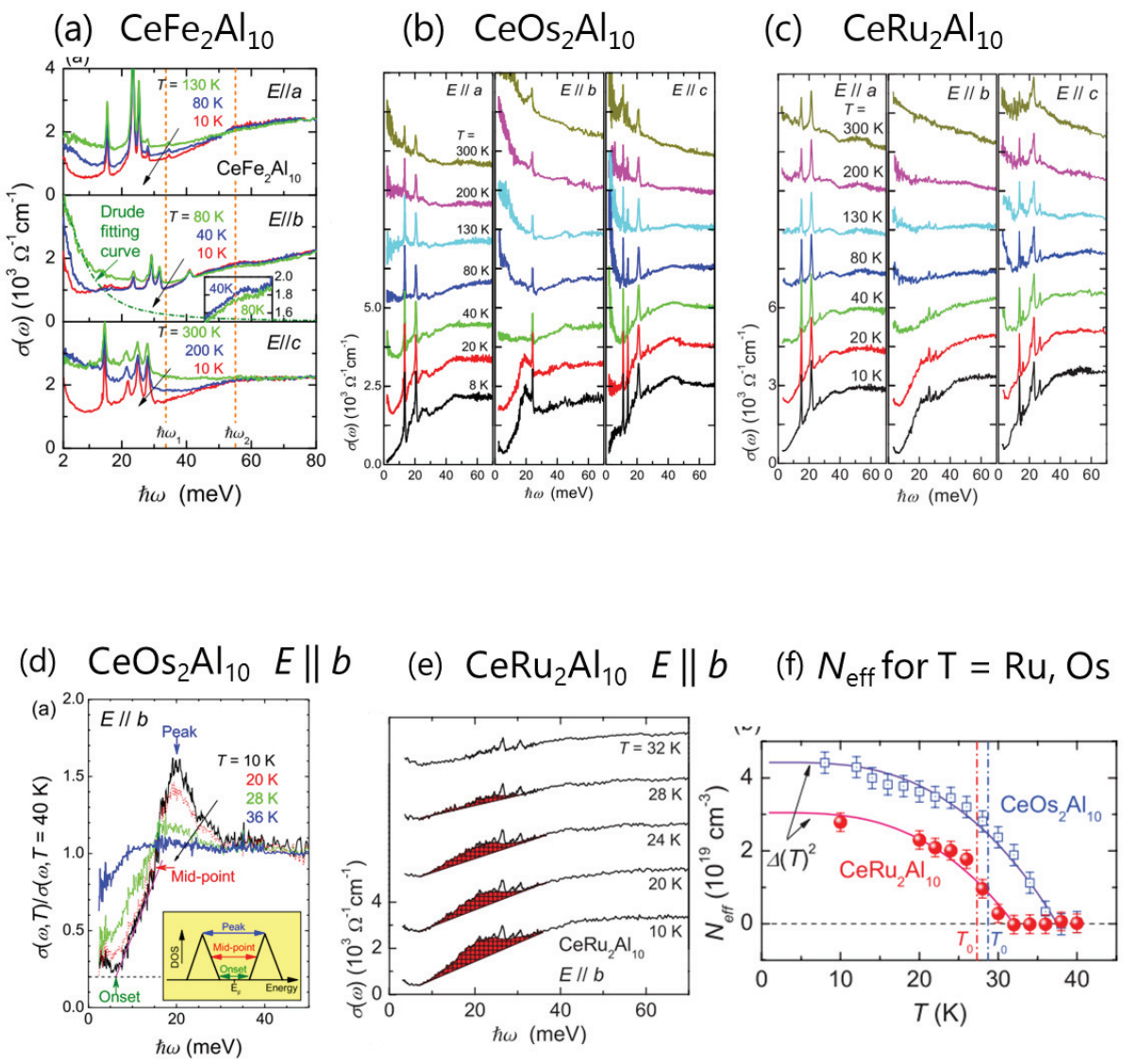

Figure 1.40: Temperature dependences of optical conductivities of CeT_2Al_{10} for T = (a) Fe, (b, d) Os, and (c, e) Ru [95, 96]. (f) Temperature dependence of effective electron number ($N_{\rm eff}$) involved in the shoulder structure at around 20 meV for $E \parallel b$.

1.3.3 Pressure effects on the magnetic and transport properties of CeT_2Al_{10} (T = Fe, Ru, and Os)

Figures 1.41 (a) and 1.42 (a)–(c) show the temperature dependences of magnetic susceptibility $\chi(T)$ of $CeOs_2Al_{10}$ along the orthorhombic principal axes and electrical resistivity $\rho(T)$ along the a axis of CeT_2Al_{10} (T = Fe, Ru, and Os) under various hydrostatic pressures, respectively [77, 97, 98]. In $\chi_a(T)$ and $\chi_c(T)$ for T = Os, the maxima at 45 K are suppressed and the temperatures at the maxima increase under pressure, indicating the increase in T_K. Furthermore, $\rho(T)$ for T = Ru at P = 2.0 GPa is similar to that of T = Os at ambient pressure. These changes in $\chi(T)$ and $\rho(T)$ suggest the enhancement of c-f hybridization by pressure. At $P > 1.58$ GPa, $\rho(T)$ for T = Os no longer exhibits the thermal activation behavior at $T > T_N$, although a broad maximum manifests at $T_{\rho m}$ which is followed by a metallic behavior below 30 K. By applying pressure up to 3 GPa on the three systems, $\rho(T)$ becomes metallic at low temperatures. The metalization in $\rho(T)$ implies that the ground state changes from the KS state to the metallic valence fluctuating state by the enhancement of the c-f hybridization.

Let us focus on the relation between T_N and the activation behaviors in $\rho(T)$ above T_N, which temperature is determined as the bend in $\rho(T)$. Figure 1.41 represents (b) T_N for T = Ru and Os, and (c) thermal activation energy Δ_H and Δ_L in $\rho(T)$ as a function of pressure. With increasing pressure up to ∼2 and 1 GPa, the T_N's of T = Ru and Os increase and disappear suddenly at P_c = 4.0 and 2.5 GPa, respectively. On the other hand, the activation energy Δ_H above T_N for T = Os decreases and vanishes above ∼1 GPa. These behaviors seem to imply that the gap formation at $T > T_N$ is not necessary for the AFM transition. However, $\rho(T)$ may exhibit such a metallic behavior if in-gap states develops within the hybridization gap, as shown in Fig. 1.26. Therefore, it is important to observe directly the gap structures by the photoemission spectroscopy, optical conductivity, and tunneling spectroscopy.

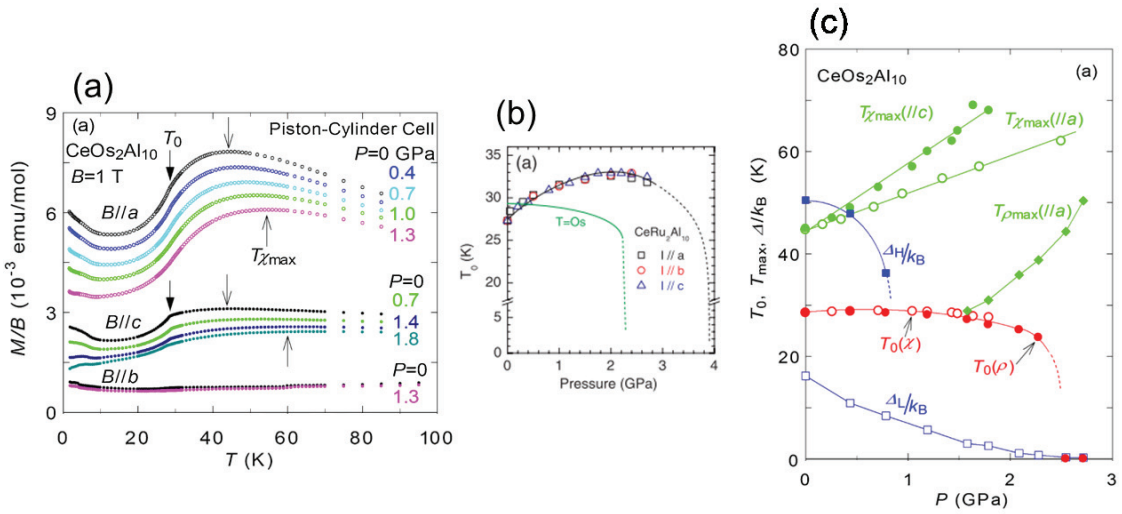

Figure 1.41: Pressure dependences of (a) the magnetic susceptibility $\chi(T)$ along the orthorhombic principal axes for $CeOs_2Al_{10}$ [97], (b) T_N for CeT_2Al_{10} (T = Ru, Os) [98], and (c) activation energies Δ_H/k_B above $T > T_N$ and Δ_L/k_B below T_N for $CeOs_2Al_{10}$ [97].

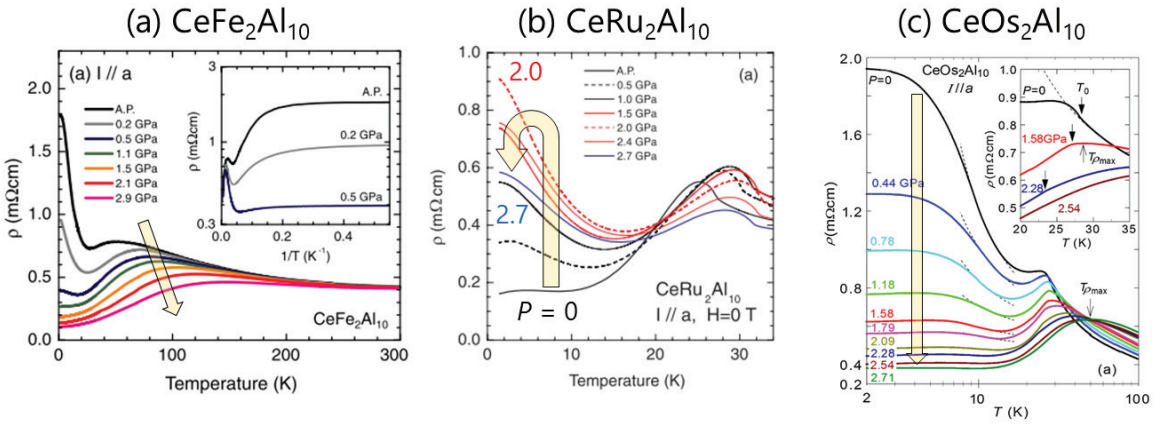

Figure 1.42: Temperature dependences of the electrical resistivity $\rho(T)$ along the a axis for CeT_2Al_{10} (T = Fe, Ru, and Os) under various pressures [77, 97, 98].

1.3.4 Doping effects on the magnetic, transport, and optical properties of $CeRu_2Al_{10}$

The effects of La, Re, and Rh substitutions on $CeRu_2Al_{10}$ have been investigated by the measurements of the magnetic, transport and optical properties [99, 100, 101, 102, 103, 104, 105, 106, 107]. Figure 1.43 (a) displays the temperature variations of $\chi^{-1}(B \,||\, a)$ for $Ce_{1-z}La_zRu_2Al_{10}$, whose value is normalized per Ce mol [99]. With increasing z, the linear temperature dependences in $1/\chi_a(T)$ above 100 K hardly change, indicating no change in the valence state of the Ce ion. Thus, the La substitution does not alter the c-f hybridization at high temperatures. The neutron diffraction study of $Ce_{1-z}La_zRu_2Al_{10}$ showed that the La substitution with $z = 0.1$ changes the direction of $\mu_{\rm AF}$ form the c axis to the b axis [100]. In $Ce(Ru_{1-y}Re_y)_2Al_{10}$, on the other hand, the maximum in $\chi_a(T)$ at around 30 K is suppressed as $2y$ increases from 0 to 0.1, as shown in Fig. 1.43 (b) [101]. The magnitude of $\mu_{\rm AF}$ also decreases from 0.4 $\mu_{\rm B}$/Ce for $2y = 0$ to 0.2 $\mu_{\rm B}$/Ce for $2y = 0.06$ [102]. Moreover, the direction of $\mu_{\rm AF}$ changes from the c axis for $2y = 0$ to the b axis for $2y = 0.06$. By contrast, in $Ce(Ru_{1-x}Rh_x)_2Al_{10}$, the maximum in $\chi_a(T)$ changes to a sharp peak with the fivefold increase in the height as $2x$ is increased to 0.46 [103, 104]. At $2x = 0.06$, $\mu_{\rm AF}$ changes the direction from the c axis to the a axis with the increase in the size to $\mu_{\rm AF} = 1.06$ $\mu_{\rm B}$/Ce [105]. These results reveal that the $4f$ state in $CeRu_2Al_{10}$ is more delocalized by Re-substitution but localized by Rh-substitution [101, 102, 103, 105]. As noted above, the La-, Re-, and Rh- substitutions in $CeRu_2Al_{10}$ change the c-f hybridization as well as the direction of $\mu_{\rm AF}$ in largely different ways.

The $\rho(T)$ data for La- and Rh- substituted systems are shown in Figs. 1.44 (a) and (b), respectively [103, 104, 106]. For the non-doped sample, $\rho(T)$ displays the thermal activation-type behavior in the region of 30 – 80 K. With increasing z and $2x$, it changes to -log T dependences, implying that the activation energy Δ decreases by both substitutions. Furthermore, as shown in Figs. 1.45 and 1.46, $T_{\rm N}$ is suppressed and γ value is increased with the increase of x, y, and z [99, 101, 103, 104, 106]. The degree of changes in $T_{\rm N}$ and γ for the Re-substituted system is stronger than those for the La-substituted system.

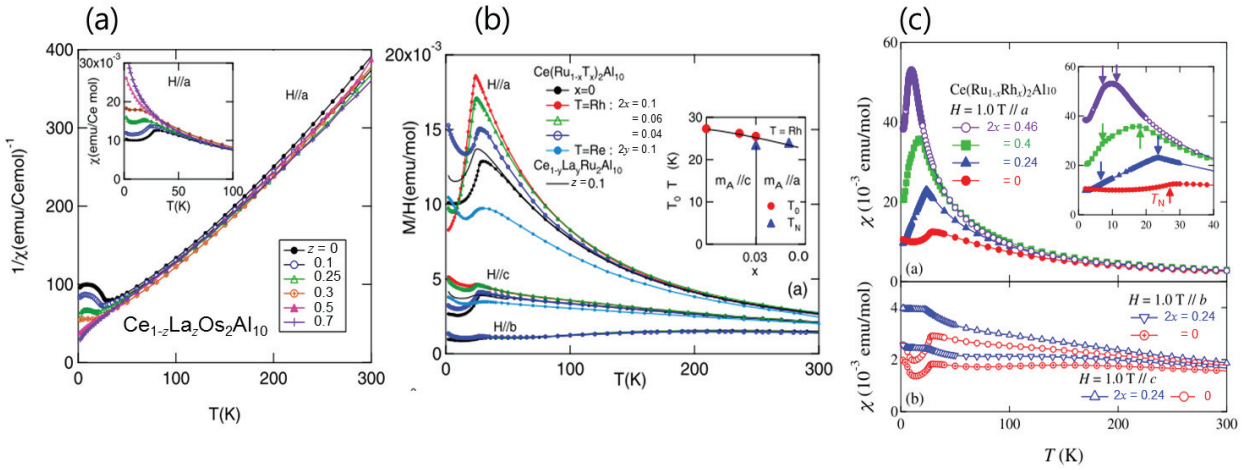

Figure 1.43: Temperature variations of the magnetic susceptibility $\chi_i(T)$ ($i = a$, b, c) of (a) $Ce_{1-z}La_zRu_2Al_{10}$ [99], (b) $Ce(Ru_{1-y}Re_y)_2Al_{10}$ [101], and (c) $Ce(Ru_{1-x}Rh_x)_2Al_{10}$ [103, 104].

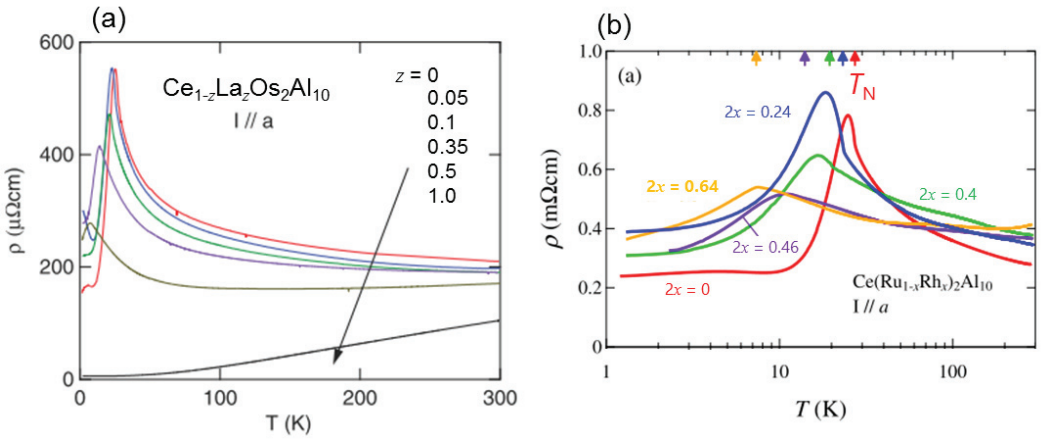

Figure 1.44: Temperature dependences of the electrical resistivity ρ ($I \parallel a$) for (a) $Ce_{1-z}La_zRu_2Al_{10}$ [106] and (b) $Ce(Ru_{1-x}Rh_x)_2Al_{10}$ [103, 104].

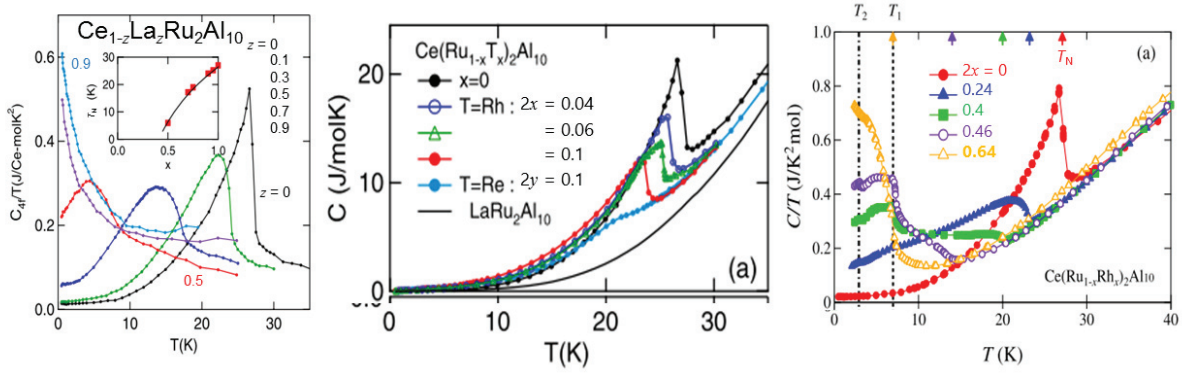

Figure 1.45: Temperature dependences of the specific heat C and magnetic part $C_{\rm m}$ for La-, Re-, Rh- substituted $CeRu_2Al_{10}$ [99, 101, 103, 104].

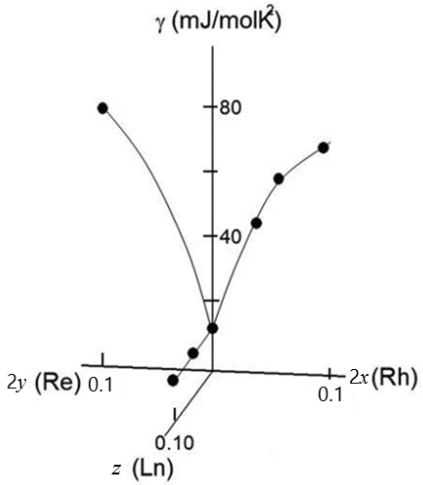

Figure 1.46: γ values in the specific heats of $Ce_{1-z}La_zRu_2Al_{10}$, $Ce(Ru_{1-y}Re_y)_2Al_{10}$, and $Ce(Ru_{1-x}Rh_x)_2Al_{10}$ as functions of x, y, and z [101].

Optical conductivity in $Ce(Ru_{1-x}Rh_x)_2Al_{10}$

Figure 1.47 (a) represents the optical conductivity spectra $\sigma(\omega)$ for $E \parallel b$ in $Ce(Ru_{1-x}Rh_x)_2Al_{10}$ for $2x = 0$, 0.06, and 0.1 [107]. For the non-doped sample, there are a broad shoulder at 40 meV and a peak structure at 20 meV. As $2x$ is increased to 0.1, the intensity of the hybridization gap is strongly suppressed, whereas the 20 meV peak is weakly suppressed (Fig. 1.47 (b)) [107]. These observations were interpreted as suggesting that the AFM order is related to the charge excitation gap along the b axis rather than the hybridization gap. However, we wonder that exact estimation of the intensity of the hybridization gap is difficult due to the large contributions of the Drude and interband transition terms.

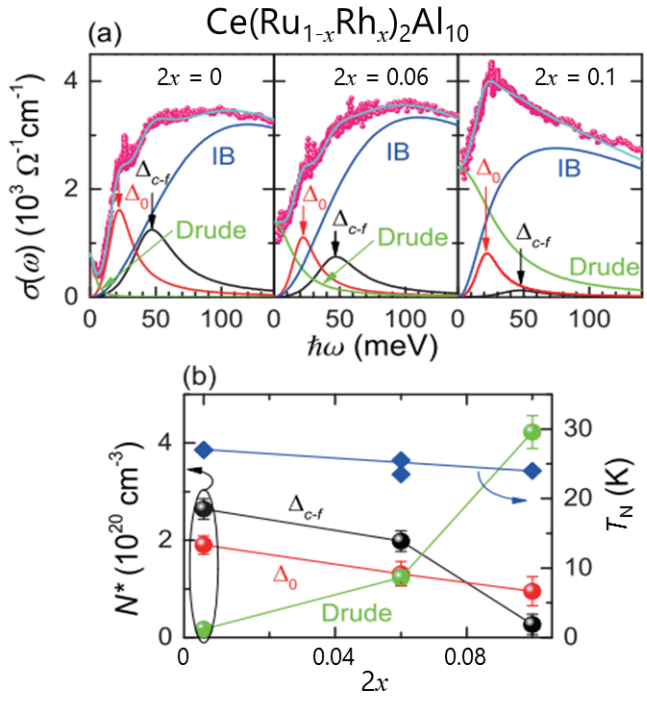

Figure 1.47: (a) Optical conductivity $\sigma(\omega)$ along the b axis at 10 K. The solid lines are the lines fitted with one Drude term and three Lorentz functions (assumed as peaks of the charge excitation Δ_0, c-f hybridization gap Δ_{cf}, interband transition (IB)). (b) Effective electron numbers of Drude, Δ_0, and Δ_{cf} components together with the AFM temperature T_N as a function of x in $Ce(Ru_{1-x}Rh_x)_2Al_{10}$ for $2x = 0$, 0.06, and 0.1 with $T_N = 27.0$, 25.5, and 23.5 K, respectively [107].

1.4 Purpose of the present study

In rare-earth based Kondo semiconductors (KSs), a narrow gap develops in the *c*-*f* hybridized bands at E_F [2, 3, 4, 27]. Neither of them ordered magnetically because the $4f$ local moments are coherently screened by the conduction electron spins as the consequence of the *c*-*f* hybridization effect. In the new family of KSs, CeT_2Al_{10} (T = Ru and Os), however, AFM orders have been observed at T_N = 27 and 28.5 K, respectively. The comparison of magnetic and transport properties between $CeRu_2Al_{10}$ and $CeOs_2Al_{10}$ indicated that $CeOs_2Al_{10}$ is located closer to the critical point where the unusual AFM disappears. Here, it evoked a question of why the T_Ns with small magnetic moments 0.3 – 0.4 μ_B/Ce are higher than those for the Gd compounds with $7\mu_B$/Gd. For T = Os, the value of transport gap was estimated as $\Delta/k_B = 50 - 80$ K. The magnetic, thermal, and x-ray absorption measurements have indicated that a pseudogap opens in the quasiparticle DOS leaving a residual DOS at E_F [71, 72, 78, 80, 83]. In facts, the Sommerfeld coefficient of $CeOs_2Al_{10}$ is as large as 7 mJ/K^2 mol. The residual DOS makes it difficult to judge the presence of the hybridization gap solely from the resistivity data. Therefore, it is important to probe directly the opening of hybridization gaps by other methods.

The present study aims to clarify the relation between the *c*-*f* hybridization gap and the unusual magnetic order in $CeOs_2Al_{10}$. For this purpose, we have prepared samples of La-, Re-, and Ir-substituted $CeOs_2Al_{10}$. Substitutions of La for Ce and Re/Ir for Os are expected to dope a $4f$ hole and a $5d$ hole/electron in $CeOs_2Al_{10}$, respectively. As mentioned above, previous studies of CeNiSn by doping $3d$ electrons and holes provided us with important information on the relation between the hybridization gap and magnetism. From these results, we expected that the *c*-*f* hybridization is enhanced/suppressed by doping holes/electrons because the Fermi energy E_F would decrease/increase as shown in Fig. 1.48. The enhancement/suppression of *c*-*f* hybridization should change the hybridization gap and T_N. Bearing this in mind, we have measured the magnetic susceptibility, electrical resistivity, thermopower, and specific heat as well as tunneling spectra of doped sample. Neutron scattering experiments have been performed on our samples. The results of doping effects on $CeOs_2Al_{10}$ will be discussed by comparing with those of $CeRu_2Al_{10}$.

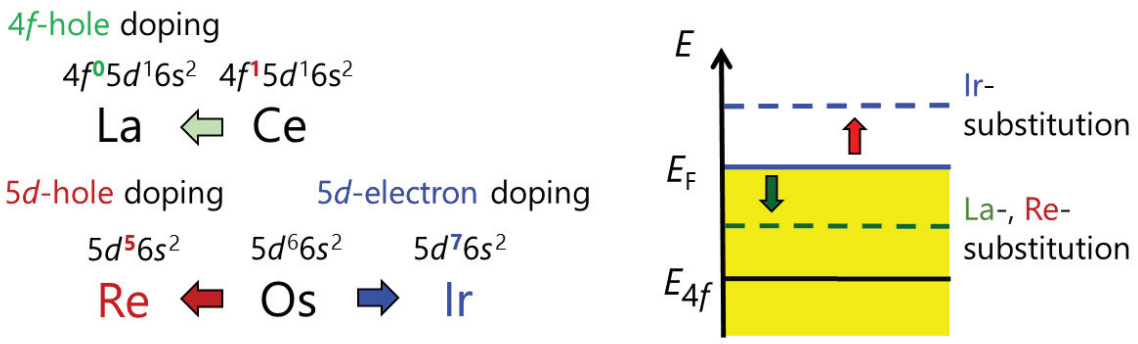

Figure 1.48: Espected effects of doping of $4f$ holes and $5d$ holes/electrons on the electronic states in $CeOs_2Al_{10}$.

Chapter 2

Sample preparation and characterizations

2.1 Crystal growth of CeT_2Al_{10} (T = Fe, Ru, and Os) and substituted $CeOs_2Al_{10}$

Firstly, we have examined the solubility of Re and Ir in $Ce(Os_{1-y}Re_y)_2Al_{10}$ and $Ce(Os_{1-x}Ir_x)_2Al_{10}$ by preparing polycrystalline samples with the nominal compositions of Re and Ir up to 50%. Starting materials of Ce, Os + Re/Ir, and Al with the ratio of 1 : 2 : 10 were arc-melted into polycrystalline ingots under an Ar atmosphere purified by the titanium getter. The ingots were annealed in an evacuated quartz ampoule at 850°C for seven days [75]. Starting materials are listed in Table 2.1.

Single crystals of CeT_2Al_{10} (T = Fe, Ru, and Os) and those substituted by La, Re, and Ir were grown using an Al self-flux method [72]. First, Ce (La) lump and crashed balls of Fe, Ru, and Os (Re/Ir) were arc-melted into an ingot of about 3 g. The ingot of CeT_2 was turn over and was melted several times to make it homogeneous. To avoid chemical reaction between Al and the quartz tube, we used magnesia and alumina crucibles, which were degassed in vacuum at high temperature. The crushed CeT_2 ingot and pieces of Al in the ratio of 1 : 30 were loaded into a magnesia crucible for T = Fe (Nikkato, MG-12G) and an alumina crucible for T = Ru and Os (Nikkato, SSA-H T2). The crucibles of 50 mm in length and 11.4 mm of inner diameter were sealed in a quartz ampoule under an Ar

atmosphere of 1/3 atm, as shown in Fig. 2.1. Beforehand, the quartz ampoule was burned by flames to remove water and impurities. Figures 2.2 and 2.3 display the temperature programs for the crystal growth of CeT_2Al_{10} (T = Fe, Ru, and Os) and substituted ones. $CeFe_2Al_{30}$ in the magnesia crucible was heated to 900°C, kept for 12 hours, and then slowly cooled at a rate 2°C/h (Fig. 2.2). On the other hand, CeT_2Al_{30} (T = Ru and Os) or substituted samples in the alumina crucible were heated to 1200°C for 5 hours and then cooled at a rate 2°C/h (Fig. 2.3).

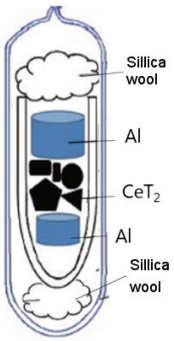

Figure 2.1: Crushed CeT_2 ingot and pieces of Al sealed in a quartz ampoule under an Ar atmosphere of 1/3 atm. The silica wool was placed above and below the crucible made of magnesia or alumina.

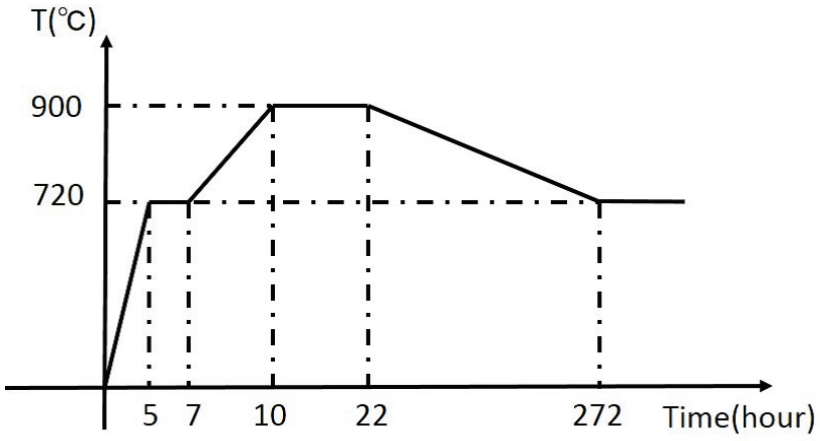

Figure 2.2: Temperature program as a function of time for the growth of single crystals of $CeFe_2Al_{10}$.

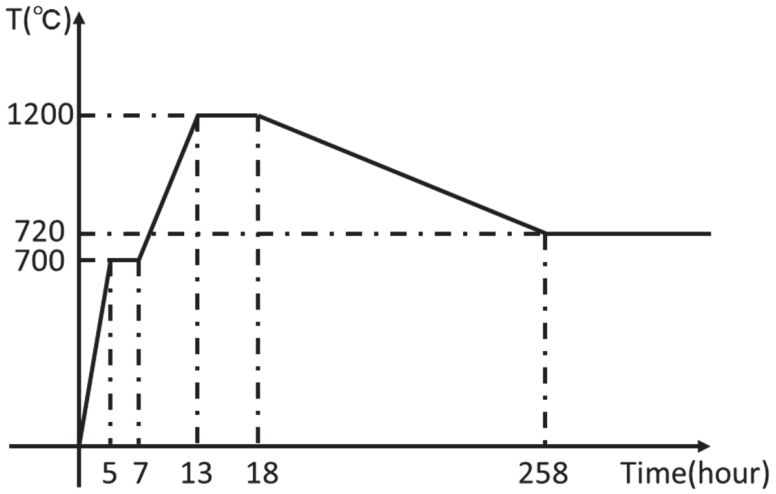

Figure 2.3: Temperature program as a function of time for the growth of single crystals of CeT_2Al_{10} (T = Ru and Os), $Ce_{1-z}La_zOs_2Al_{10}$, $Ce(Os_{1-y}Re_y)_2Al_{10}$, and $Ce(Os_{1-x}Ir_x)_2Al_{10}$.

Table 2.1: Starting materials for the sample of CeT_2Al_{10} and substituted one.

Materials	Suppliers	Purity	Shape
Ce	Johnson Matthey ♯ 40284 ♯ I02 W058	3N	Lump
Ce	Ames Lab. MPC ♯ 3031M-33	4N	Rod 6ϕ
La	Ames Lab. MPC ♯ M001	4N	Rod 6ϕ
Fe	Rare Metallic ♯ 628-34	4N	Ingot
Ru	Tanaka Kikinzoku ♯ 02973	3N	Powder
Os	Tanaka Kikinzoku ♯ 8 89740206	3N	Powder
Ir	Tanaka Kikinzoku ♯ 0482	3N	Powder
Re	Nilaco ♯ 361483	3N	Wire 2ϕ
Al	Koujundo Chem. Lab. No.376321	5N	Ingot
Al	Alfa Aesar ♯ 10779 ♯ L08U26	5N	Ingot

2.2 Characterizations of samples

The samples were characterized by combining powder x-ray diffraction (Rigaku Ultima-IV) with Cu target (TOSHIBA Copper-A-41, $V = 40$ kV and $I = 30$ mA), Laue back diffraction (TRYSE TRY-IPLC) with W target (TOSHIBA Tungsten-A-40, $V = 25$ kV and $I = 20$ mV). The chemical composition was determined by the wavelength dispersive electron-probe microanalysis (EPMA, JEOL JXA-8200). From the powder X-ray diffraction patterns, the crystallographic structures and the lattice parameters have been determined by the analysis software RIETAN-FP [115]. Back scattered electron (BSE) images of the polished surface of the samples were observed by the EPMA system operated at 20 keV.

2.2.1 X-ray diffraction

Figures 2.4 and 2.5 show the powder x-ray diffraction patterns of the polycrystalline sample of $Ce_{1-z}La_zOs_2Al_{10}$, $Ce(Os_{1-y}Re_y)_2Al_{10}$, and $Ce(Os_{1-x}Ir_x)_2Al_{10}$ in the diffraction rage of $10^\circ \leq 2\theta \leq 120^\circ$. The diffraction patterns indicated that the $YbFe_2Al_{10}$-type structure is kept in the ranges $z \leq 1$, $y \leq 0.5$, and $x \leq 0.4$. The lattice parameters are plotted in Figs. 2.6 and 2.7. With increasing z and y, the orthorhombic lattice parameters increase, whereas the a and c parameters decrease with increasing x. Since the change is smaller than 0.3% for $z \leq 1.0$, $y \leq 0.1$, and $x \leq 0.2$, we expect that the chemical pressure effect on the c-f hybridization may be much weaker than that of doping of $4f/5d$ holes and electrons.

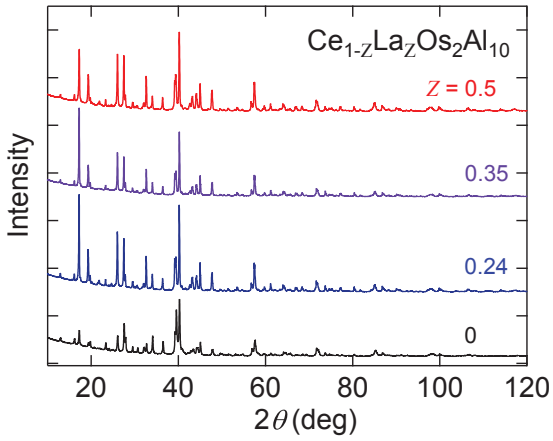

Figure 2.4: Powder x-ray diffraction patterns of polycrystalline samples of $Ce_{1-z}La_zOs_2Al_{10}$.

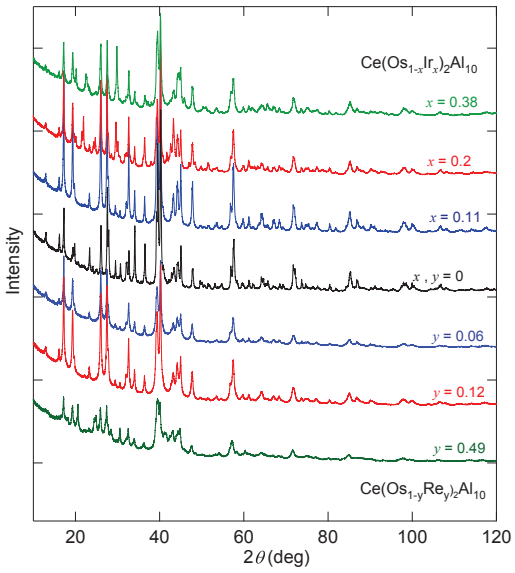

Figure 2.5: Powder x-ray diffraction patterns of polycrystalline samples of $Ce(Os_{1-x}Ir_x)_2Al_{10}$ and $Ce(Os_{1-y}Re_y)_2Al_{10}$.

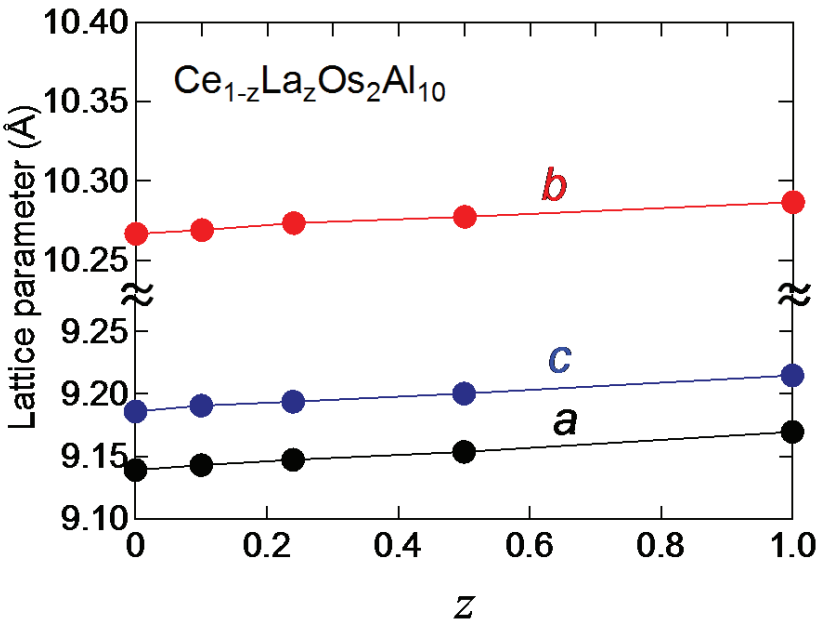

Figure 2.6: Orthorhombic lattice parameters of polycrystalline samples of $Ce_{1-z}La_zOs_2Al_{10}$.

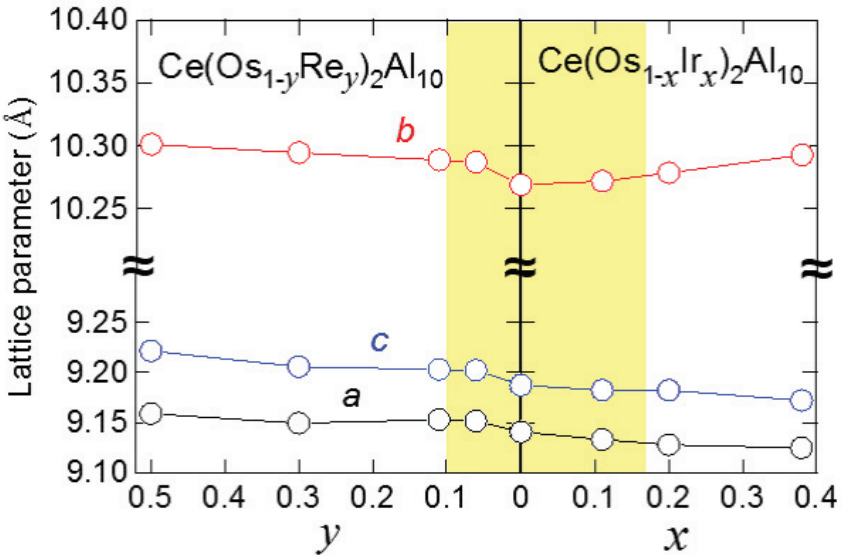

Figure 2.7: Orthorhombic lattice parameters of polycrystalline samples of $Ce(Os_{1-y}Re_y)_2Al_{10}$ and $Ce(Os_{1-x}Ir_x)_2Al_{10}$.

2.2.2 Electron-probe microanalysis

Electron-probe micro analysis (EPMA) is the most commonly method of non-destructive elemental analysis. The electron beam of < 0.1 μm in diameter is focused on the sample, producing the inelastic collisions between incident-electrons and the electrons in the inner-shells of atoms in the sample. The inner-shell electrons are left from its orbit due to the collisions, a higher-shell electron falls into the vacancy. The process generates the characteristic x-rays at particular wavelengths. Their x-ray intensities reflect the concentration of atoms in the sample. Therefore, we can determine the atomic compositions of the samples. The high spatial resolution probe can detect almost all elements except for light elements (H, He, and Li) because each element has the specific set of x-rays. We have two ways to detect the characteristic x-rays. One is energy-dispersive spectrometry (EDS) and the other is wavelength-dispersive spectrometry (WDS). The EDS system uses a solid-state semiconducting detector, which collects and counts all of the emitted x-rays at once. On the other hand, the WDS system detects x-rays of specific energy by utilizing Bragg diffraction from diffracting crystals. By changing the angle of incident characteristic x-rays, the crystals will constructively diffract x-rays of specific wavelengths. EDS system yields more information and require a much shorter counting time, whereas the energy resolution is not better than 100 eV. In our study, EPMA was performed by WDS system with the high energy resolution of 10 eV.

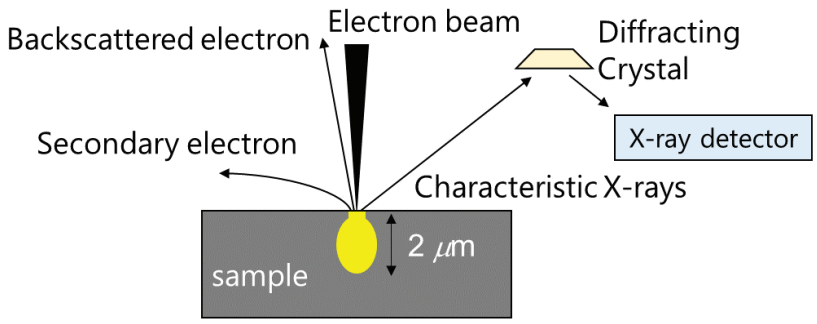

Figure 2.8: Measurement process of electron-probe micro analyzer (EPMA, WDS system). When focused electron beam at typical energy 5–30 eV hits a sample, characteristic x-rays, secondary electrons, and backscattered electrons are emitted from the sample. The characteristic x-rays are diffracted through the diffracting crystal to be monotonized.

CeT_2Al$_{10}$ (T = Fe, Ru, and Os)

Figure 2.9 shows the examples of photographs for the polished single crystals of CeT_2Al$_{10}$(T = Fe, Ru, and Os). We obtained large single crystals for T = Fe (10 × 8 × 5 mm^3) compared with T = Ru and Os (3 × 3 × 2 mm^3).

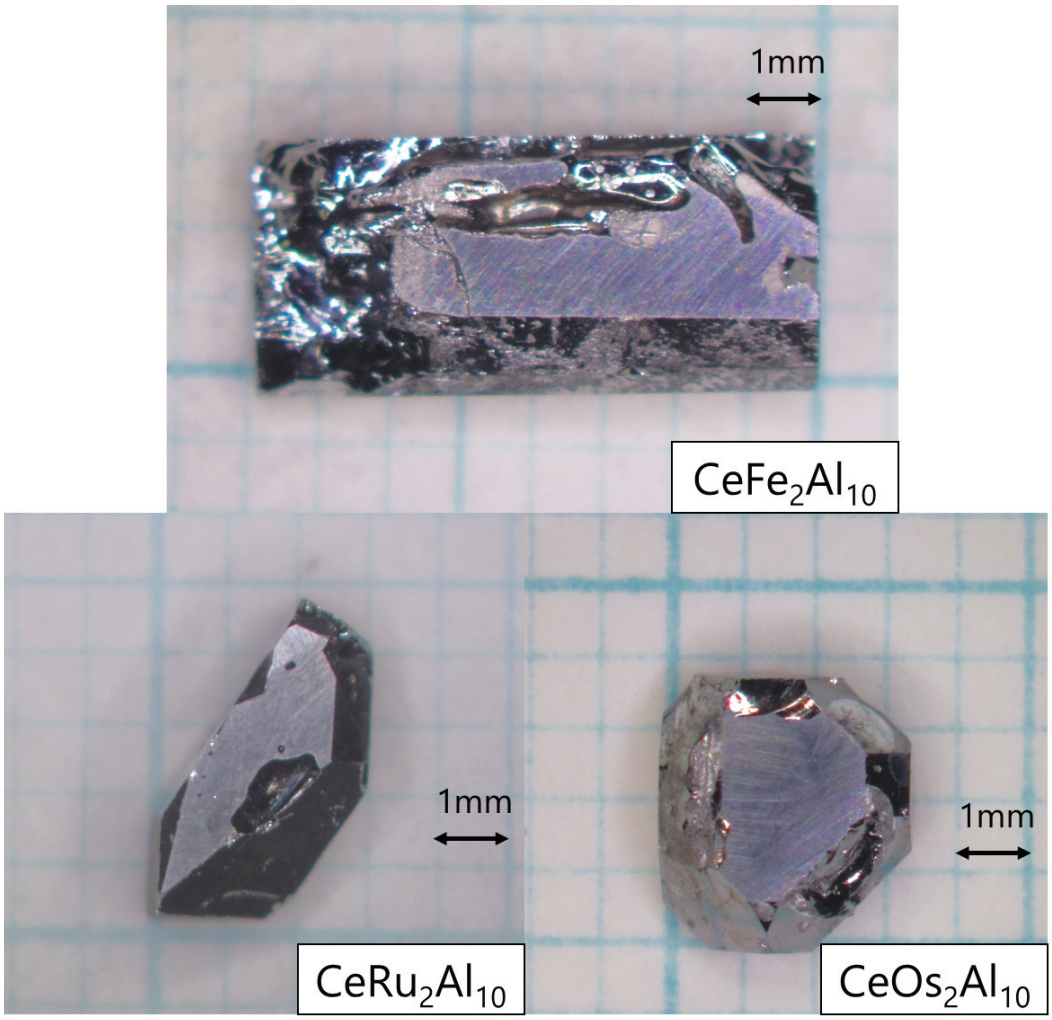

Figure 2.9: Photographs of the single crystals of CeT_2Al$_{10}$ (T = Fe, Ru, and Os).

$\mathbf{Ce_{1-z}La_zOs_2Al_{10}}$

Several crystals of $Ce_{1-z}La_zOs_2Al_{10}$ of approximately $2 \times 2 \times 1$ mm^3 were obtained. Figures 2.10 and 2.11 are, respectively, the photograph and the BSE images for the single crystals grown from the the initial compositions $Ce_{1-Z}La_ZOs_2Al_{10}$. The atomic compositions determined by EPMA are listed in Table 2.2. The gray areas of the images are the CeT_2Al_{10} phase, while the white areas are the impurities of $OsAl_4$. The compositions of La (z) in the crystals were found to deviate slightly from the initial ones (Z). For $Z =$ 0.05, 0.10, 0.20, 0.30 and 0.5, the actual values of z were 0.043, 0.096, 0.15, 0.24 and 0.51, respectively. Here, the sum of composition of Ce and La was assumed to be 1.0.

Table 2.2: Compositions for the single crystals made from $Ce_{1-Z}La_ZOs_2Al_{10}$ with the initial compositions $Z = 0.05$, 0.1, 0.2, 0.3, and 0.5.

Z	Ce	La	Os	Al
0.05	0.957	0.043	1.92	10.08
0.1	0.91	0.09	1.95	10.19
0.20	0.86	0.14	1.93	10.22
0.30	0.76	0.24	1.92	10.29
0.5	0.51	0.49	1.97	10.25
1	0	1	1.92	10.34

$\mathbf{Ce(Os_{1-y}Re_y)_2Al_{10}}$

Several crystals of $Ce(Os_{1-y}Re_y)_2Al_{10}$ of approximately $4 \times 3 \times 2.5$ mm^3 were obtained. The photographs and BSE images are shown in Figs. 2.12 and 2.13, respectively. The BSE images are monocolor, indicating the absence of impurity phases. Therefore, the contents of y were the same as the initial ones $Y = 0.01$, 0.02, 0.03, 0.05, and 0.1 (see Table 2.3).

Table 2.3: The compositions for the single crystals made from $Ce(Os_{1-Y}Re_Y)_2Al_{10}$ with the initial compositions $Y = 0.01$, 0.02, 0.03, 0.05, and 0.1.

Y	Ce	Os	Re	Al
0.01	1	1.93	0.02	10.10
0.02	1	1.92	0.04	10.18
0.03	1	1.87	0.05	10.07
0.05	1	1.84	0.10	10.13
0.1	1	1.75	0.19	10.15

$\mathbf{Ce(Os_{1-x}Ir_x)_2Al_{10}}$

Figures 2.14 and 2.15, respectively, show the photographs and BSE images for $Ce(Os_{1-x}Ir_x)_2Al_{10}$. The compositions of Ir (x) were found to be 0, 0.03, 0.04, 0.08, 0.15, 0.27 for the initial ones $X = 0$, 0.02, 0.03, 0.10, 0.20, and 0.30 respectively. The difference between the values x and X is attributed to the segregation of a small amount of impurity phase of $(Os,Ir)Al_4$. The impurity phases are the white areas in Fig. 2.15 .

Table 2.4: The compositions for the single crystals made from $Ce(Os_{1-X}Ir_X)_2Al_{10}$ with the initial compositions $X = 0.01$, 0.03, 0.05, 0.2, and 0.3.

X	Ce	Os	Ir	Al
0.01	1	1.92	0.029	10.16
0.03	1	1.87	0.06	10.05
0.05	1	1.86	0.080	10.01
0.2	1	1.64	0.30	10.17
0.3	1	1.42	0.55	10.18

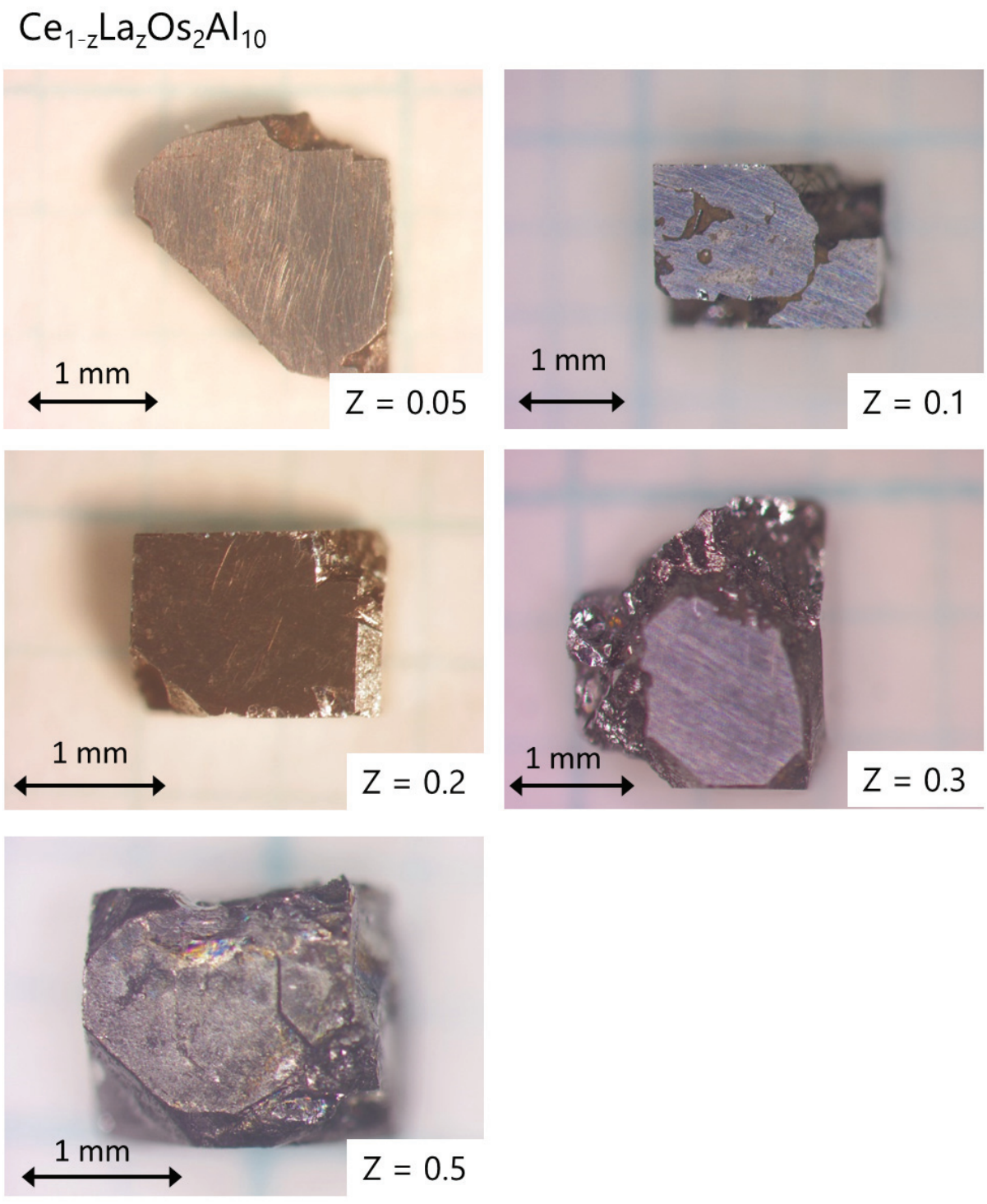

Figure 2.10: Photographs of the single crystals made from the initial compositions $Ce_{1-Z}La_ZOs_2Al_{10}$ with $Z = 0.05$, 0.1, 0.2, 0.3, and 0.5.

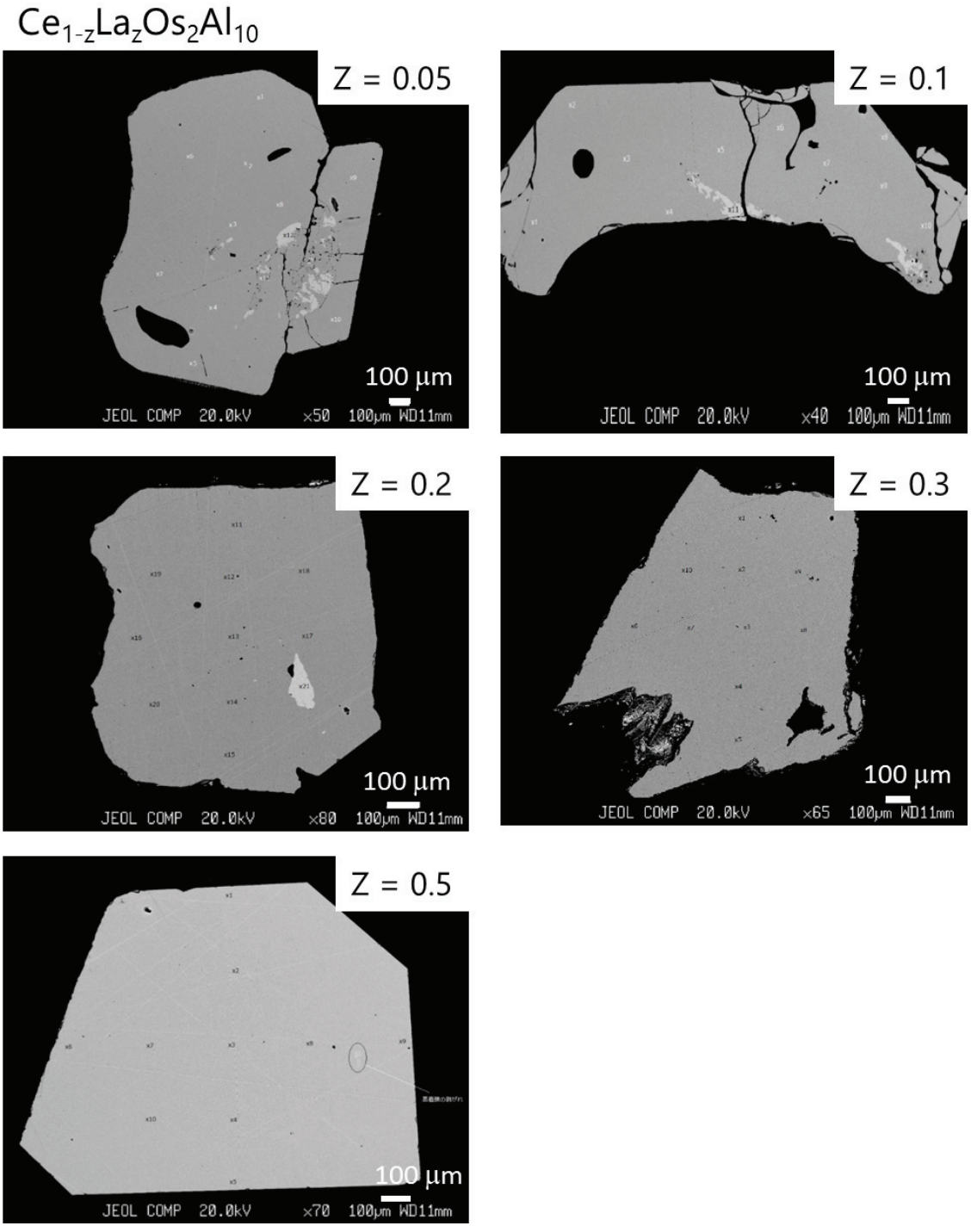

Figure 2.11: Back scattered electron images for the polished crystals $Ce_{1-Z}La_ZOs_2Al_{10}$ made from the initial compositions $Z = 0.05$, 0.1, 0.2, 0.3, 0.5. Note the 100 μm scale given at the right bottom.

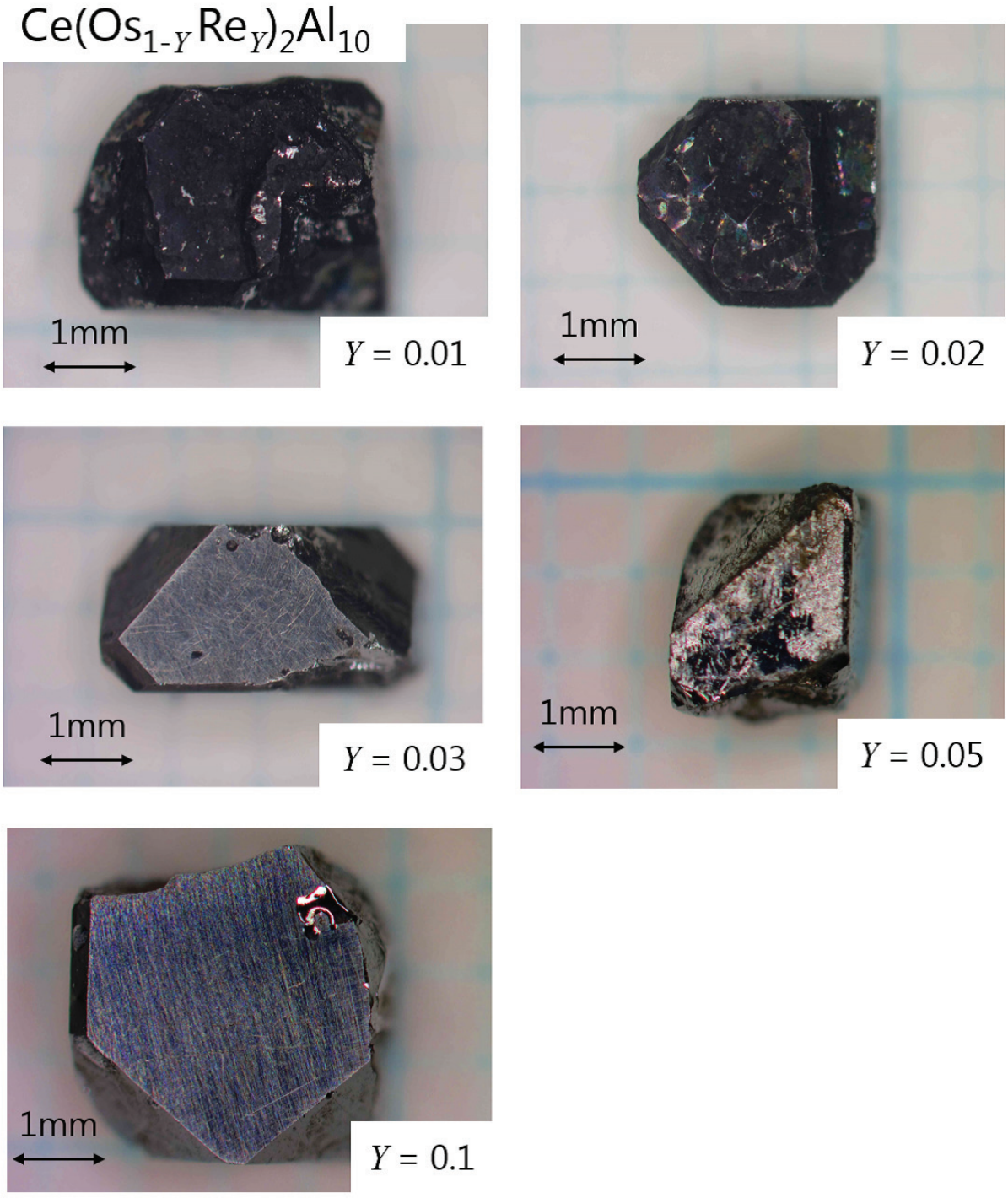

Figure 2.12: Photographs of single crystals made from the initial compositions $Ce(Os_{1-Y}Re_Y)_2Al_{10}$ with $Y = 0.01$, 0.02, 0.03, 0.05, and 0.1.

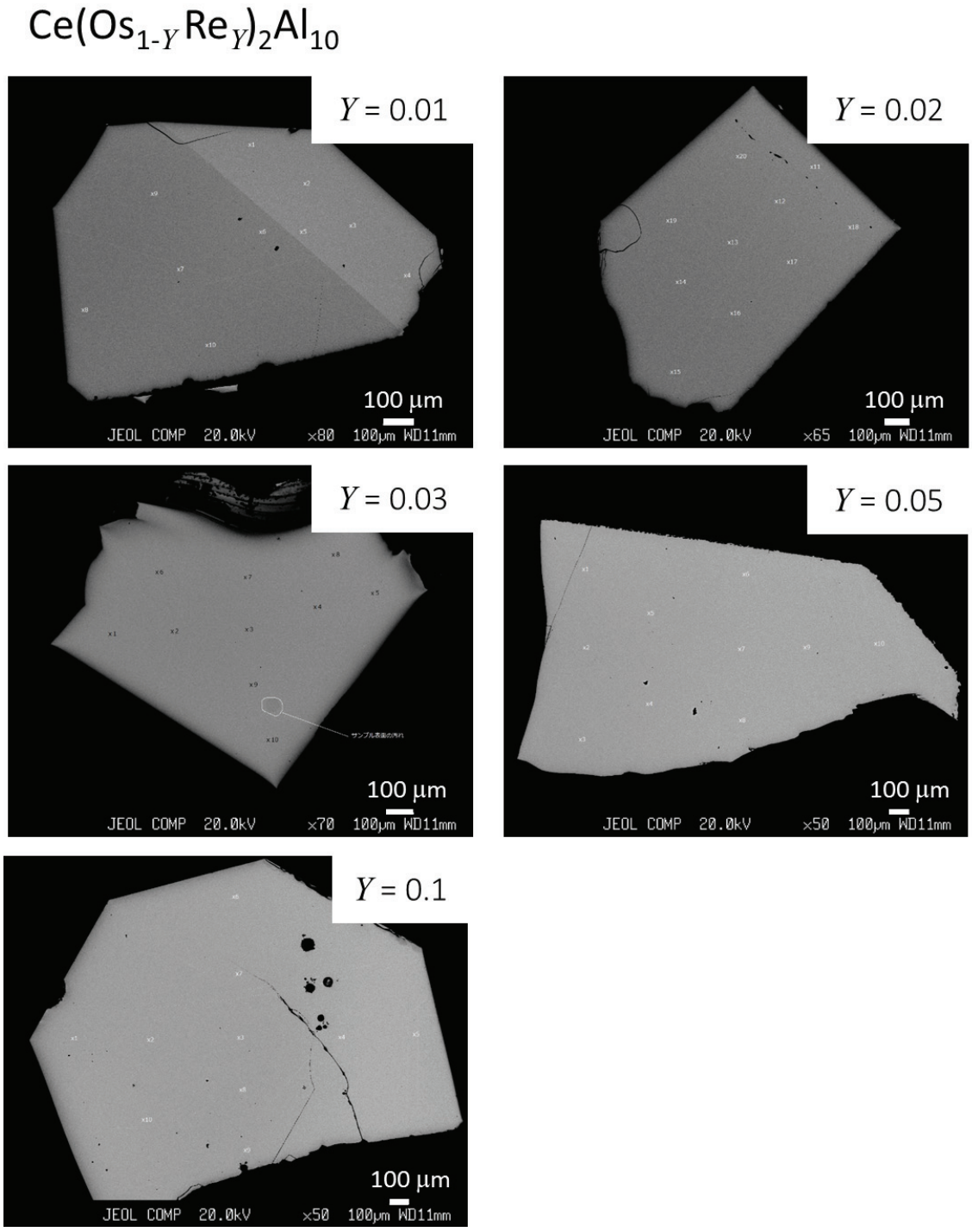

Figure 2.13: Back scattered electron images for the polished crystals $Ce(Os_{1-Y}Re_Y)_2Al_{10}$ made from the initial compositions $Y = 0.01$, 0.02, 0.03, 0.05, and 0.1.

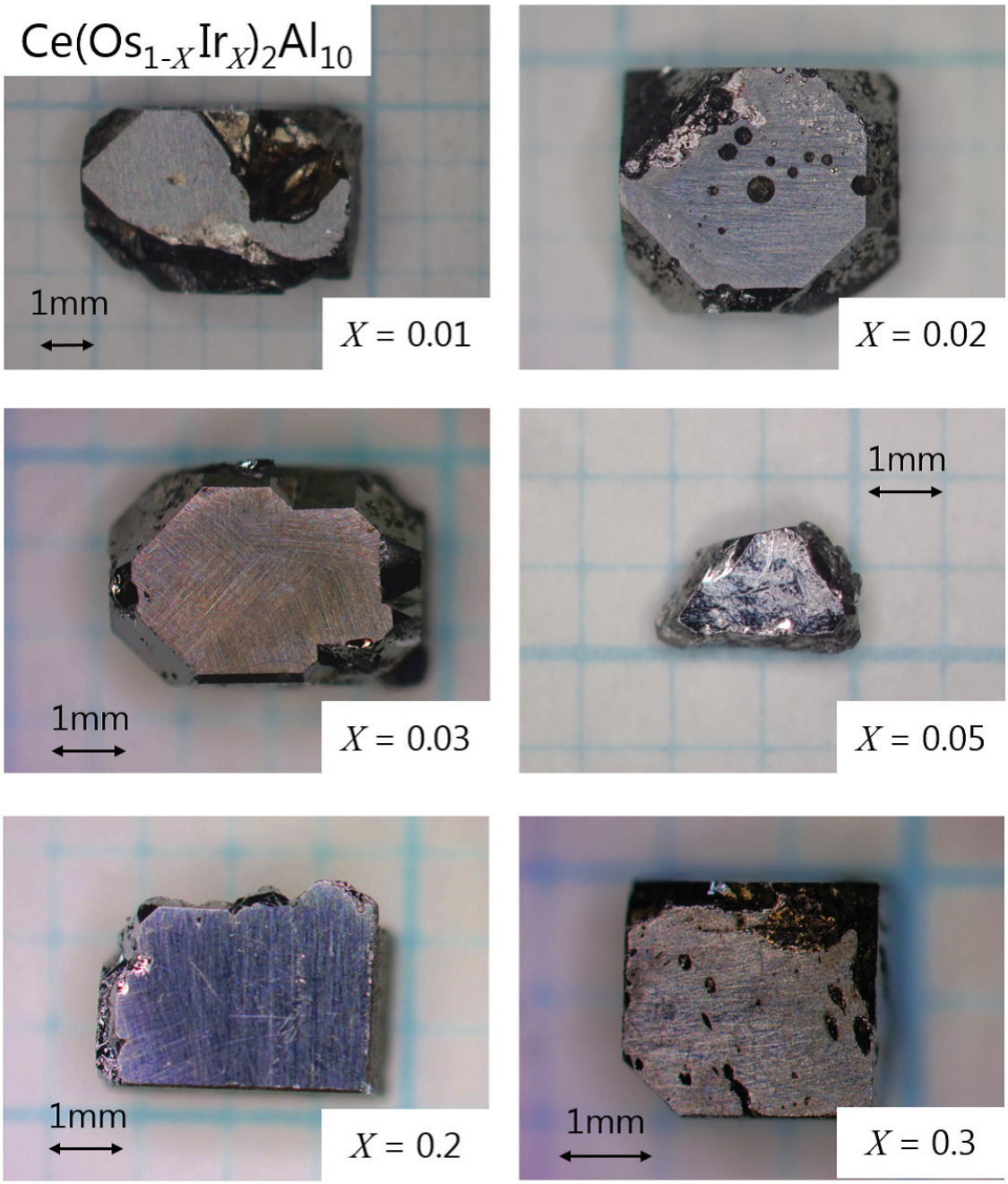

Figure 2.14: Photographs of the single crystals made from the initial compositions $Ce(Os_{1-X}Ir_X)_2Al_{10}$ with $X = 0$, 0.01, 0.02, 0.05, 0.2, and 0.3.

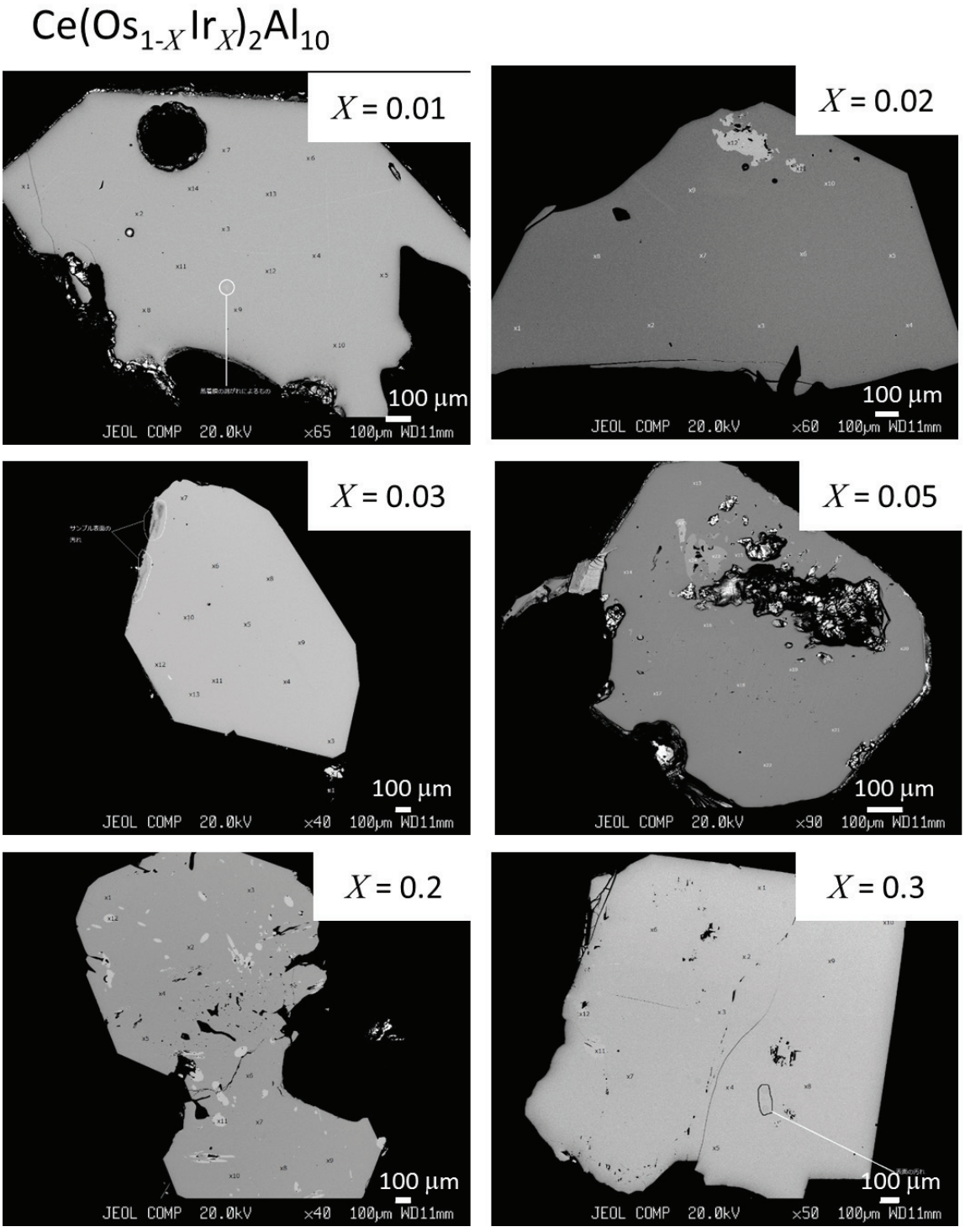

Figure 2.15: Back scattered electron images for the polished crystals $Ce(Os_{1-X}Ir_X)_2Al_{10}$ made from the initial compositions $X = 0$, 0.01, 0.02, 0.05, 0.2, and 0.3.

2.2.3 Orienting crystal direction

Figure 2.16 shows the x-ray diffraction patterns for single crystals of $CeOs_2Al_{10}$ taken for the polished planes perpendicular to (a) a- (b) b-, and (c) c-axes, respectively. The Laue photos taken for these planes are shown in Fig. 2.17, which are in accord with simulated patterns in the Fig. 2.18. In all cases, single crystalline nature was checked by taking several Laue photos and x-ray diffraction patterns for different areas. When the photographs and diffraction pattern showed well-defined reflection patterns with sharp spots, the crystals were cut by using a spark erosion machine in appropriate shapes for the measurements of magnetic, transport, and tunneling properties.

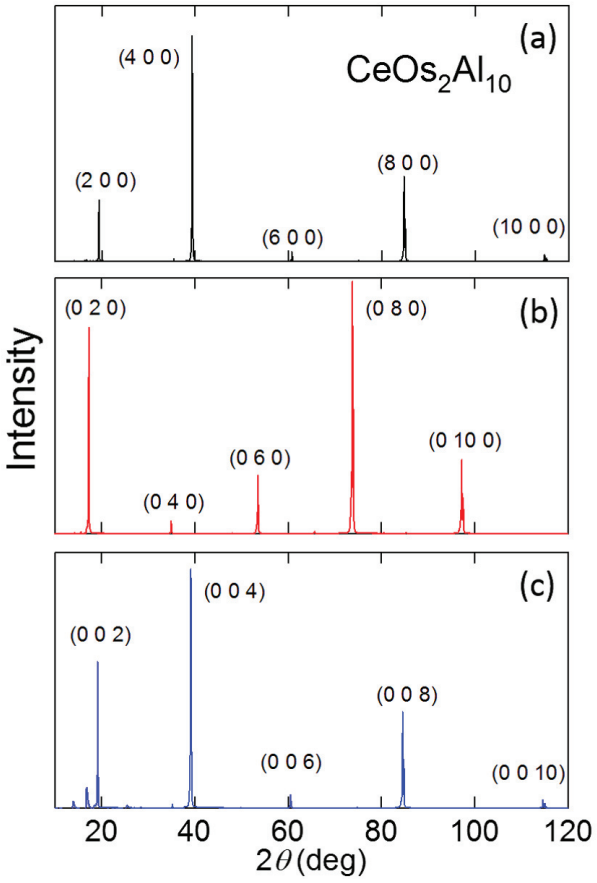

Figure 2.16: X-ray diffraction patterns of the single crystal of $CeOs_2Al_{10}$ taken for the polished planes perpendicular to (a) a- (b) b-, and (c) c- axes, respectively.

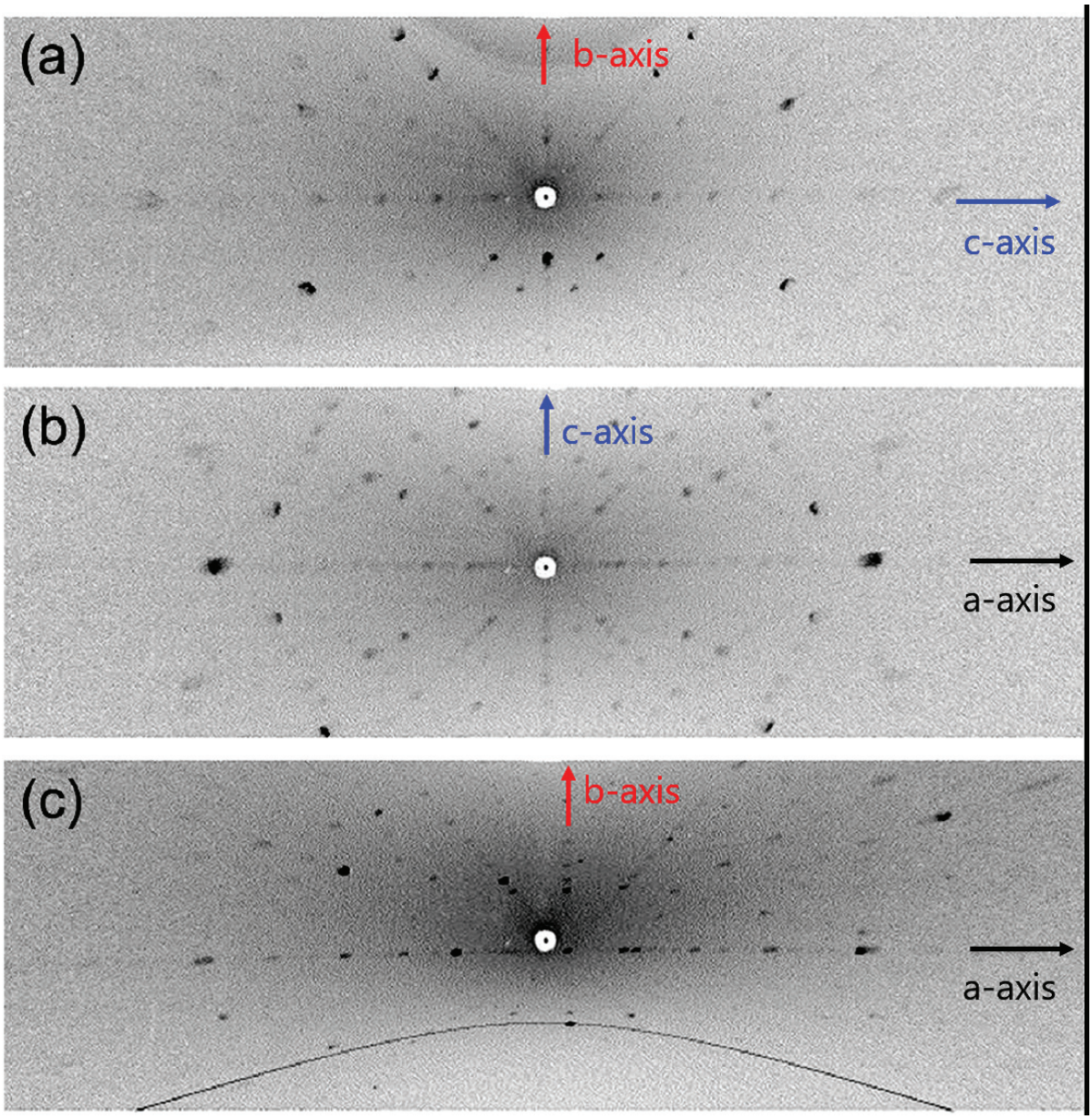

Figure 2.17: X-ray Laue pictures of a $CeOs_2Al_{10}$ single crystal oriented in the (a) (1 0 0), (b) (0 1 0), and (c) (0 0 1) directions, respectively

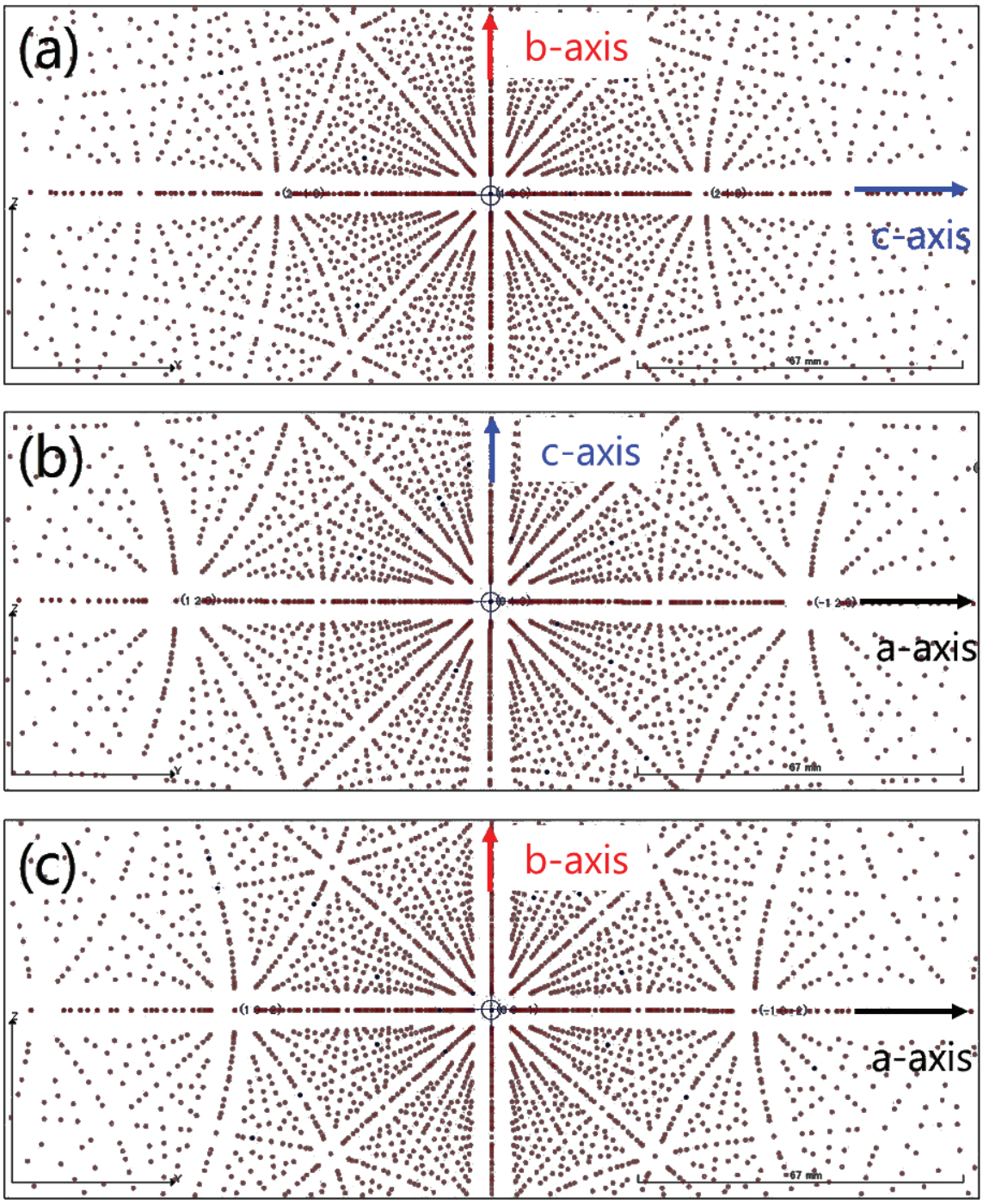

Figure 2.18: X-ray Laue patterns simulated for $CeOs_2Al_{10}$ oriented in the (1 0 0), (0 1 0), and (0 0 1) directions, respectively.

Chapter 3

Experimental

3.1 Magnetization

The temperature dependence of magnetization $M(T)$ was measured in an external field $B = 1$ T from 1.8 to 300 K with a commercial Magnetic Property Measurements System (MPMS, Quantum Design) which is shown in Fig. 3.1. Thereby, the superconducting quantum interference device (SQUID) was used to detect the magnetic signal. The sample was moved upward through the pickup coils, inducing the SQUID output voltage, as shown in Fig. 3.2. The integration of the output voltages versus position is proportional to the magnitude of the magnetic moment. The absolute value was calibrated by using a standard sample of Pd.

The isothermal magnetization $M(B)$ was measured up to $B = 14$ T at differential temperatures by the option of the DC extraction method of the Physical Property Measurement System (PPMS) in Fig. 3.3. A set of copper coils produces the voltage signal by the movement of the magnetic sample. The amplitude of the detection coil signal depends upon both the extraction speed and the samples's magnetic moment. The servo motor transports the sample through the whole detection coil set at a speed of 100 cm/sec. The short scan time allows the average of several scans for each measurement, reducing the contribution of random error. During one transportation, PPMS reads the voltage profile curve as shown in Fig. 3.4. The sample moment is obtained by integrating the voltage profile and fitting the waveform. The resolution of magnetic moment is 2.5×10^{-5} emu being two orders of magnitude less sensitive than that of MPMS $\sim 1 \times 10^{-7}$

emu. However, this resolution is enough to measure $M(B)$ up to 14 T for our samples.

For magnetization measurements, we used a sample of a rectangular shape with the typical mass of 30–100 mg. First, we cut off a small section of a transparent plastic straw and place the sample at the center of the straw of 10.4 mm in inner diameter. Then, the straw was mounted in a full-sized straw as shown in Fig. 3.5. It is necessary to ensure that the sample does not budge inside the straw to avoid any movement during the transportation at the high speed.

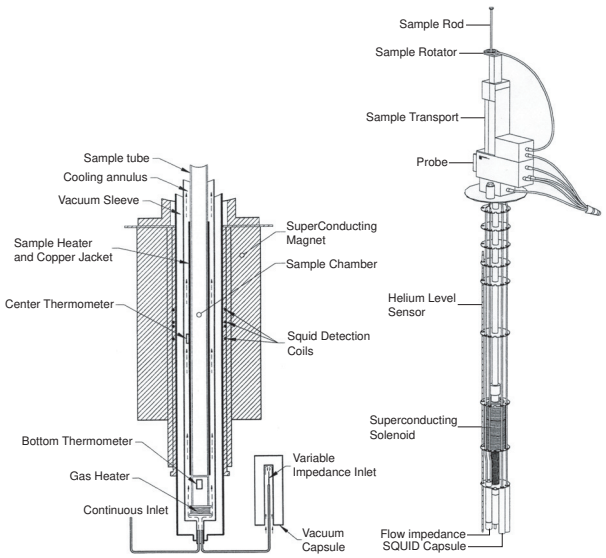

Figure 3.1: SQUID magnetometer of MPMS (Quantum Design) [116]

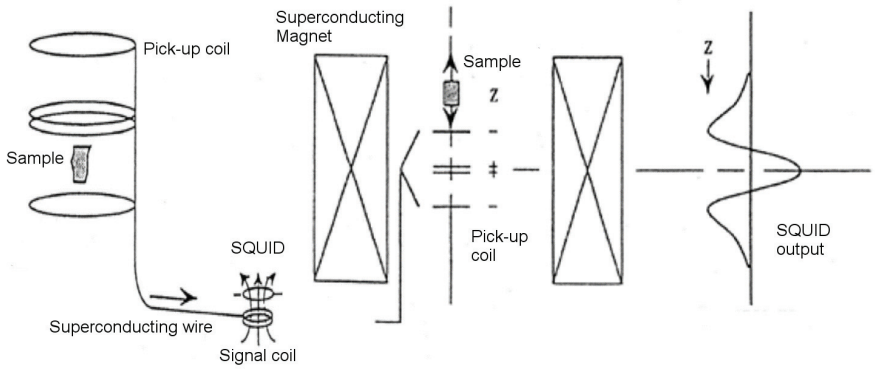

Figure 3.2: Principle of the measurement of magnetic moments by the SQUID system of MPMS (Quantum Design) [116]. External field was applied up to 5 T.

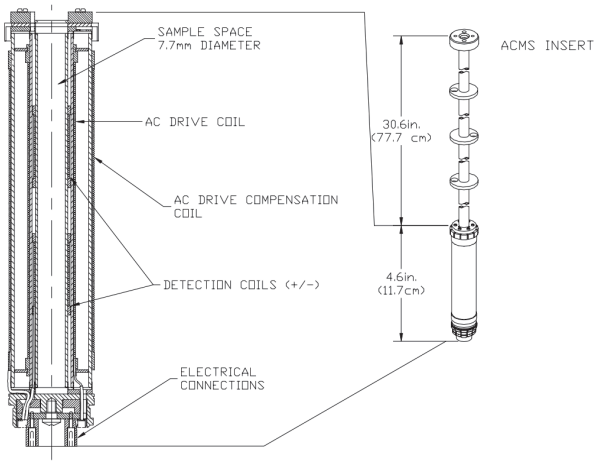

Figure 3.3: A coil set to measure magnetization by the extraction method using the PPMS [117]. External field was applied up to 14 T.

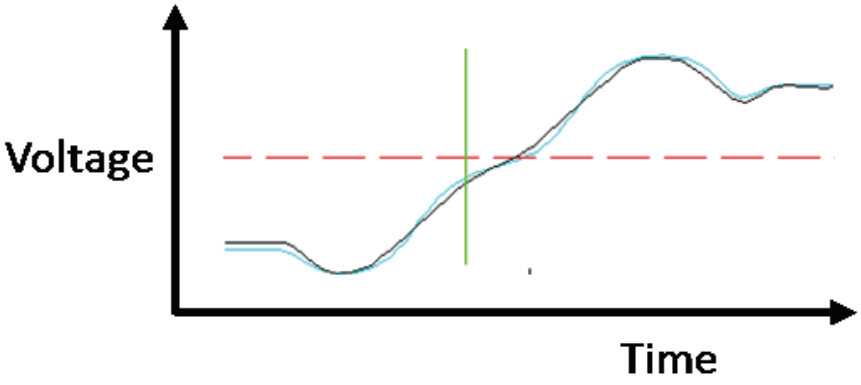

Figure 3.4: Voltage wave form as a function of time for the DC measurement with PPMS (black line). The light blue line is the waveform reference and indicates ideal measurement results [117].

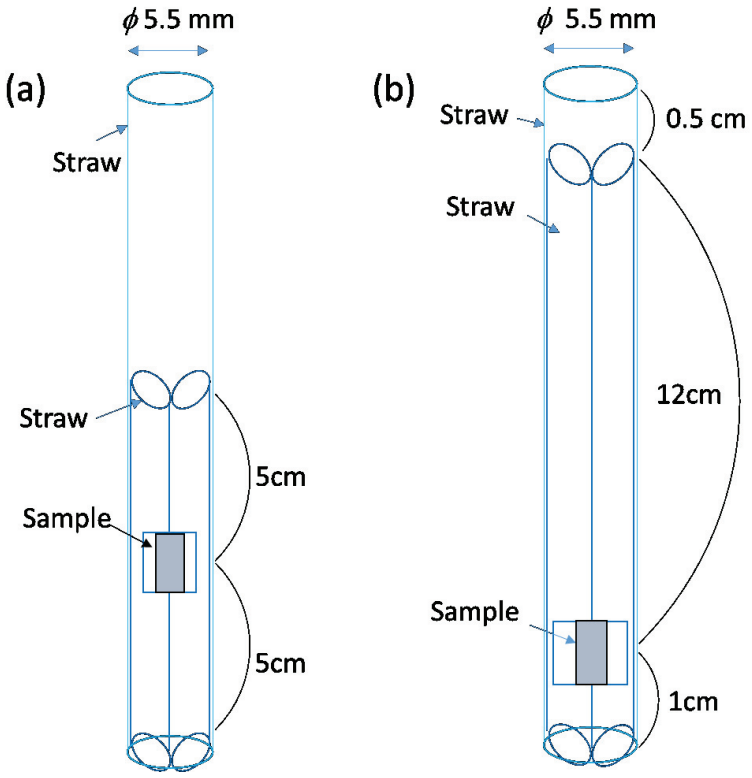

Figure 3.5: Sample mounting in the straw for the magnetization measurements with (a) the SQUID systems of MPMS and (b) the DC extraction option of PPMS.

3.2 Specific heat

The specific heat C at constant pressure was measured from 2 to 300 K by a relaxation method using a calorimeter in PPMS. Figure 3.6 shows the sample platform made of sapphire in the heat capacity option. Au-35% Pd alloy wires of 50 μm in diameter provide the required thermal connection to the platform. A sample of $\sim$ 10 mg was mounted on the platform. The sample was thermally connected to the addenda with Apiezone N-grease. However, too much of grease leads to poor thermal diffusivity, which results in an inaccurate sample heat capacity. The PPMS controls the heat supplied to and released from a sample while monitoring the resulting change in temperature T. The amount of heat $P(t)$ is equal to P_0 during the heating portion of the measurement and equal to zero during the cooling portion. Based on the temperature response in the cooling period, the relaxation time τ is calculated. The PPMS fits the entire response of the sample platform to a model that accounts for both the thermal relaxation of the sample platform to the bath temperature and that of the sample platform to sample itself. The τ leads to heat capacity at constant pressure C by using the equations as described below.

$$\tau = \frac{C}{K} = \frac{C_{\mathrm{s}} + C_{\mathrm{h}}}{K_{\mathrm{w}}} \ , \tag{3.1}$$

$$K_{\mathrm{w}} = \frac{P}{\Delta T} \ , \tag{3.2}$$

$$C = K_w \tau = \frac{P\tau}{\Delta T} \ , \tag{3.3}$$

$$C_{\mathrm{s}} = \frac{P\tau}{\Delta T} - C_{\mathrm{h}}. \tag{3.4}$$

The C_{h} and C_{s}, respectively, are the heat capacities of the holder and sample, and K_{w} is the thermal conductance of the wire.

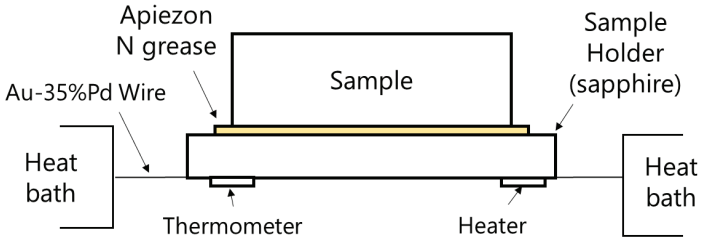

Figure 3.6: Thermal connections between the sample, the holder, and the heat bath in the PPMS heat capacity option [118].

Simple Model

The simple model, which is the most basic analysis, assumes the sample and sample platform are in good thermal contact with each other [118]. The equations of simple model are expressed as

$$C_{\text{total}}(T) = \frac{dQ(T)}{dT} \tag{3.5}$$

$$C_{\text{total}}(T)\frac{dT}{dt} = P(t) - \int_{T}^{T_0} K_w(T')dT' \tag{3.6}$$

$$C_{\text{total}}(T)\frac{dT}{dt} = P(t) - K_w(T - T_0) \ , \tag{3.7}$$

where C_{total} is the total heat capacity of the sample and sample platform, and T_0 is the temperature of the thermal bath.

Two-tau Model

The two-tau model is used to measure the heat capacity of the sample when poor thermal attachment of the sample to the platform produces a temperature difference between the two [118]. This model simulates the effect of heat flowing between the platform and puck. The following equations express the two-tau model. The respective temperatures of the platform and sample are given by $T_{\text{P}}(t)$ and $T_{\text{s}}(t)$, respectively:

$$P(t) = \int_{T_0}^{T_h(t)} K_w(T')dT' + \int_{T_s(t)}^{T_h(t)} K_g(T')dT' + C_h(T)\frac{dT_h(t)}{dt} \tag{3.8}$$

$$C_h(T)\frac{dT_h(t)}{dt} = P(t) - K_w(T_h(t) - T_0) - K_g(T_h(t) - T_s(t)). \tag{3.9}$$

The sample heat capacity can be obtained, as derived from the Eqs. (3.7) and (3.9):

$$C_s(T)\frac{dT_s(t)}{dt} = K_g\{T_h(t) - T_s(t)\}. \tag{3.10}$$

3.3 Electrical resistivity

The electrical resistivity ρ was measured from 2.6 to 300 K by a standard AC four-probe method with Lake shore 370 AC Resistance Bridge operating at 13.7 Hz. The AC method removes the thermoelectric contribution. The setting of the sample and leads is shown in Fig. 3.7. The sample was cut into the typical dimensions of 0.5 × 0.5 × 2 mm^3 using a spark erosion machine. We used Au wires of 50 μm in diameter (Tanaka Kikinzoku, ϕ50 μm, 99%) as for pairs of current and voltage leads. The Au wires were connected on the samples by the Ag paste (Tokuriki Honten P-248). Thereby, the contact resistance was kept less than 10 Ω. The sample was glued by using a varnish (GE7031) to a Cu plate covered with a cigarette paper for electrical insulation. The Cu plate was mounted on a cold head of a Gifford-McMahon-type refrigerator (IWATANI CORP., UW404-HO).

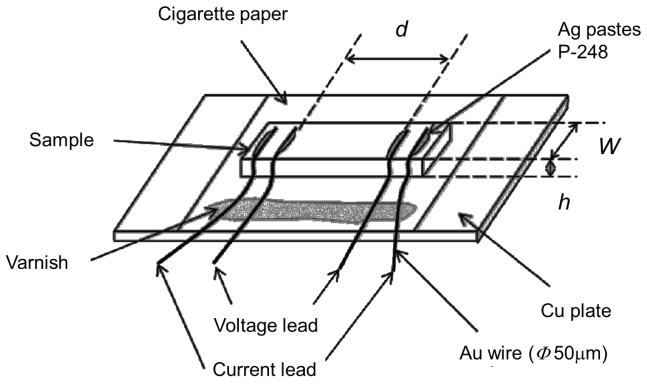

Figure 3.7: The setting of the sample and leads for the electrical resistivity measurement by the AC four-probe method.

3.4 Thermopower

The thermopower S is the thermoelectric voltage induced by the temperature difference between two points of a sample when no electric current is passing through the sample. The S is experimentally defined as

$$S = \lim_{\Delta T \to \infty} \frac{\Delta V}{\Delta T} \ , \tag{3.11}$$

where ΔT and ΔV denote the temperature and voltage differences between the two points of the sample, respectively.

Mott formula

The diffusion term of thermopower of a metal is expressed by the Mott formula as describe below:

$$S_d = -\frac{\pi^2}{3} \frac{k_B^2 T}{|e|} \Big[\frac{\partial \ln \sigma}{\partial E} \Big]_{E=\eta} \ , \tag{3.12}$$

where σ is the dc conductivity and η is the chemical potential. It is derived from the linear response theory of the transport phenomena [119]. In addition to the diffusion term, there is the phonon drag contribution $S_p(T)$. At low temperatures, $S(T)$ in certain metals displays nonliner temperature dependence when S_p exceeds S_d.

Thermopower of Ce-based compounds

The thermopower of Ce-based valence fluctuating compounds such as CeNi [57, 58] displays a large and broad peak at around $T_{\rm K}$ as shown in Fig. 1.25 (b). The absolute value is 10 – 100 times larger than in simple metals. It is caused by the scattering of conduction electrons from $4f$ electron states in the vicinity of the chemical potential. The large and positive $S(T)$ is understood in terms of the Mott formula for the diffusion term. From the Boltzmann equation, the conductivity σ is expressed by

$$\sigma = \frac{e^2}{12\pi^3 \hbar} \int \tau v dS_{\rm F} \ , \tag{3.13}$$

where τ and v, respectively, are scattering relaxation time and the velocity of conduction electrons, and $S_{\rm F}$ is the Fermi surface area. If we adopt a free electron model, the σ is given by $\sigma = \frac{e^2 \tau}{m^*} N$, where N is the density of electrons with the mass m^*. The S_d in Ce

compounds is derived from a two-band model in which carriers are conduction electrons and $4f$ electrons.

$$S_d = \frac{\sigma_c S_d^c + \sigma_f S_d^f}{\sigma_c + \sigma_f}, \tag{3.14}$$

where S_d^c, S_d^f, σ_c, σ_f, respectively, are the thermopower and conductivity for conduction electrons "c" and $4f$ electrons "f". These terms are expressed by the Mott formula as

$$S_d^c \propto (d \ln \sigma_c / dE)_{E=\eta} \tag{3.15}$$

$$S_d^{4f} \propto (d \ln \sigma_f / dE)_{E=\eta} \ . \tag{3.16}$$

Here, σ_c and σ_f are determined by the scattering between conduction electrons and $4f$ electrons whose density of state are N_c and N_f, respectively.

$$\sigma_c \propto N_c(E) \tau_{c-f} \tag{3.17}$$

$$\sigma_f \propto N_f(E) \tau_{f-f}. \tag{3.18}$$

Both τ_{c-f} and τ_{f-f} are inversely proportional to $N_f(E)$. Therefore, σ_f does not depend on $N_f(E)$, and we can express $\ln \sigma$ as describe below.

$$\ln \sigma \propto \ln N_c(E) - \ln N_f(E). \tag{3.19}$$

Because of the relation $[d \ln N_c(E_{\rm F})/dE] \ll [d \ln N_f(E_{\rm F})/dE]$,

$$d \ln \sigma_c / dE \propto -d \ln N_f / dE. \tag{3.20}$$

This term is not included in S_d^f so that the total S_d is dominated by S_d^c. Eventually, the Mott Formula is expressed by

$$S_d(T) \sim S_d^c(T) \sim \frac{\pi^2 k^2 T}{3|e|} \Big[\frac{d \ln N_f(E)}{dE} \Big]_{E=\eta} \sim \frac{\pi^2 k^2 T}{3|e|} \Big[\frac{1}{N_f} \frac{\partial N_f}{\partial E} \Big]_{E=\eta}. \tag{3.21}$$

Since the quasiparticle density of states $N_f(E)$ in valence fluctuating Ce compounds has an extremely large positive slope of $\partial N_f / \partial E$ at $E = \eta$, $S(T)$ exhibits a large positive peak. Such a peak is found for CeNi as shown in Fig. 1.25. Furthermore, the Kondo effect, crystal electric field, and spin interactions strongly affect the quasiparticle band and the degeneracy of the $4f$ states. Then, $S(T)$ changes drastically at the characteristic

temperatures by these effects. As an example, $S(T)$ for a localized $4f$ electron compound CePtSn [29, 60] with $T_{\rm N} = 7$ K is presented in Fig. 1.25 (b).

In the case of the phase transition in concomitant with a topological change of the Fermi surface, Eq. (3.20) is not applicable. Instead, $S_i(T)$ is expressed from Eq. (3.13) as

$$S_i(T) \propto \Big[\frac{\partial \ln \tau_i}{\partial E} + \frac{\partial \ln \int v_i dS_F}{\partial E}\Big]_{E=\eta}, \tag{3.22}$$

where v_i is the velocity of a conduction electron along the i direction. An evident anomaly appears in $S(T)$ when the Fermi surface is reconstructed as a function of temperature or external field [120].

Seesaw heating method

A seesaw heating method is used to measure $S(T)$ [121]. The sample stage as illustrated in Fig. 3.8 was mounted on a cold head of a Gifford-Mcmahon-type refrigerator (IWATANI CORP., CW404). The parts A are strain gauges of 120 Ω (type KFL-02-0120-C1-16, Lot Y009, batch 061A H10, KYOWA) used as heaters, to which electrical current is supplied by the current source ADVANTEST R6144. The parts B are a pair of Cernox thermometers (Model: CX-1050-SD-HT, serial No. 73213, 73162, Lakeshore). The strain gauges are glued on the Cernox sensors by GE7301 varnish to make thermal contact. The voltage of the Cernox sensors is measured by the temperature controller (Lakeshore 331). The fiber reinforced plastics (FRP) plate of 0.5 mm thickness was placed to weaken the thermal contact between thermometers and the sample stage. The FRP plate was glued on sample stage made of Cu by using GE7301 varnish. This setting up makes it easy to adjust the distance between two thermometers in the range 2 – 7 mm, depending on the length of the sample. The wires denoted by D are voltage leads. All wires are thermally anchored to the heat sink rods. The sample (E) was spanned between the two thermometers by using a Ag paste (TOKURIKI HONTEN P-248). The thermoelectric voltage V is measured by a Keithly 2182 nanovoltmeter. Figure 3.9 displays the V and the temperature of two Cernox thermometers as a function of time. In this method, $S(T)$ and the averaged temperature $T_{\rm av}$ of the sample are given by the following equations.

$$S(T) = \frac{2\Delta V}{\Delta T_1 + \Delta T_2} \tag{3.23}$$

$$\Delta T_1 + \Delta T_2 = (T_{1f} - T_{1i}) + (T_{2i} - T_{2f}) \tag{3.24}$$

$$2\Delta = V_f - V_i \tag{3.25}$$

$$T_{\rm av} = \frac{T_{2f} + T_{2i} + T_{1f} + T_{1i}}{4}. \tag{3.26}$$

The time dependences of parameters T_{2f},T_{1f}, T_{1i}, T_{2i}, V_f, and V_i are indicated in Fig. 3.9. The temperature difference at a few percent of the absolute temperature was generated by the strain gauges. Because of the definition of ΔV, other thermopower between the sample, wires, and the Ag paste can be cancelled.

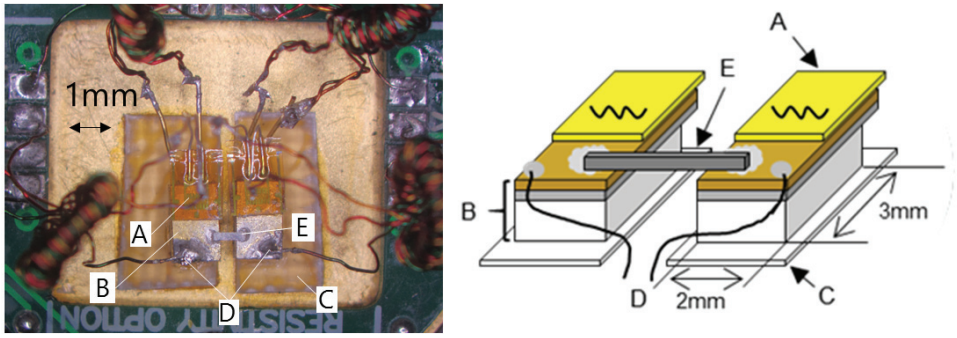

Figure 3.8: The setting of the thermopower measurement by the seesaw heating method.

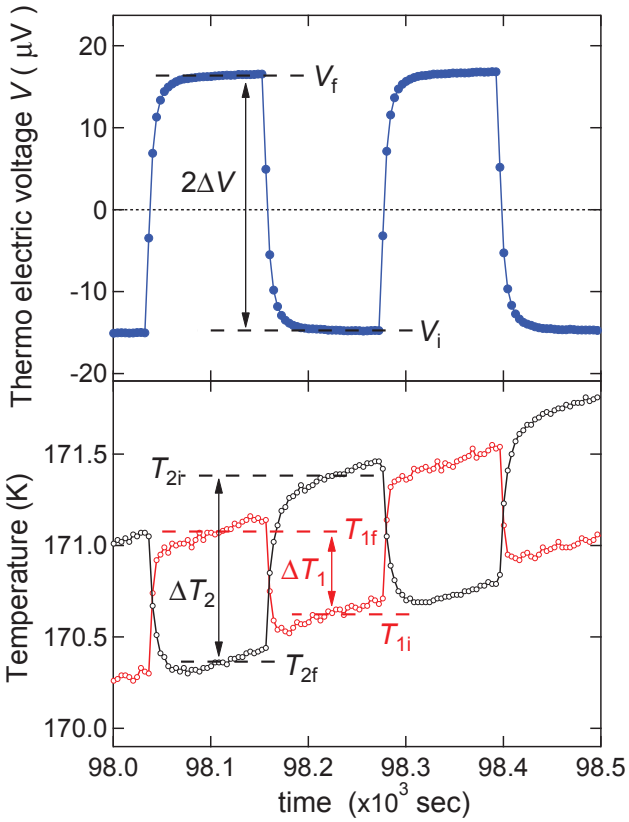

Figure 3.9: Time variations of temperatures T_1 and T_2 of a pair of Cernox thermometers and thermal electrical voltage V for the thermopower measurement by the seesaw heating method.

3.5 Tunneling spectroscopy

3.5.1 Tunneling process of electrons in solids

The tunneling spectroscopy has been used as a powerful method to probe opening of energy gaps in the vicinity of the Fermi level $E_{\rm F}$ in superconductors and Kondo semiconductors [46, 47, 48, 61, 129]. The method is based on the concept of quantum tunneling of electrons in solids [122]. Figure 3.13 displays the wave function ψ as a function of x (the thickness of barrier) in a metal-insulator-metal junction. The basis for the tunneling current is the inherently smooth behavior of the probability density at points of finite discontinuity in the potential energy $U(x)$. At a metal-insulator interface, the wave function $\psi(x)$ for an electron in the Metal 1 at $E_{\rm F}$ does not vanish outside the metal. Therefore, application of a bias voltage V allows the electrons to tunnel when the thickness of the barrier x is small enough ($x < \sim$100 Å). We measure the tunneling current I in the junction as a function of V, ie, dI/dV.

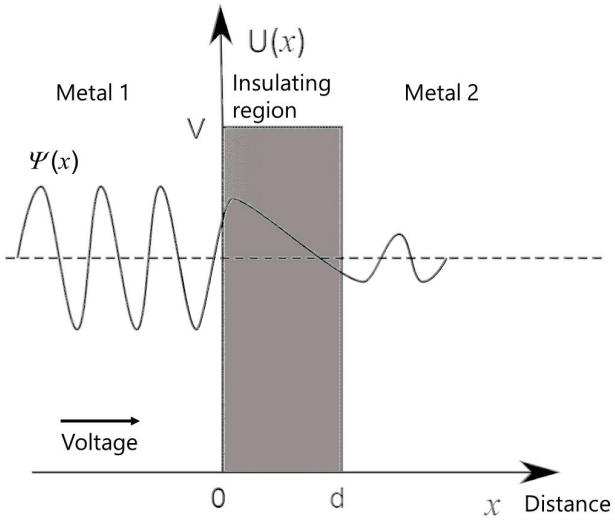

Figure 3.10: Tunneling process in the metal-insulator-metal junction. The wave function is extending smoothly across the tunneling junction.

3.5.2 Break-junction tunneling spectroscopy

We used the break-junction tunneling method [46, 47, 127] to record the differential conductance dI/dV as a function of the bias voltage V in a semiconductor-insulator-semiconductor (SIS) junction. The sample was shaped into a plate of $3 \times 2 \times 0.5$ mm^3 (Fig. 3.11). A groove was cut into the surface to be cracked perpendicularly in the middle. The sample plate was placed on a flexible substrate made of glass epoxy (Figs. 3.12 and 3.13), and from its back an adjustable force was applied to make a crack in a liquid-helium chamber. For the semiconducting sample, the junction is expressed as S_1–I–S_2. This process makes a clean interface of the SIS junction without any contamination and oxidation of reactive Ce in the materials. Generally, the tunneling current I largely depends on the junction resistance $R_{\rm J}$. The $R_{\rm J}$ increases exponentially as the distance of insulating barrier d is increased, as expressed by Eq. (3.27). This means that the $R_{\rm J}$ increases about one order of magnitude when d increases by a few Å. Therefore, the absolute value of tunneling spectrum dI/dV also changes drastically depending on d.

$$R_J = \exp(\frac{2\sqrt{2m\phi}}{\hbar}d). \tag{3.27}$$

In the case of scanning tunneling spectroscopy (STM) with a nano-scale tip, the contact area would be atomic scale. Then, the resistance in the vacuum tunneling would be above 10 kΩ ($= h/2e^2$). In our break-junction cases, however, a bulky sample of a rod sample with a cross section of 0.3×2 mm^2 was broken. The effective contact area would be of the order of submicron meters, containing many tunneling junctions in the interface. In facts, the small value of $R_{\rm J}$ in the range of 1 – 1000 Ω have been observed in previous BJTS works on the Kondo semiconductors [46, 47, 48, 49]. Then, we considered that the tunneling regime may dominate even at low junction resistance $R_{\rm J}$ as small as 10 – 1000 Ω.

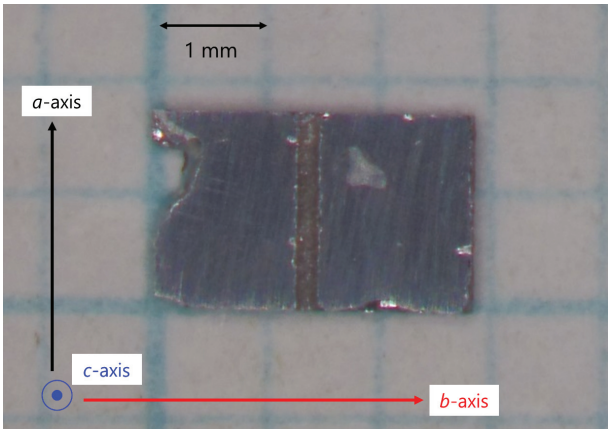

Figure 3.11: Single crystal of $CeFe_2Al_{10}$ with a groove used for the break-junction tunneling measurement.

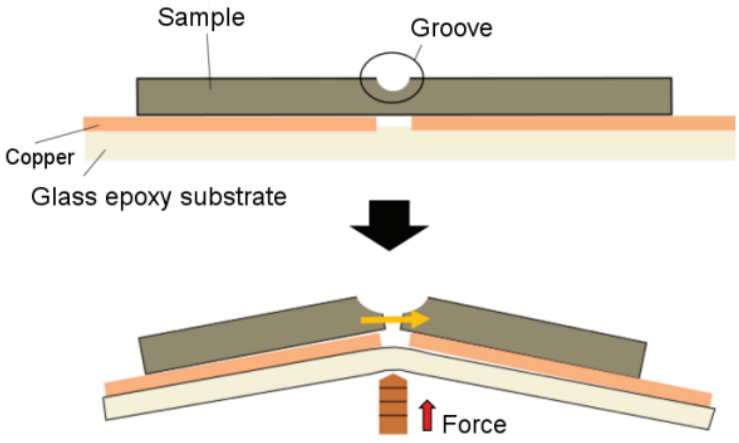

Figure 3.12: Breaking the sample with a groove by applying an adjustable bending force in liquid He at 4.2 K.

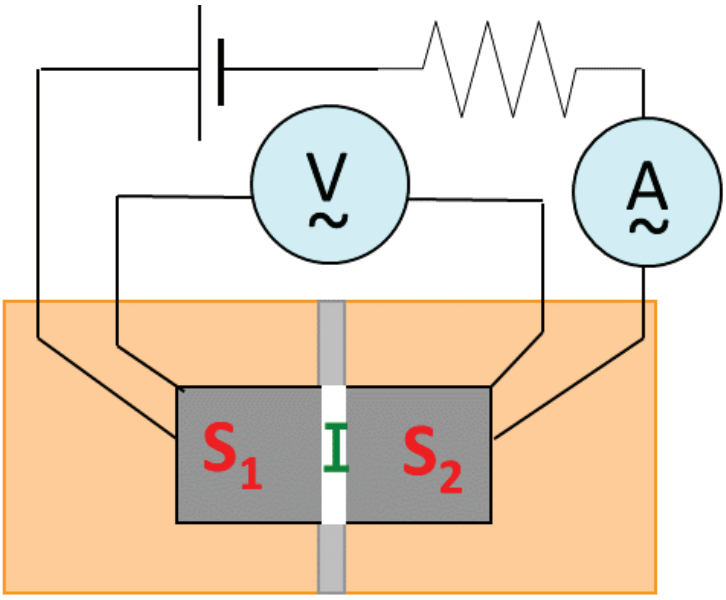

Figure 3.13: Schematic diagram of semiconductor 1 – insulator – semiconductor 2 (SIS) junction for a four-probe measurement of tunneling conductance.

Break-junction tunneling spectrum

We consider the tunneling probability across the insulating layer, leading to the equation of tunneling current I. The probability of transition P from S_1 to S_2 is expressed as

$$P = \frac{2\pi e}{\hbar}\langle 2|M|1\rangle^2 N_1(E), \tag{3.28}$$

where M is the tunneling matrix element and $N_1(E)$ is the density of state (DOS) in S_1. The $|1\rangle$ and $\langle 2|$ are the wave functions of S_1 and S_2 in Fig. 3.13. At $T = 0$, the tunneling current is given by

$$I\ (T = 0\mathrm{K}) = \frac{4\pi e}{\hbar}\int_{-\infty}^{\infty} |M_{1\to 2}|^2 N_1(E - eV)N_2(E)dE, \tag{3.29}$$

where V is the bias voltage between two electrodes.

At $T > 0$, the tunneling currents from S_1 to S_2, and from S_2 to S_1 are expressed as

$$I_{1\to 2} = \frac{4\pi e}{\hbar}\int_{-\infty}^{\infty} |M_{1\to 2}|^2 N_1(E - eV)N_2(E)f(E - eV)[1 - f(E)]dE \tag{3.30}$$

$$I_{2\to 1} = \frac{4\pi e}{\hbar}\int_{-\infty}^{\infty} |M_{2\to 1}|^2 N_1(E - eV)N_2(E)f(E)[1 - f(E - eV)]dE \tag{3.31}$$

where $f(E)$ is an equilibrium Fermi function shown in Fig. 3.14. In the difference of Fermi energy between both electrodes, $E_{\mathrm{F1}} - E_{\mathrm{F2}} = eV$, we describe the Fermi functions as

$$f_1 = [exp(\frac{E_1 - E_{\mathrm{F1}}}{k_{\mathrm{B}}T}) + 1]^{-1} = f(E - eV), \tag{3.32}$$

$$f_2 = [exp(\frac{E_2 - E_{\mathrm{F2}}}{k_{\mathrm{B}}T}) + 1]^{-1} = f(E). \tag{3.33}$$

Since the transition rate is assumed to be $|M_{1\to 2}|^2 = |M_{2\to 1}|^2 = |M|^2$ for the same semiconductors S_1 and S_2, the tunneling current is given by

$$I = I_{1\to 2} - I_{2\to 1} = \frac{2\pi e}{\hbar}\int_{-\infty}^{\infty} |M|^2 N_1(E - eV)N_2(E)[f(E - eV) - f(E)]dE \tag{3.34}$$

Then, the tunneling probability $P \propto |M|^2$ is expressed as

$$P \propto exp[-2\sqrt{\frac{2\mathrm{m}}{\hbar^2}}\ d(\phi - \frac{eV}{2} - W)^{1/2}], \tag{3.35}$$

where ϕ and W represent, respectively, the potential barrier and work function.

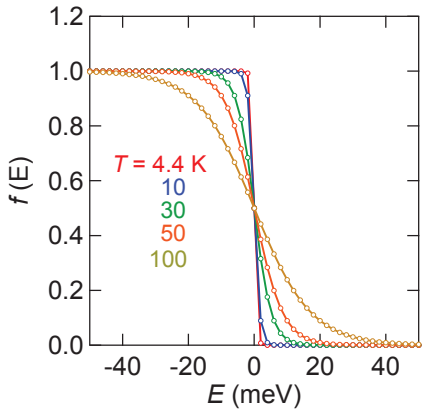

Figure 3.14: Temperature variations of the Fermi function $f(E)$.

Figure 3.15 shows the tunneling probabilities at various distances between two semiconducting electrodes. The probability increases with increasing the absolute value of $|V|$. When the distance d increases by 3%, the curve largely decreases. Therefore, any difference in the thermal expansion between the sample and the substrate changes the distance, making the junction unstable at elevated temperatures. In fact, we could not observe the reproducible dI/dV spectra on heating above 90 K.

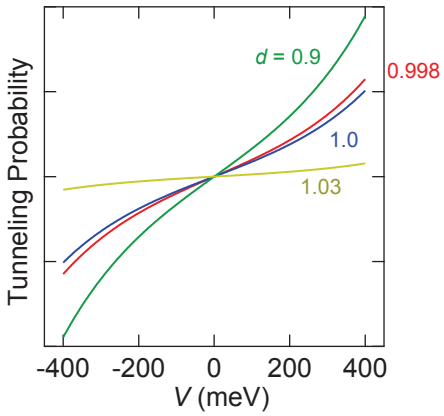

Figure 3.15: Tunneling probability of an SIS junction as a function of bias voltage V at various distances d.

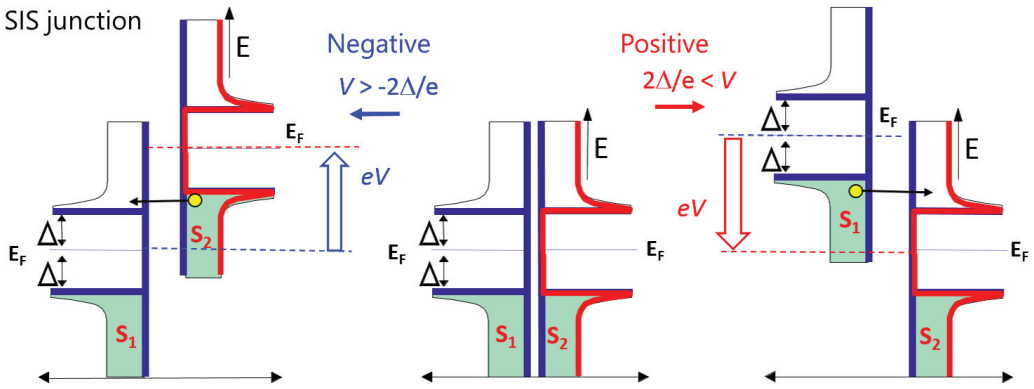

Figure 3.16: Schematic diagram of the tunneling process in an SIS junction

By differentiating the tunneling current I in Eq. (3.34), the tunneling conductance dI/dV of the SIS junction can be written as:

$$\begin{aligned}\frac{dI_{\rm SIS}}{dV} &= A\int_{-\infty}^{\infty}|M|^2\frac{dN_1(E-eV)}{dV}N_2(E)[f(E-eV)-f(E)] \\ &\quad +N_1(E-eV)N_2(E)[-\frac{df(E-eV)}{dV}]dE. \end{aligned} \tag{3.36}$$

Figure 3.16 illustrates the tunneling process in the SIS junction. The Δ is defined as the energy difference from $E_{\rm F}$ to the bottom of the upper band. When $|V|$ is increased to $2\Delta/e$, where e (>0) is the elementary electron charge, the electrons suddenly tunnel from the lower occupied band of one electrode (S_1) to the upper unoccupied band of the other electrode (S_2). Thereby, a symmetric pair of sharp gap edges appear in the dI/dV spectrum, as described below.

By using Eq. (3.36), the tunneling spectra dI/dV are calculated for the Kondo semiconductors with the V-shaped and U-shaped gaps in the DOS. The DOS's are described by the Eqs. (3.37)–(3.38) and (3.39)–(3.40), respectively.

$$N_{\rm V}(E) = \frac{C}{E^2+(D/2)^2}+N_c \qquad (|E|\le\Delta) \tag{3.37}$$

$$= (\frac{C}{(\Delta)^2+(D/2)^2}-N_r)\times\frac{|E|}{\Delta}+N_r+N_c \qquad (\Delta<|E|) \tag{3.38}$$

$$N_{\rm U}(E) = 0 \qquad (|E|\le\Delta) \tag{3.39}$$

$$= \frac{|E|}{\sqrt{E^2-(\Delta)^2}} \qquad (\Delta<|E|) \tag{3.40}$$

Here, N_c means the DOS of the conduction electrons, and N_r is the residual DOS at $E_{\rm F}=0$. Figures 3.17(a) and 3.18(a) display the DOS's, respectively. The DOS

with the V-shaped gap leads to the V-shaped form in the dI/dV spectrum as shown in Fig. 3.17(b). When the DOS has a full gap, by contrast, the dI/dV spectrum shows a U-shaped structure (Fig. 3.18(b)). The peak-to-peak separation V^{P-P} in the break-junction tunneling spectrum is equal to $4\Delta/e$.

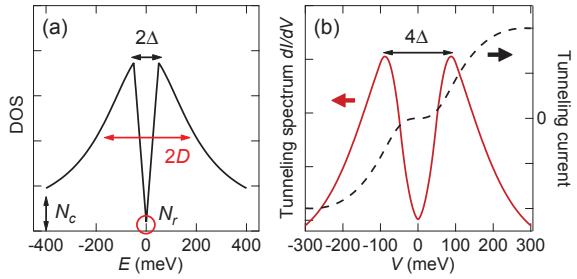

Figure 3.17: (a) The V-shaped DOS described by Eqs. (3.37) and (3.38) where $\Delta = 50$ meV is the gap width, $D = 400$ meV is the half width of Lorentzian shape DOS, N_r is the residual DOS at Fermi energy $E_{\rm F}$, and N_c is DOS of the conduction electrons. (b) The solid and broken curves represent the calculated tunneling conductance dI/dV and current for the SIS junction, respectively.

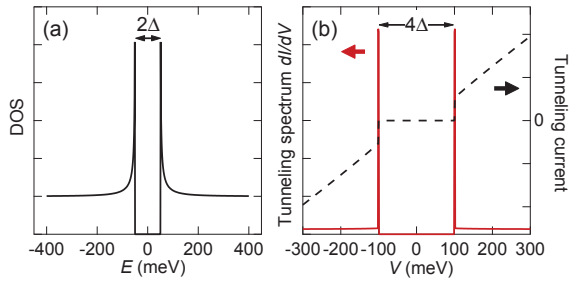

Figure 3.18: (a) The U-shaped DOS described by the Eqs. (3.39) and (3.40) where $\Delta = 50$ meV is the gap width. (b) The solid and broken curves represent the calculated tunneling conductance dI/dV and current for the SIS junction, respectively.

The c-f hybridization gap widths $2\Delta_1$ and $2\Delta_2$ for Kondo semiconductors observed by the break-junction tunneling, photoemission spectroscopy, and optical conductivity are listed in Table 3.1. For Kondo semiconductors CeRhAs and YbB_{12}, the gaps observed by BJTS are 2 – 5 times larger than those observed by optical conductivity and photoemission measurements, whose reason remains unclarified.

Table 3.1: Gap widths $2\Delta_1$ and $2\Delta_2$ for Kondo semiconductors observed by the break-junction tunneling, optical conductivity (OC), and photoemission spectroscopy (PES) measurements.

	BJTS		OC		PES		Ref.
Compound	$V_1/2$ (meV)	$V_2/2$ (meV)	$2\Delta_1$ (meV)	$2\Delta_2$ (meV)	$2\Delta_1$ (meV)	$2\Delta_2$ (meV)	
YbB_{12}	220	–	25 – 40	–	20 or 200	–	[43, 45, 49]
CeNiSn	–	8 – 10	–	10	–	–	[44, 46, 47]
CeRhSb	–	20 – 27	–	15	60 – 70	25 – 60	[44, 46]
CeRhAs	500	180	–	100	180 – 200	100 – 120	[42, 48]

Measurement of the tunneling current

The differential conductance dI/dV as a function of the bias voltage V was measured by the AC-modulation technique with the four-probe method. The schematic diagram of the overall circuit is shown in Fig. 3.19. The V is swept slowly ($V_0(t)$) with the addition of a sinusoidal component, $V(t) = V_0(t) + dV(\cos\ 2\pi ft)$. The $V_0(t)$ was applied with the DC power source (Agilent E3630A) and a function generator (KEITHLEY 3990), and dV was generated by another function Generator (Hewlett-Packard 3325B). The principle of harmonic detection is described by the expansion of $I(V_0 + dV)$ with respect to the modulation amplitude dV in the case of $dV << V_0$:

$$\begin{aligned} I(V_0 + dV) &= I(V_0) + \frac{dI(V_0)}{dV}dV + \frac{1}{2}(\frac{d^2I(V_0)}{dV^2})(dV)^2 \\ &= I(V_0) + \frac{dI(V_0)}{dV}V\cos 2\pi ft + \frac{1}{2}(\frac{d^2I(V_0)}{dV^2})(V\cos 2\pi ft)^2 + ... \\ &= I(V_0) + \frac{dI(V_0)}{dV}V\cos 2\pi ft + \frac{1}{2}(\frac{d^2I(V_0)}{dV^2})(V^2\frac{1+\cos 4\pi ft}{2}) + ..(3.41) \end{aligned}$$

The signal at the frequency of $2\pi f$ which is proportional to dI/dV was detected by the lock-in amplifier (EG& G model 124A). The correct tunneling conductance dI/dV was detected by keeping the amplitude dV constant. The dV determines the resolution in the derivative conductance. Since the tunneling current is very weak ($< 1\mu$A), the signal was amplified by using an operational amplifier (Op-Amp) with a variable resister.

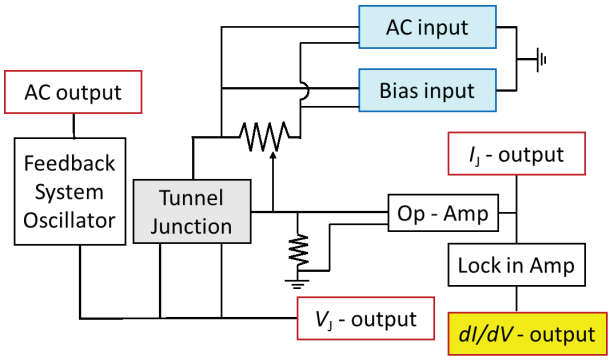

Figure 3.19: Schematic diagram of the overall circuit to measure the derivative conductance of the SIS junction.

Chapter 4

Results and discussion

4.1 Magnetic, transport, and thermal properties of $CeOs_2Al_{10}$ doped with $4f/5d$ holes and $5d$ electrons

Magnetic susceptibility

Figures 4.1– 4.3 display the temperature variations of magnetic susceptibility $M/B = \chi(T)$ and the inverse for $Ce_{1-z}La_zOs_2Al_{10}$ ($z \leq 0.51$), $Ce(Os_{1-y}Re_y)_2Al_{10}$ ($2y \leq 0.2$), and $Ce(Os_{1-x}Ir_x)_2Al_{10}$ ($2x \leq 0.3$), respectively. The value is normalized per Ce mol for the data of $Ce_{1-z}La_zOs_2Al_{10}$. For the undoped sample, $\chi(T)$ in $B \parallel a = 1$ T passes through a maximum at around 45 K and drops at $T_N = 28.5$ K. When z is increased to 0.24, the broad maximum disappears but a weak anomaly still exists at $T_N = 10.0$ K. For $z = 0.51$, $\chi_a(T)$ continues to increase on cooling to 2 K. We note that the decrease in $\chi(T)$ at $T < T_N$ along the three principal disappears for $z \geq 0.096$, and the values of $\chi(T)$ for $B \parallel b$ are essentially unchanged. The inverse of $\chi(T)$ for $B \parallel a$ versus T is shown in Fig. 4.1 (b). The Curie-Weiss fit to the data between 200 to 300 K gives the paramagnetic Curie temperature Θ_P, whose absolute value stays at 22 – 30 K for $z \leq 0.51$, as shown in Fig. 4.4. The fitting also yields the effective magnetic moment $\mu_{eff} = 2.62$ – 2.66 μ_B/Ce for $z \leq 0.51$. The fact that both Θ_P and μ_{eff} are insensitive to the doping of $4f$ holes in $CeOs_2Al_{10}$ indicates that the $4f$-hole doping does not alter the c-f hybridization at high

temperature.

Figure 4.2 displays the temperature dependences of $\chi(T)$ for $5d$-hole doped system $Ce(Os_{1-y}Re_y)_2Al_{10}$ ($2y \leq 0.2$). As $2y$ is increased, the drop at T_N disappears at $2y = 0.06$, and the maximum in $\chi_a(T)$ at around 45 K is suppressed and disappears at $2y = 0.2$. On cooling to 2 K, the continuous increase in $\chi_a(T)$ may be the effect of disorder-induced magnetic moments. As shown in Fig. 4.2 (b), the Curie-Weiss fit to the inverse of $\chi_a(T)$ at temperatures above 200 K yields the negative θ_P values in the whole range $0 \leq 2y \leq 0.2$. The increase of $|\theta_P|$ from 24 K for $2y = 0$ to 46 K for $2y = 0.2$ shown in Fig. 4.4 suggests the increase of T_K because the value of T_K for the overall CEF levels is proportional to $|\theta_P|$ [92]. This indicates the tendency of delocalization of $4f$ states in $Ce(Os_{1-y}Re_y)_2Al_{10}$.

As shown in Fig. 4.3, an opposite trend is observed in $5d$-electron doped system $Ce(Os_{1-x}Ir_x)_2Al_{10}$. On going from $2x = 0$ to 0.3, the broad maximum changes to a sharp peak, whose temperature decreases to 7 K. Thereby, the value at the maximum increases by five times, leading to the enhancement of anisotropy, $\chi_a \gg \chi_c > \chi_b$. It is worth noting that the data set of $\chi_i(T)$ ($i = a, b, c$) for $2x = 0.3$ at $T > 30$ K are in agreement with the calculation taking account of the CEF effect on the localized $4f$ state of the Ce^{3+} ion. The solid lines in Fig. 4.3 are the calculations using the CEF parameters which were determined by the x-ray absorption spectroscopic study on $CeOs_2Al_{10}$ [80]. The calculated $\chi(T)$ is consistent with the data for $2x = 0.3$ much better than those for $2x = 0$, confirming the localization of $4f$ state. As shown in Fig. 4.3 (b), the Curie-Weiss fit to the data of $\chi^{-1}(T)$ for $B \parallel a$ above 200 K gives the paramagnetic Curie temperature θ_P whose value changes from -20 K for $2x = 0$ to $+24$ K for $2x = 0.3$. For $B \parallel c$, the decrease in $\chi(T)$ at $T < T_N$ disappears with increasing $2x$. For $2x \geq 0.16$, the sharp peak in $\chi_a(T)$ at T_N and the absence of the drop in $\chi_c(T)$ at $T < T_N$ suggest the AFM ordered moments μ_{AF} are oriented parallel to the easy a axis. This reorientation of μ_{AF} from the c axis to the a axis is confirmed by the isothermal magnetization and neutron diffraction measurements [109].

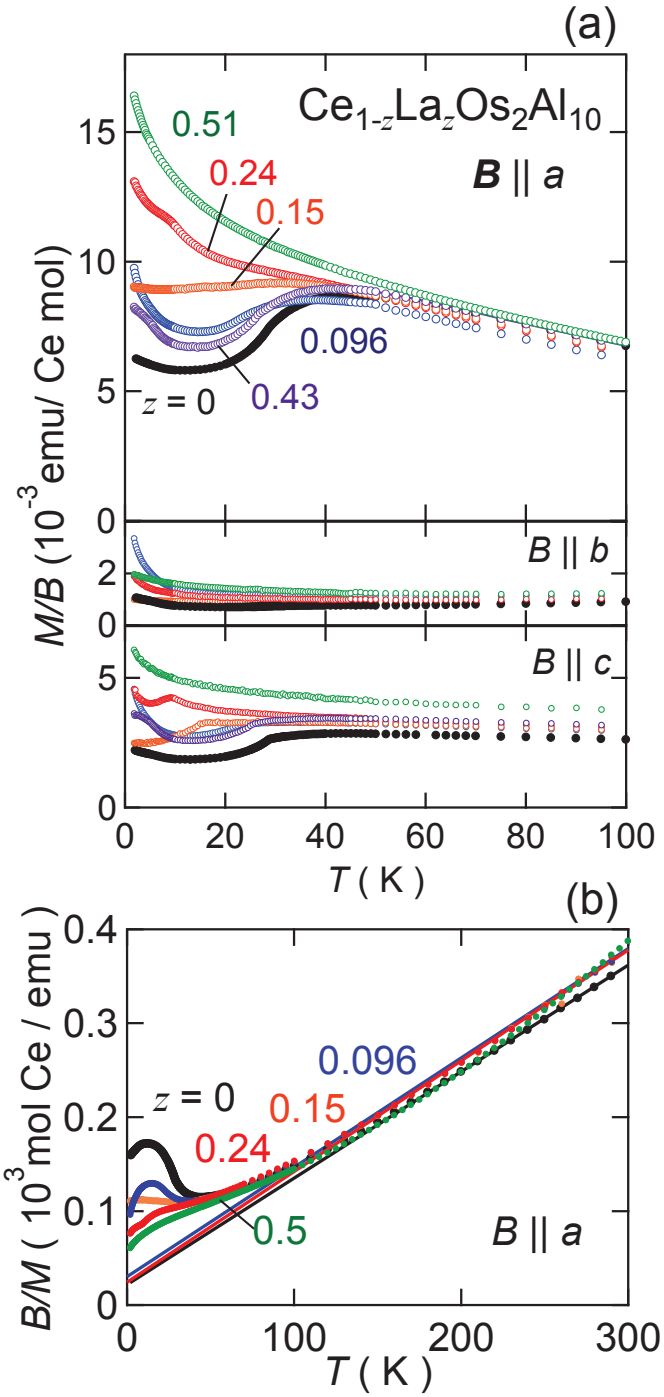

Figure 4.1: Temperature dependences of (a) magnetic susceptibility M/B along the three principal axes and (b) B/M along a axis for the single crystals of $Ce_{1-z}La_zOs_2Al_{10}$.

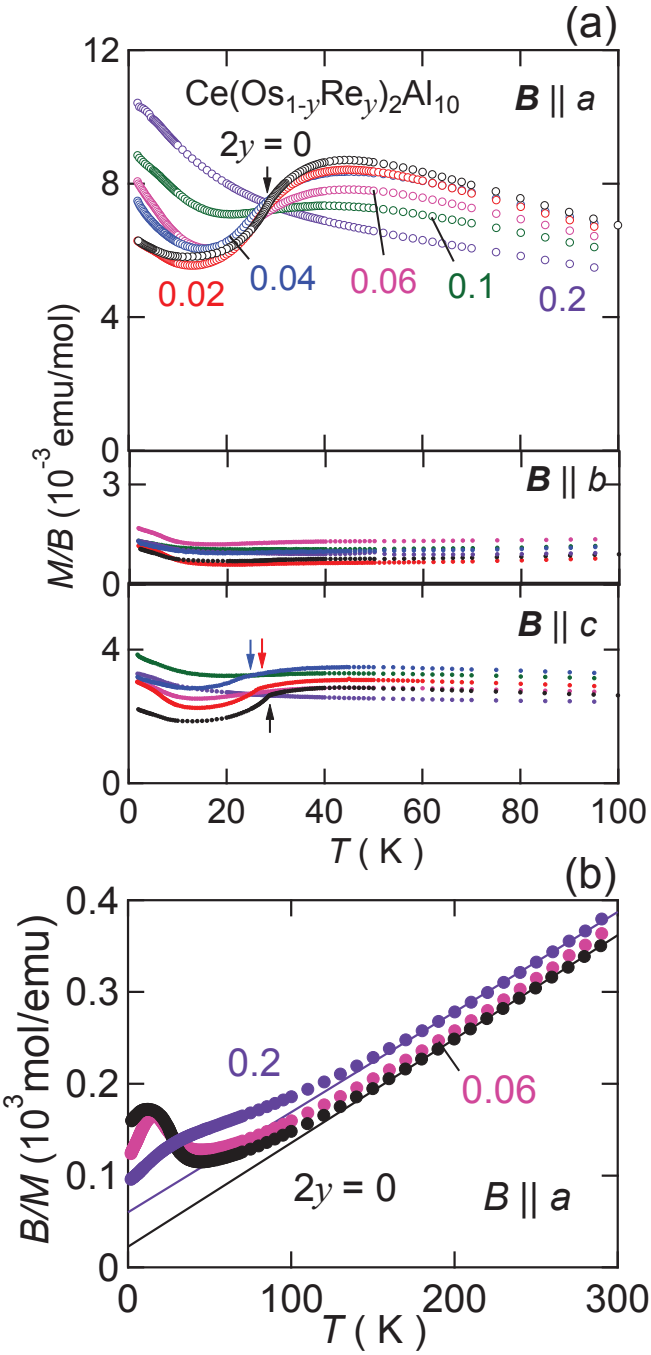

Figure 4.2: Temperature dependences of (a) magnetic susceptibility M/B along the three principal axes and (b) B/M along a axis for the single crystals of $Ce(Os_{1-y}Re_y)_2Al_{10}$. The arrows indicate T_N determined by the specific heat measurements.

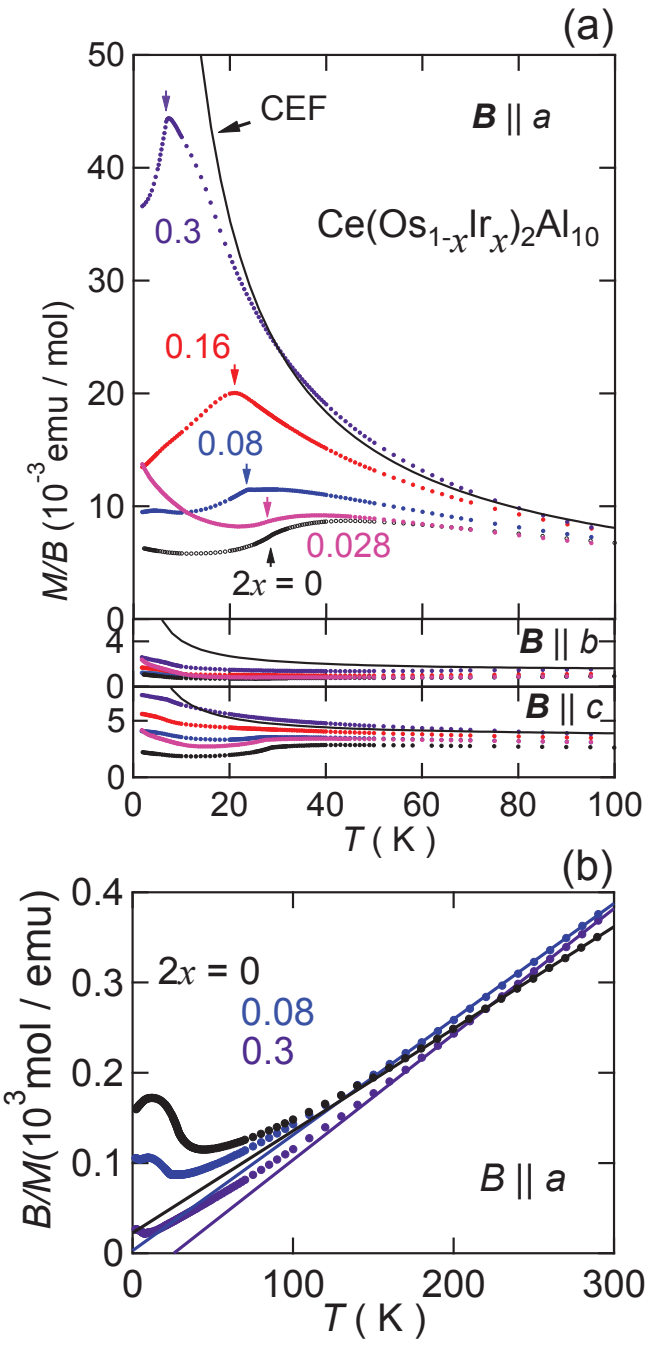

Figure 4.3: Temperature dependences of (a) magnetic susceptibility M/B along the three principal axes and (b) B/M along a axis for the single crystals of $Ce(Os_{1-x}Ir_x)_2Al_{10}$. The arrows indicate T_N determined by the specific heat measurements.

Magnetization

The magnetization curves $M(B)$ in applied magnetic fields $B \,||\, a$ and $B \,||\, c$ are shown in Figs. 4.5 (a), (b), and (c) for $Ce_{1-z}La_zOs_2Al_{10}$, $Ce(Os_{1-y}Re_y)_2Al_{10}$, and $Ce(Os_{1-x}Ir_x)_2Al_{10}$, respectively. In the undoped system, a metamagnetic transition was observed by applying B along the c axis at 6.1 T [72]. This transition was assigned as a spin flop transition with the change from $\mu_{\rm AF} \,||\, c$ to $\mu_{\rm AF} \perp c$, because the linear extrapolation of the M ($B \,||\, c$) data between 8 and 14 T goes to the origin. When z is increased to 0.24, the metamagnetic anomaly still exists at $B \,||\, c = 2.5$ T, indicating the direction of $\mu_{\rm AF}$ to be kept along the c axis. The $M(B)$ curves for $B \,||\, a$ and $B \,||\, b$ do not show any anomaly up to 14 T. This result is in agreement with the AFM structure for $z = 0.1$ with $\mu_{\rm AF} \,||\, c = 0.23$ μ_B/Ce, which was determined by neutron diffraction experiments [100].

In Fig. 4.5 (b), the metamagnetic behavior in $M(B \,||\, c)$ is also observed in $Ce(Os_{1-y}Re_y)_2Al_{10}$ up to $2y = 0.04$. It is not seen for $2y = 0.1$ in consistent with the absence of anomaly in $\chi_a(T)$ in Fig. 4.2 (b). The $M(B \,||\, a)$ curves for all $2y$ show the linear increase with B, suggesting that the AFM order with $\mu_{\rm AF} \,||\, c$ fades away without showing reorientation.

When $2x$ is increased to 0.06, however, there is no transition in $M(B \,||\, c)$ but a weak upturn appears in $M(B \,||\, a)$ at around 3 T as shown in Fig. 4.5 (c). For $2x = 0.16$, a metamagnetic transition and a bend in $M(B \,||\, a)$ manifest clearly at 3.0 and 10.4 T, respectively. Moreover, the $M(B \,||\, a)$ is saturated to a large value of 0.7 $\mu_{\rm B}$/Ce. For $2x = 0.3$, the magnitude of $M(B \,||\, a)$ increases further but the spin-flop transition field $B_{\rm sf}$ does not change. These results suggest that the ground state for $2x \geq 0.16$ is in the AFM state with $\mu_{\rm AF}(\sim 1\mu_{\rm B}/{\rm Ce})$ pointing along the a axis.

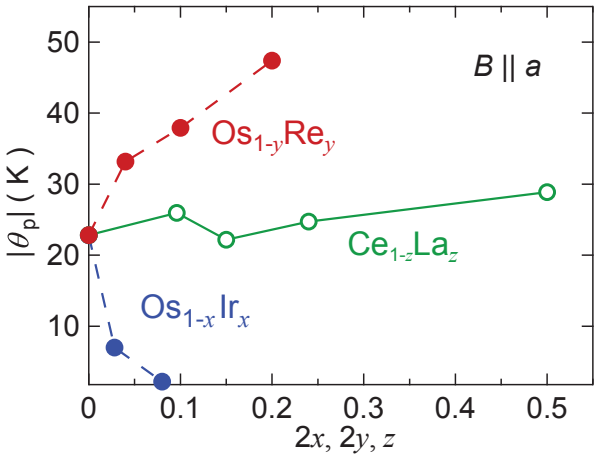

Figure 4.4: The absolute value of the paramagnetic Currie temperature $|\Theta_{\rm P}|$ for $B \parallel a$ as functions of the doped hole/electron concentrations z, $2y$, and $2x$ in $Ce_{1-z}La_zOs_2Al_{10}$, $Ce(Os_{1-y}Re_y)_2Al_{10}$ and $Ce(Os_{1-x}Ir_x)_2Al_{10}$.

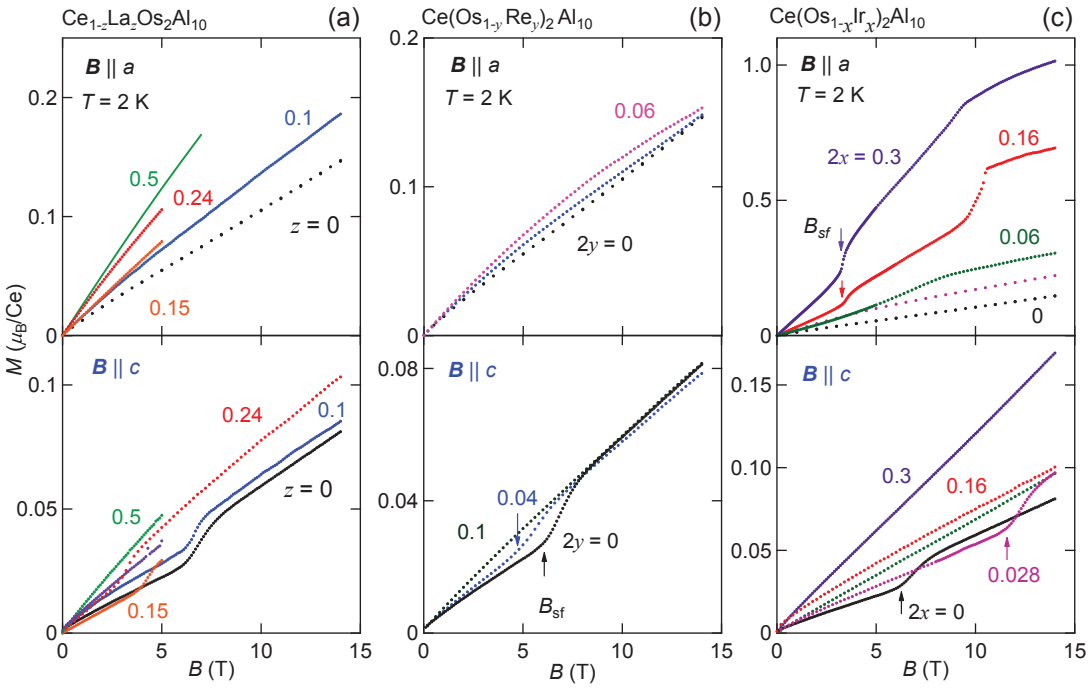

Figure 4.5: Isothermal magnetization curves of $M(B \parallel a)$ and $M(B \parallel c)$ at 2.0 K for $Ce_{1-z}La_zOs_2Al_{10}$, $Ce(Os_{1-y}Re_y)_2Al_{10}$, and $Ce(Os_{1-x}Ir_x)_2Al_{10}$, respectively.

Electrical resistivity

Effects of the doping on the hybridization gap above T_N and the AFM gap below T_N may manifest themselves in the temperature dependence of electrical resistivity $\rho(T)$. Figures 4.6 (a), (b), and (c) show the results of $\rho(T)$ along the three principal axes for the samples substituted with La, Re, and Ir, respectively. The vertical lines denote T_N's determined by the specific heat measurements as described below. For the non-doped sample, the $-\log T$ dependence from 300 to 100 K is followed by a thermal activation-type behavior in two regions, $80 > T > 30$ K and $16 > T > 5$ K, as shown in the inset of Fig. 4.6. Fitting the data between 80 and 30 K with the formula $\rho(T) = \rho_0 \exp(\Delta/2k_BT)$ gives the values of 56, 83, and 65 K for Δ_a/k_B, Δ_b/k_B, and Δ_c/k_B, respectively. At $T \leq$ 28.5 K, $\rho(T)$ increases abruptly. Below 16 K, $\rho(T)$ shows the semiconducting behavior along three directions. At a small doping level $z = 0.043$, the increase in $\rho(T)$ at $T < T_N$ becomes much stronger, reaching 4.2 mΩcm, twice the value for $z = 0$. As z is further increased to 0.096, the increase in $\rho(T)$ is weakened. For $z \geq 0.24$, $\rho(T)$'s no longer follow the activation type form but show -ln$T$ dependence in the whole temperature range.

In 5d-hole doped samples $Ce(Os_{1-y}Re_y)_2Al_{10}$, the semiconducting behavior at $T < 10$ K disappears even at a small level $2y = 0.02$ although the thermal activation behavior above T_N still exists as shown in Fig. 4.6 (b). On going from $2y = 0.02$ to 0.1, the metallic behavior at low temperatures becomes more evident. The anomaly at T_N is observed in $\rho_b(T)$ for $2y = 0.04$ but is hardly observed for $2y = 0.06$. It is noteworthy that the metallization below T_N occurs before the thermal activation behavior above T_N disappears. For $2y = 0.1$, the maximum of $\rho(T)$ shifts to high temperature and $\rho(T)$ at $T < 15$ K is proportional to T^2. For $2y = 0.2$, the temperature at the maximum further increases, suggesting the enhancement of T_K. The broad maximum at around 100 K is a characteristic of valence fuctuating Ce compounds.

In Fig. 4.6 (c), the magnitudes of Δ_a/k_B, Δ_b/k_B, and Δ_c/k_B for $2x = 0.08$ are approximately 80% of those for $2x = 0$. For $2x = 0.16$, only $\rho_a(T)$ displays the upward bend at T_N, which is consistent with the AFM arrangement of $\mu_{AF} \parallel a$ along the propagation vector (1, 0, 0) [109]. In addition, a hump manifests itself in $\rho_c(T)$ at around 200 K. The $-\log T$ dependence above the hump can be attributed to the Kondo scattering in the CEF excited state [123]. For $2x = 0.3$ and 0.54, the hump at around 200 K becomes

more evident in $\rho_a(T)$ and $\rho_c(T)$, but the anomaly at $T_{\rm N}$ becomes unclear. The decrease in $\rho(T)$ below 10 K may be attributed to the development of in-gap states or short-range order of localized moments. This metallization by the $5d$-electron doping occurs at a higher doping level than by the $5d$-hole doping.

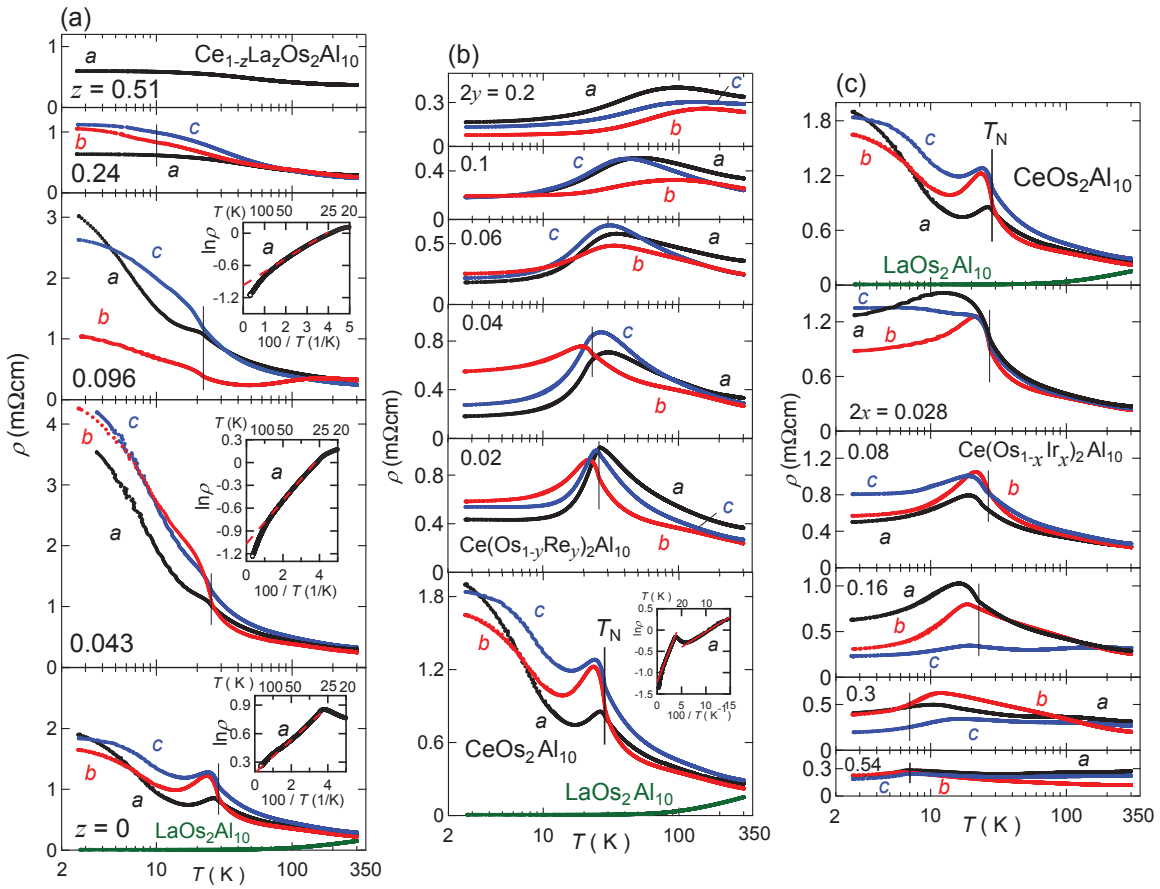

Figure 4.6: Temperature dependences of electrical resistivity $\rho(T)$ along the three principal axes for single crystals of (a) $Ce_{1-z}La_zOs_2Al_{10}$, (b) $Ce(Os_{1-y}Re_y)_2Al_{10}$, and (c) $Ce(Os_{1-x}Ir_x)_2Al_{10}$, respectively. The vertical lines denote the AFM ordering temperatures T_N determined by the specific heat measurement. The insets represent the Arrhenius plots of the resistivity.

Thermopower

The suppression of hybridization gap above $T_{\rm N}$ also manifests itself in the thermopower $S(T)$, because $S(T)$ is very sensitive to the energy dependence of the quasiparticle density of states at the chemical potential as well as the Fermi surface as expressed by Eq. (3.20) and Eq. (3.22). Figures 4.7 – 4.9 display the temperature dependences of $S_i(T)$ and $\rho_i(T)$ $(i = a, b, c)$ for $4f/5d$ hole- and $5d$ electron- doped samples, respectively. The solid lines indicate the AFM ordering temperature $T_{\rm N}$ determined by the specific heat measurement. At a glance, $S(T)$ of the undoped sample displays stronger anisotropy than in $\rho(T)$. Below 300 K, $S_i(T)$'s along the principle axes increase due to the Kondo scattering. At the maximum temperature $T_{S_{\rm max}}$, the absolute value of $S_b(T_{S_{\rm max}})$ is 3 times larger than those of $S_a(T_{S_{\rm max}})$ and $S_c(T_{S_{\rm max}})$. Between 80 and 30 K, where $\rho(T)$ exhibits the thermal activation behavior, $S_{\rm b}$ gradually decreases whereas $S_{\rm a}$ and $S_{\rm c}$ show shallow minima. It is worth noting that only $S_{\rm b}$ bends at $T_S = 36$ K. That is in concomitant with the opening of the charge excitation gap along the b axis as observed in the optical conductivity [95, 96]. As temperature is decreased below $T_{\rm N}$, $S_{\rm a}$ and $S_{\rm c}$ increase by a few μV/K in coincidence with the increase of $\rho(T)$. These increases are similar in size to those observed at $T_{\rm N}$ in $CeRu_2Al_{10}$ [99]. By contrast, only $S_{\rm b}$ decreases drastically from 30 to -7 μV/K. Such a large change in $S(T)$ at $T < T_{\rm N}$ has not been observed in CeT_2Al_{10} with T = Ru, Fe [99]. The anisotropic behaviors in $S(T)$ is difficult to understand in terms of either the temperature dependence of the energy derivative of c - f scattering relaxation time τ_{c-f} or the shape of quasiparticle density of states. Therefore, we suggest that a topological change of the Fermi surface causes such anisotropic behavior. If a part of the Fermi surface of the hybridization band is lost by the phase transition, $S(T)$ would change in a large size. In fact, $S_{\rm c}$ in URu_2Si_2 decreases by ΔS = 40 μV/K at the occurance of the "hidden order" at 17.5 K [124], where a large part of heavy-fermion Fermi surface is removed [125]. On further cooling, $S_{\rm a}$ and $S_{\rm c}$ of $CeOs_2Al_{10}$ reach negative values.

Let us move our attention to the $S(T)$ data for La-substituted samples $Ce_{1-z}La_zOs_2Al_{10}$. For a small doping level $z = 0.043$, S_i's at $T < 20$ K change sign from negative to positive. When z is increased to 0.096, $S_{\rm b}$ $(T_{\rm S_{max}})$ decreases to 25 μV/K whose value is similar to $S_{\rm a}$ $(T_{\rm S_{max}})$ and $S_{\rm c}$ $(T_{\rm S_{max}})$. The bend at $T_{\rm S}$ and decrease at $T_{\rm N}$ still remain in $S_{\rm b}(T)$, whereas there are no obvious anomalies in $S_{\rm a}$ and $S_{\rm c}$ at $T_{\rm N}$. At $z = 0.24$, the local

minimum in $S_{\rm a}(T)$ becomes shallower, in good agreement with the disappearance of the activation-type behavior in $\rho_i(T)$.

Figure 4.8 shows the temperature dependences of $S(T)$ and $\rho(T)$ for $Ce(Os_{1-y}Re_y)_2Al_{10}$. At $2y = 0.02$, $S_{\rm b}(T)$ remains positive down to 3 K in coincide with the disappearance of activation behavior in $\rho_{\rm b}(T)$ at $T < 16$ K. The temperature dependence of S_c is more drastic than that for $2y = 0$. For $2y \geq 0.04$, $S(T)$'s stay positive over the whole temperature range. In addition, the local minma of $S_{\rm a}$ and $S_{\rm c}$ become shallower, indicating the suppression of the hybridization gap above $T_{\rm N}$. The anomalies in $S_{\rm a}$ and $S_{\rm c}$ at $T_{\rm N}$ are no longer obvious. On the other hand, $S_{\rm b}$ at $2y = 0.04$ still bends at $T_{\rm S} = 30$ K and $T_{\rm N} = 21$ K. Ongoing from $2y = 0.04$ to 0.2, the double peaks in $S_{\rm a}$ and $S_{\rm c}$ changes to one large peak. One large positive peak in $S(T)$ is the characteristic feature of valence fluctuating Ce compounds such as CeNi, as shown in Fig. 1.25 [29]. It is consistent with the T^2 dependence of $\rho(T)$ below 10 K. These results imply that the system is transported from the Kondo semiconducting regime to the valence fluctuating metallic regime.

Let us pay our attention to the $5d$-electron doped system $Ce(Os_{1-x}Ir_x)_2Al_{10}$ as shown in Fig. 4.9. Small doping at $2x = 0.028$ drastically changes the T-dependence in $S_i(T)$. The jumps in $S_{\rm a}$ and $S_{\rm c}$ at $T_{\rm N}$ change to knees, and the drop $\Delta S_{\rm b} = 20\mu$V/K becomes comparable to those in other directions. In the range $0.028 \leq 2x \leq 0.08$, the deep minimum manifests in $S_{\rm c}$ below $T_{\rm N}$. For $2x = 0.16$, at $T > T_{\rm N}$, the absolute value of $S_{\rm c}$ decreases but that of $S_{\rm a}$ increases. For $2x = 0.3$, S_a is smaller than 10 μV/K in magnitude and becomes negative below 100 K. The small and negative value of $S_{\rm a}$ for $2x = 0.3$ is the hallmark of Ce AFM compounds with localized $4f$ electrons exemplified by CePtSn [57]. Moreover, there is no visible jump either at $T_{\rm N}$ in $S_{\rm b}(T)$ nor that in $\rho_b(T)$ whereas the bend at $T_{\rm S}$ still exists in $S_b(T)$.

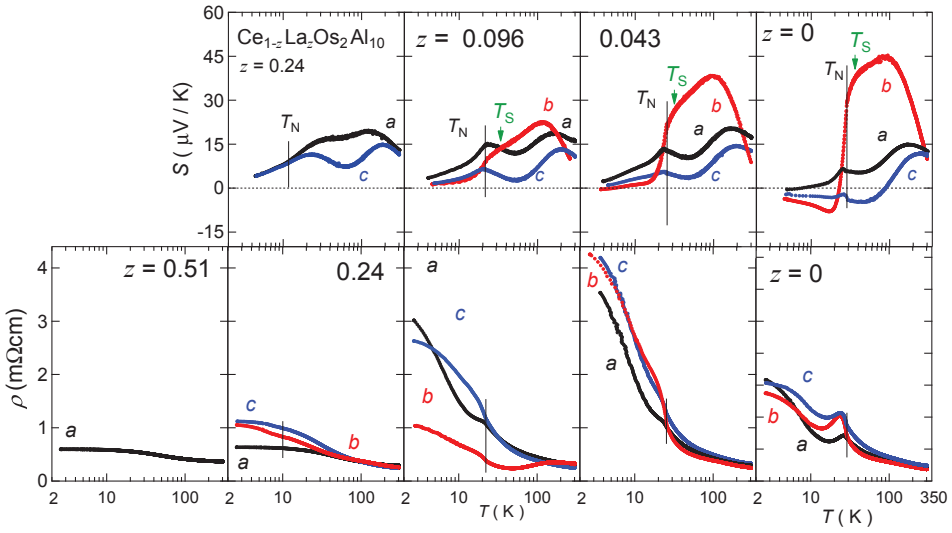

Figure 4.7: Temperature variations of themopower $S(T)$ and resistivity $\rho(T)$ along the three principal axes for single crystals of $Ce_{1-z}La_zOs_2Al_{10}$ ($0 \leq z \leq 0.51$). The solid lines indicate the AFM ordering temperatures T_N which are defined by the specific heat measurement.

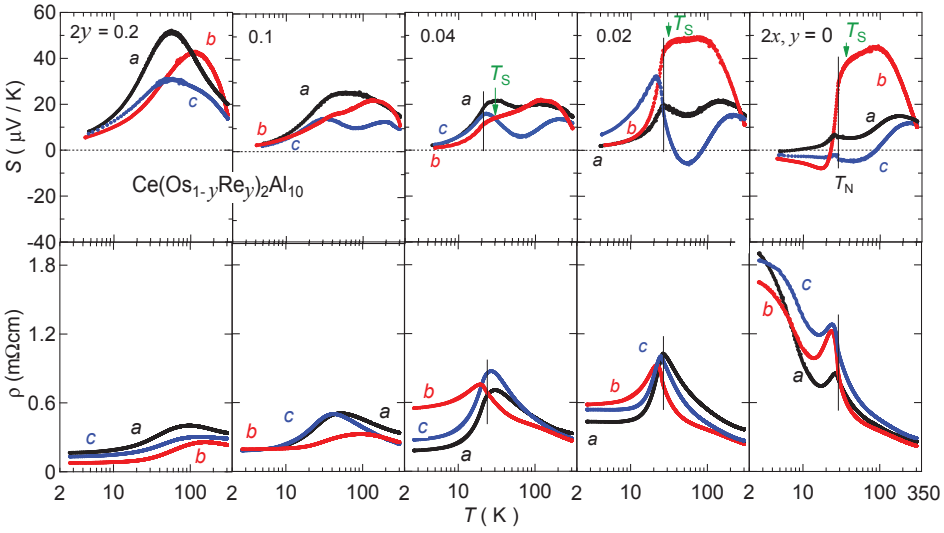

Figure 4.8: Temperature dependences of themopower $S(T)$ and resistivity $\rho(T)$ along the three principal axes for single crystals of $Ce(Os_{1-y}Re_y)_2Al_{10}$ ($0 \leq 2y \leq 0.2$). The solid lines denote the AFM ordering temperatures T_N.

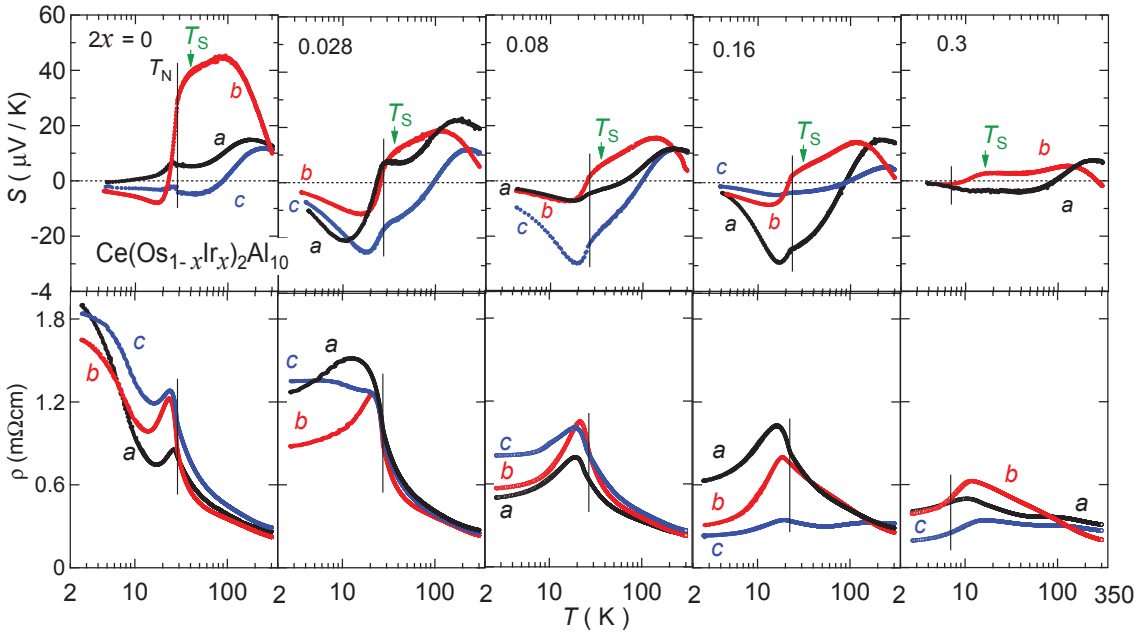

Figure 4.9: Temperature variations of themopower $S(T)$ and resistivity $\rho(T)$ along the three principal axes for single crystals of $Ce(Os_{1-x}Ir_x)_2Al_{10}$ ($0 \leq 2x \leq 0.3$). The solid lines represent the AFM ordering temperatures T_N.

Specific heat

The temperature dependences of specific heat C and magnetic specific heat $C_{\rm m}$ are plotted in the forms of C/T and $C_{\rm m}/T$ in Figs. 4.10 – 4.12 for the La-, Re-, and Ir-substituted systems, respectively. Thereby, the values of C for $LaOs_2Al_{10}$ were subtracted from those for the substituted samples to estimate the values of $C_{\rm m}$. The midpoint of the jump in C/T was taken as $T_{\rm N}$. For the non-doped sample, C/T shows a sharp jump at $T_{\rm N} = 28.5$ K [71, 72]. The extrapolation of the plot C/T versus T^2 to $T = 0$ gives the Sommerfeld coefficient γ of 7 mJ/K^2 mol. With increasing z, the jump in C/T gradually decreases. A weak anomaly is noticeable at 10 K for $z = 0.24$, but no jump is observed down to 2 K for $z \geq 0.35$. As shown in Fig. 4.10 (b), a sharp peak of $C_{\rm m}/T$ at $T_{\rm N}$ for $z = 0$ is gradually smeared out by doping $4f$ holes. When z is increased to 0.15, $\Delta C_{\rm m}/T$ decreases rapidly, but the value of $T_{\rm N}$ gradually decreases. The extrapolated values of $\gamma_{\rm m}(C_{\rm m}/T$ at $T = 0)$ are 21 and 133 mJ/ Ce K^{2}mol for $z = 0.05$ and 0.51, respectively.

In Fig. 4.11 (a), with increasing $2y$ in $Ce(Os_{1-y}Re_y)_2Al_{10}$, the jump shifts to low temperatures and becomes significantly broader, and fade away at $2y = 0.1$. The γ value reaches 100 mJ/K^{2}mol at $y = 0.2$. The increasing rate of γ with respect to $2y$ is 3 times higher than that with respect to z. Let us turn our attention to the result of C/T of $5d$-electron doped system $Ce(Os_{1-x}Ir_x)_2Al_{10}$ in Fig. 4.12. When $2x = 0.08$ and 0.16, $T_{\rm N}$ decreases and the jump becomes smaller. For $2x = 0.3$, C/T gradually increases on cooling from 17 K and exhibits a jump at 7 K, whose temperature agrees with that of the sharp peak in $\chi_a(T)$ in Fig. 4.3 (a). Figure 4.13 shows the magnetic entropy $S_{\rm m}$ estimated by integrating $C_{\rm m}/T$ versus T over the entire temperature range. For the non-doped sample, $S_{\rm m}$ bends downward at $T_{\rm N}$, where $S_{\rm m}$ reaches 0.35 Rln2. The decreasing rate in $S_{\rm m}$ below $T_{\rm N}$ is weakened with increasing z, $2y$, and $2x$. The value of $S_{\rm m}(T_{\rm N})$ decreases by the doping of $4f$ holes and $5d$ holes, whereas it increases by the doping of $5d$ electrons.

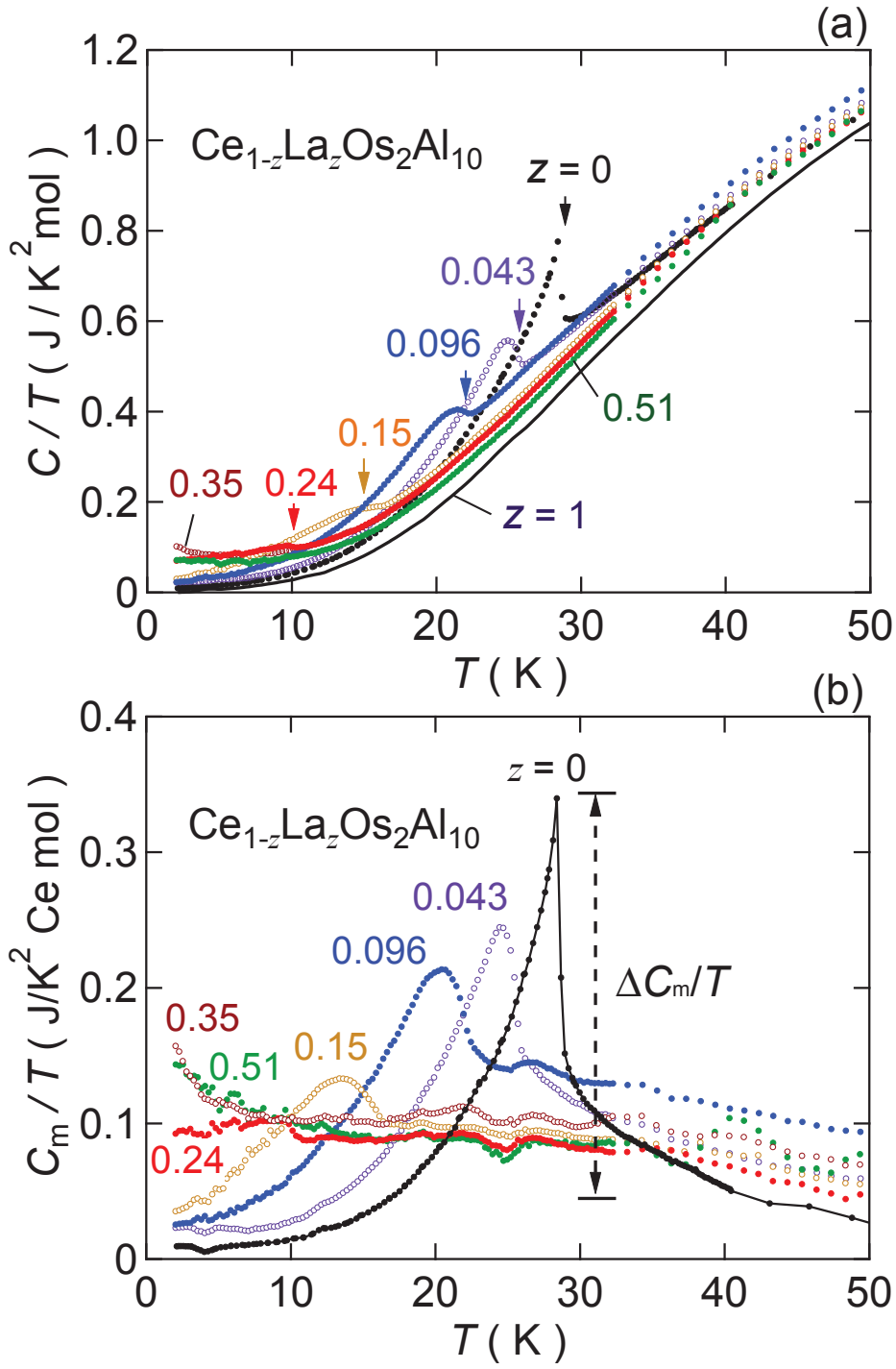

Figure 4.10: Temperature dependences of the specific heat C and magnetic magnetic part $C_{\rm m}$ plotted in the forms of (a) C/T and (b) $C_{\rm m}/T$ for $Ce_{1-z}La_zOs_2Al_{10}$. The arrows indicate the midpoint of the anomaly in C/T, which is taken as $T_{\rm N}$.

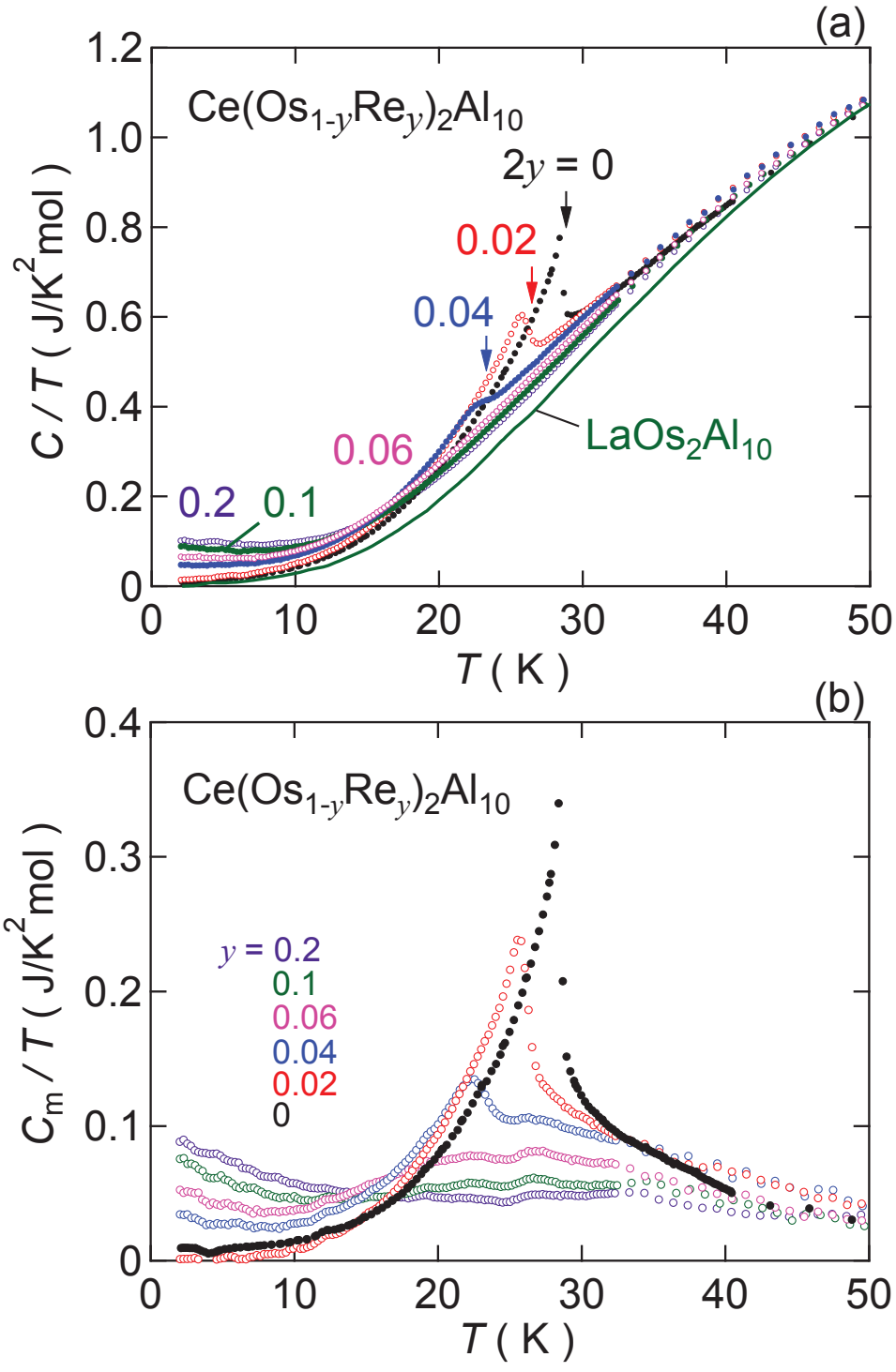

Figure 4.11: Temperature dependences of (a) C/T and (b) $C_{\rm m}/T$ for $Ce(Os_{1-y}Re_y)_2Al_{10}$. The arrows indicate the $T_{\rm N}$.

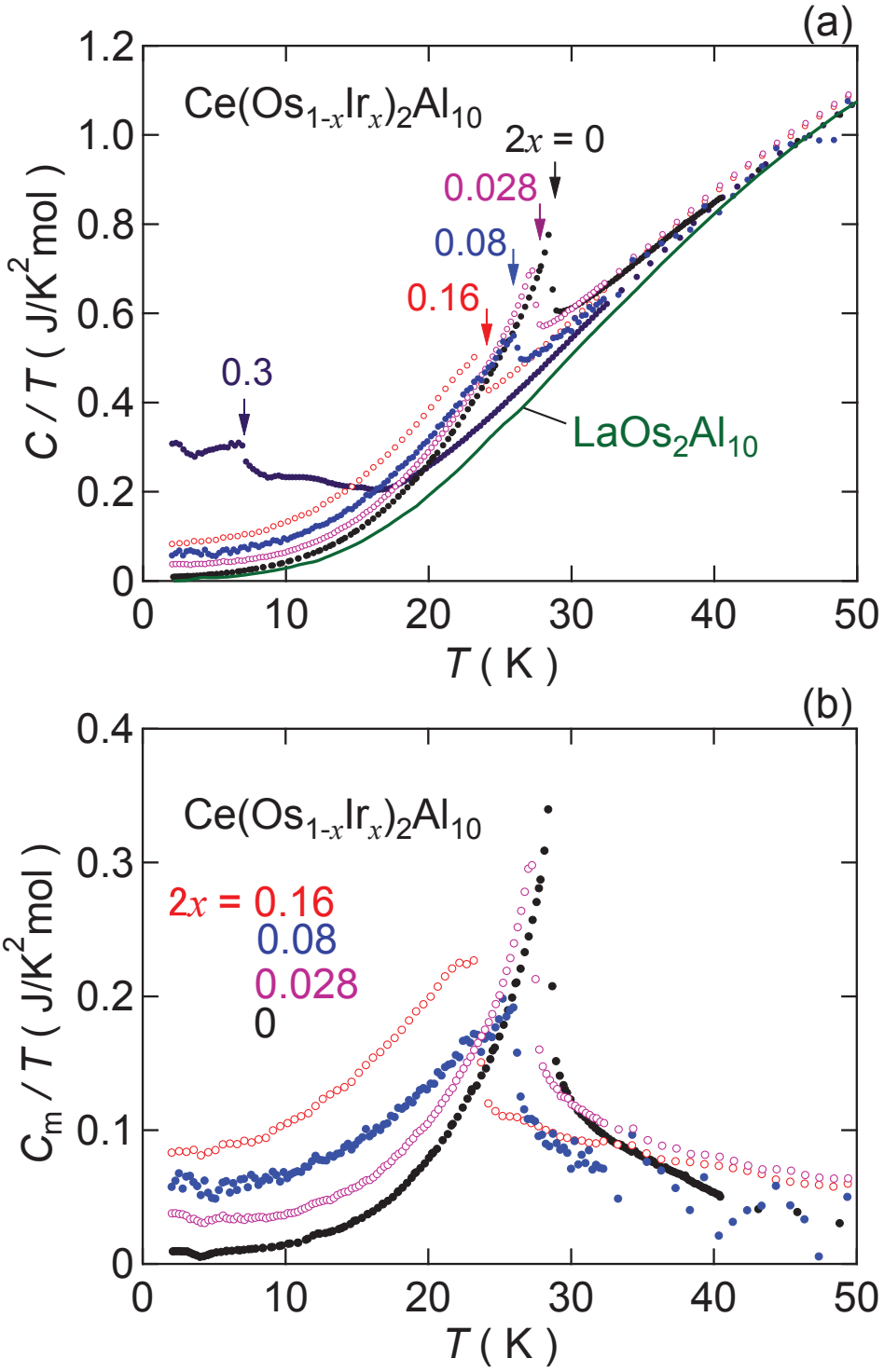

Figure 4.12: Temperature dependences of (a) C/T and (b) $C_{\rm m}/T$ for $Ce(Os_{1-x}Ir_x)_2Al_{10}$. The arrows indicate $T_{\rm N}$.

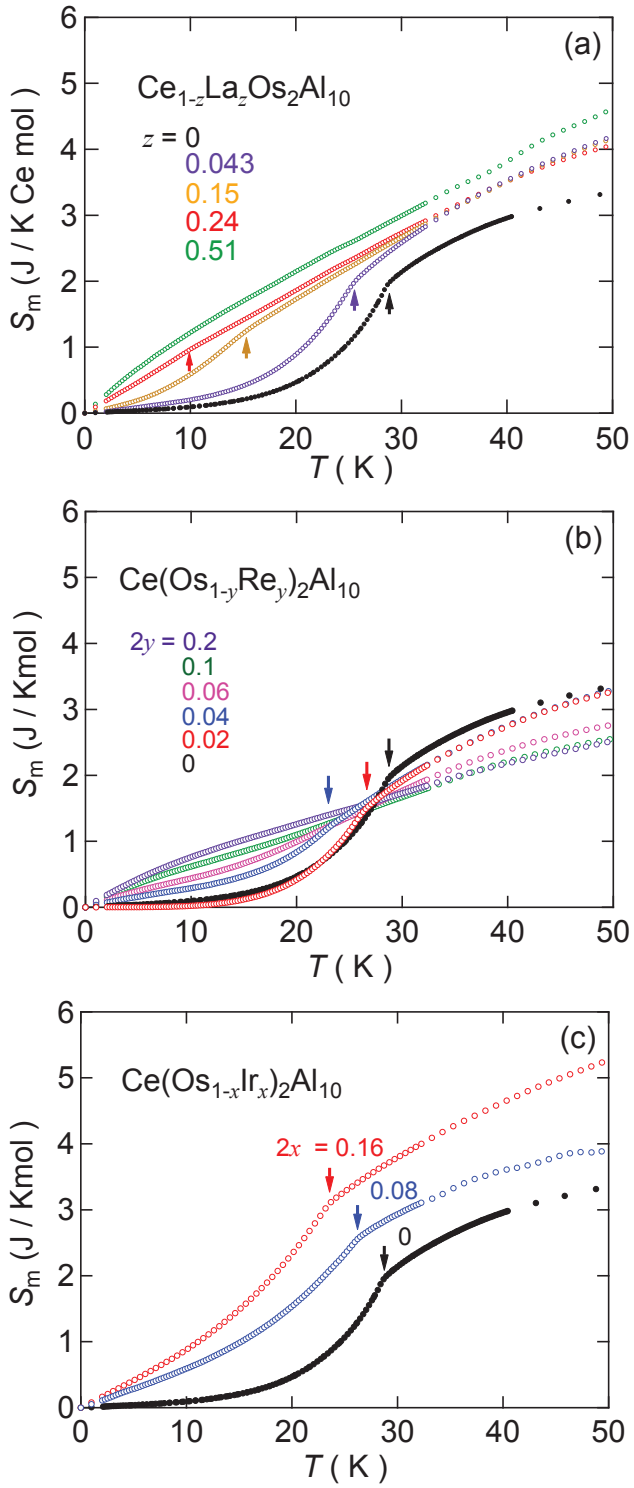

Figure 4.13: Temperature dependences of the magnetic entropy $S_{\rm m}$ for (a) $Ce_{1-z}La_zOs_2Al_{10}$, (b) $Ce(Os_{1-y}Re_y)_2Al_{10}$, and (c) $Ce(Os_{1-x}Ir_x)_2Al_{10}$. The arrows indicate $T_{\rm N}$.

Discussion

Firstly, we discuss the relation between the AFM transition and the magnetic structure. Figure 4.14 shows the plots of $T_{\rm N}$, $B_{\rm sf}$ at 2.0 K, $S_{\rm m}$ at $T_{\rm N}$, and $M(B \parallel a = 14$ T) at 2.0 K as functions of z, $2y$, and $2x$. The decrease in $T_{\rm N}$ with increasing z, $2y$, and $2x$ is most drastic as a function $2y$. In the $4f$-hole doped system $Ce_{1-z}La_zOs_2Al_{10}$, $B_{\rm sf}$ decreases with increasing z above z =0.1. In the $5d$-hole doped system $Ce(Os_{1-y}Re_y)_2Al_{10}$, by contrast, $B_{\rm sf}$ is strongly suppressed to zero at $2y = 0.1$. The degree of suppression of $B_{\rm sf}$ seems to be correlated with those in $T_{\rm N}$ and $S_{\rm m}(T = T_{\rm N})$ for $4f$-hole and $5d$-hole doped systems. Moreover, these suppressions in $B_{\rm sf}$, $T_{\rm N}$, and $S_{\rm m}$ are consistent with the decrease in $\mu_{\rm AF}$. The magnitude of $\mu_{\rm AF}$ decreases from 0.3 $\mu_{\rm B}$/Ce for $z = 0$ to 0.23 $\mu_{\rm B}$/Ce for $z = 0.1$ and to 0.18 $\mu_{\rm B}$/Ce for $2y = 0.06$ [100, 110]. Note that all suppressions in $4f$-hole doped system are much weaker than those in $5d$-hole doped system. When $2x$ is increased to 0.06 in $Ce(Os_{1-x}Ir_x)_2Al_{10}$, the direction of $\mu_{\rm AF}$ is reoriented from $\parallel c$ to $\parallel a$. In the range $0.06 \leq 2x \leq 0.3$, the magnitude of $B_{\rm sf}$ along the a axis is constant. The reorientation and increase of ordered moments from $\mu_{\rm AF} \parallel c = 0.3$ $\mu_{\rm B}$/Ce for $2x = 0$ to $\mu_{\rm AF} \parallel a = 0.9$ $\mu_{\rm B}$/Ce for $2x = 0.16$ have been proved by neutron scattering experiments [109]. The enhancement of $\mu_{\rm AF}$ results in the increase in both the magnetic entropy $S_{\rm m}(T_{\rm N})$ and $M(T = 2$ K, $B = 14$ T). Note that the decrease in $T_{\rm N}$, however, is only 10% from 28.5 K for $2x = 0$ to 26.5 K for $2x = 0.06$. The opposite changes between $\mu_{\rm AF}$ and $T_{\rm N}$ with respect to $2x$ suggest that the intersite AFM interaction between Ce moments depends on neither the magnitude nor direction of $\mu_{\rm AF}$ with respect to the crystal axis. Similar reorientation of AFM ordered moments has been observed in $CeRu_2Al_{10}$ when Rh is partially substituted for Ru at 5% [103, 104, 105]. Thereby, the decrease in $T_{\rm N}$ is also 10% from 27.0 K for $2x = 0$ to 24.0 K for $2x = 0.1$. These facts indicate that the reorientations of magnetic moments is induced by the doping of $4d/5d$ electrons into the gapped state of the mother compounds.

Secondly, let us consider the relation between the hybridization gap, the DOS at $E_{\rm F}$, and the AFM order. Figure 4.15 displays the variations of the thermal activation energy Δ in $\rho(T)$, $T_{\rm S}$, $T_{\rm N}$, and γ per Ce mol as functions of doping amounts z, $2y$, and $2x$ for the three systems. The characteristic temperature $T_{\rm S}$ is defined by the bend in $S_{\rm b}(T)$. For each system, the suppression of $T_{\rm N}$ is well correlated with the increase in the γ value.

The degrees of changes for the $5d$-hole doped system are stronger than those for the $4f$-hole doped system. This contrasting response reveals that the gapped electronic state in $CeOs_2Al_{10}$ is much weakly affected by $4f$-hole doping compared with $5d$-hole doping. For the three systems, the common anticorrelation between T_N and γ suggests that the development of in-gap states at E_F destroys the AFM order. In fact, $\rho(T)$ exhibits the metallic behavior at low temperatures in the regions $z \geq 0.24$, $2y \geq 0.06$, and $2x \geq 0.3$, where the AFM orders are fading. Furthermore, we find the decreases in T_N and T_S follow that of Δ in the three systems although the $4f/5d$-hole and $5d$-electron doping change the c-f hybridization strength in very different ways. Therefore, it is suggested that the presence of hybridization gap is necessary for the unusual AFM order. However, for the sample with $z = 0.2$ and $2x = 0.3$, C/Ts exhibit weak anomalies at 11.6 and 7.0 K, respectively, although $\rho(T)$s no longer show the thermal activation-type behavior. The metallic behavior in the $\rho(T)$ can be attribute to the charge transport of quasiparticles in the residual DOS at E_F ($= N(E_F)$) within the hybridization gap. Moreover, in the existence of hybridization gap and AFM order, the bend in $S(T)$ at T_S is found only along the b axis. It is not clear yet why S_b decrease above T_N .

In the break-junction tunneling spectra, the peaks at the gap edge and the cusps in the zero-bias conductance ($= dI/dV(V = 0)$) are expected to provide more direct information of the temperature dependences of the gap structures and $N(E_F)$ [46, 47, 48, 49, 61]. In order to understand the relation between the unusual AFM order, the hybridization gap Δ, and $N(E_F)$, we have performed the break-junction tunneling spectroscopic study of CeT_2Al_{10} (T = Fe, Ru, and Os) and La-, Re-, and Ir-substituted $CeOs_2Al_{10}$.

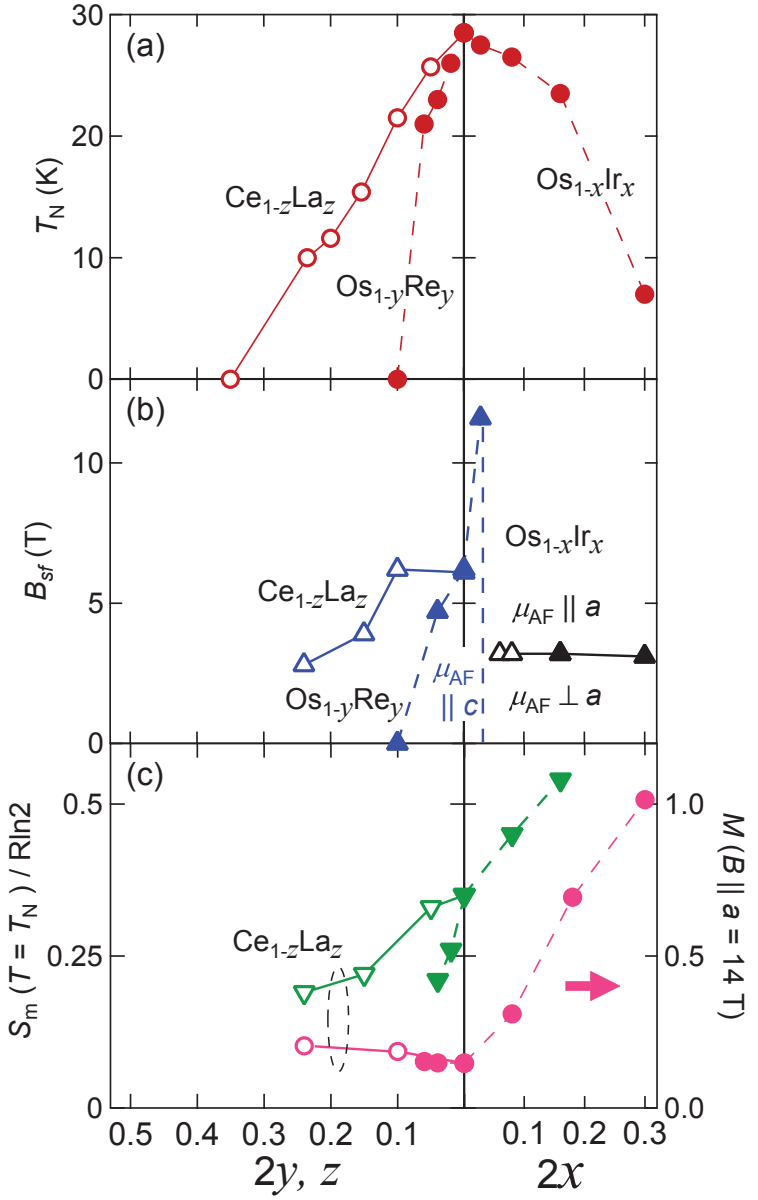

Figure 4.14: (a) Néel temperature $T_{\rm N}$, (b) spin-flop field $B_{\rm sf}$ in the isothermal magnetization curve $M(B)$, and (c) magnetic entropy $S_{\rm m}$ at $T_{\rm N}$, and magnetization $M(B \parallel a = 14$ T) at 2 K as functions of z, $2y$, and $2x$ in $Ce_{1-z}La_zOs_2Al_{10}$, $Ce(Os_{1-y}Re_y)_2Al_{10}$, and $Ce(Os_{1-x}Ir_x)_2Al_{10}$, respectively. Closed triangles in (b) denote the values of $B_{\rm sf}$ at the metamagnetic increase in $M(B)$ in Fig. 4.5, while open triangles denote the values of $B_{\rm sf}$ at the maximum in dM/dB.

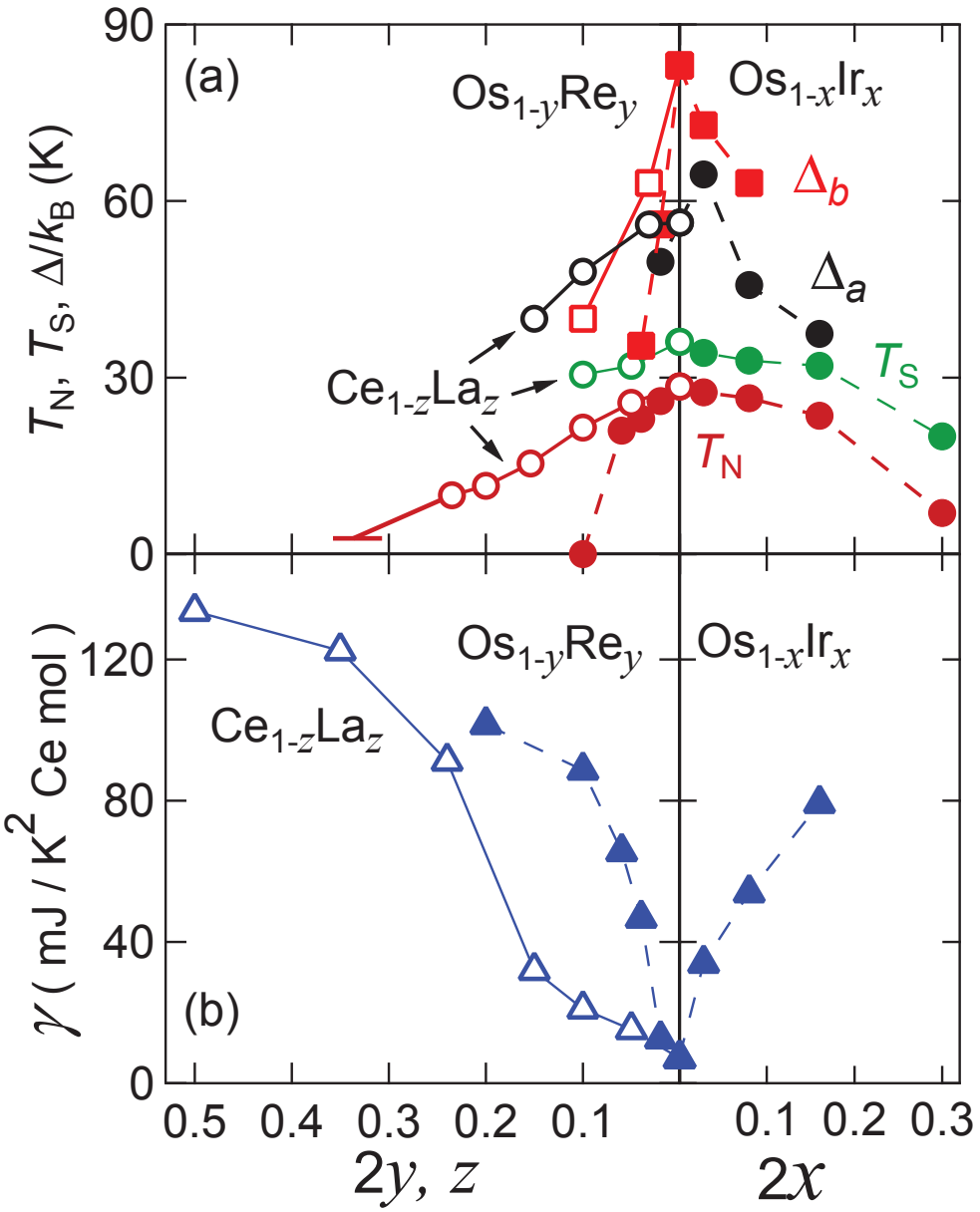

Figure 4.15: (a) Thermal activation energy Δ_a and Δ_b in the resistivity ρ, temperature T_S at the bends in the thermopower S_b, and Néel temperature T_N, and (b) γ value per Ce mol of the specific heat C/T as functions of z, $2y$, and $2x$ in $Ce_{1-z}La_zOs_2Al_{10}$, $Ce(Os_{1-y}Re_y)_2Al_{10}$, and $Ce(Os_{1-x}Ir_x)_2Al_{10}$, respectively.

4.2 Break-junction tunneling spectroscopy on CeT_2Al_{10} (T = Fe, Ru, and Os) and substituted $CeOs_2Al_{10}$

4.2.1 Characteristic features of tunneling spectra dI/dV in CeT_2Al_{10} (T = Fe, Ru, and Os)

Anisotropy of the spectra

Typical spectra of differential conductance dI/dV measured with current directions along the orthorhombic principal axes for CeT_2Al_{10} (T = Fe, Ru, and Os) are shown in Figs. 4.16 and 4.17. The spectra are shifted vertically for clarity. We realized there are no significant differences in the spectra with respect to the current directions. The crack of the sample was made just underneath the groove cut perpendicular to the long direction. However, it is not certain whether the tunneling in the local area occurs perpendicular to the bulk crack when the surface is reconstructed. In addition, the electrons tunneling through an atomic scale area may lose the information of the wave-vector due to the uncertainty principle [126].

Reproducibility of the spectra

Figure 4.18(a) shows the dI/dV spectra of $CeOs_2Al_{10}$ at 4.4 K for various junctions with resistances R_J ranging from 22 to 738 Ω. Here, the magnitude of R_J was obtained as the inverse of ZBC. For each measurement, the value of R_J is more than 1000 times compared with the sample resistance before breaking. We see similar features of three gaps, V_1, V_{AF}, and V_2 in all spectra. Figure 4.18(b) summarizes the values of peak-to-peak voltages V^{P-P} of the three gaps in 30 spectra including the data of Fig. 4.18(a). We notice that the gap values are essentially independent of R_J in a wide range of 9 – 800 Ω. Also for T = Fe and T = Ru, we confirmed that all gap structures and the widths V^{P-P} for each compound hardly depend on the magnitude of R_J. These observations support that the tunneling regime dominates in the junctions although the real nature of the interface remains unknown. The largest value of R_J is still less than 10 kΩ that is expected for a single-step elastic tunneling in scanning tunneling spectroscopy. It is likely that the large effective area of our break junction give rise to the small values of R_J as observed in other

Kondo semiconductors [46, 47, 48, 49].

Comparison of the junction resistance with the bulk resistivity

We show the temperature dependence of $R_{\rm J}$ normalized by the value at 4.4 K together with that of the bulk resistivity $\rho(T)$ for CeT_2Al_{10} (T = Ru and Os) in Fig. 4.19. If the observed temperature dependence of ZBC were due to the change in the resistance of a weak link at the junction, $R_{\rm J}$ would exhibit the similar temperature dependence of the bulk resistivity. Whereas $R_{\rm J}$ of T = Ru remains constant below $T_{\rm N}$, $\rho(T)$ exhibits a peak and sharply decreases on cooling below $T_{\rm N}$. For T = Os, the increase in $R_{\rm J}$ below $T_{\rm N}$ is much weaker than that of $\rho(T)$.

Then, we compare $\rho(T)$ and the differential resistance dV/dI as a function of bias voltage V in Figs. 4.20 and 4.21 for T = Ru and Os, respectively. The presence of a local minimum at around 80 and 55 meV, respectively, mimics the peak in the bulk resistivity at around 25 K. However, dV/dI for T = Ru continues to increase with decreasing V, in contrast with the significant decrease in the resistivity on cooling. Moreover, the presence of dip in dV/dI at high energy region does not correspond to the monotonic behavior in the resistivity. These results deny the possibility of the weak link but support the tunneling nature of our break junction.

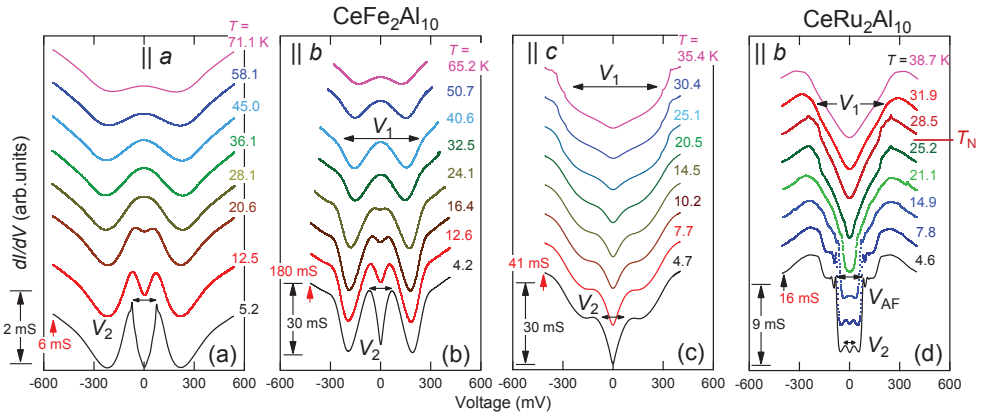

Figure 4.16: Temperature variations of the differential conductance dI/dV versus the bias voltage V for $CeFe_2Al_{10}$ measured for break junctions with electrical currents along the (a) a, (b) b, and (c) c axes, and for (d) $CeRu_2Al_{10}$ with current along the b axis, respectively. Curves are shifted vertically for clarity. The widths between the shoulders, between the peaks, and between the inner peaks of the spectra are denoted as V_1, $V_{\rm AF}$, and V_2, respectively. The widths V_1, $V_{\rm AF}$, and V_2 are shown by horizontal arrows.

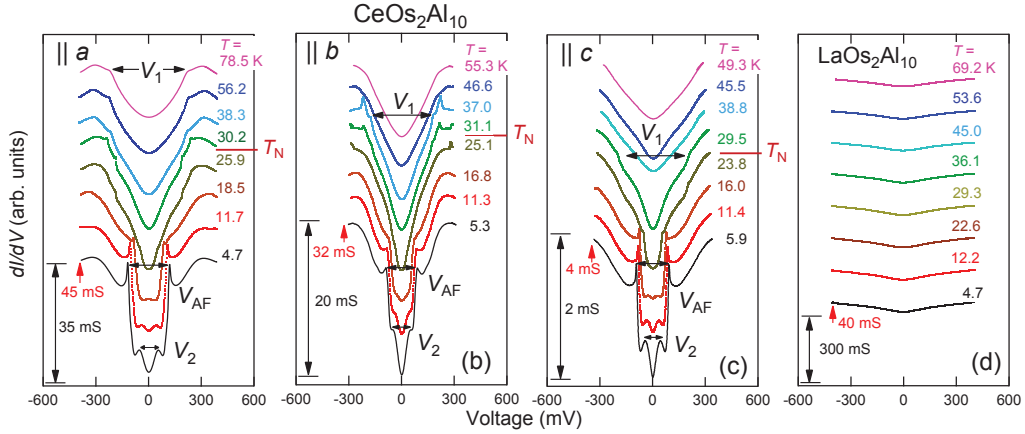

Figure 4.17: (a)–(c) Temperature variations of the differential conductance dI/dV vs the bias voltage V for $CeOs_2Al_{10}$ measured for break junctions with currents along the orthorhombic principal axes, and (d) for the metallic reference $LaOs_2Al_{10}$, respectively. Curves are shifted vertically for clarity.

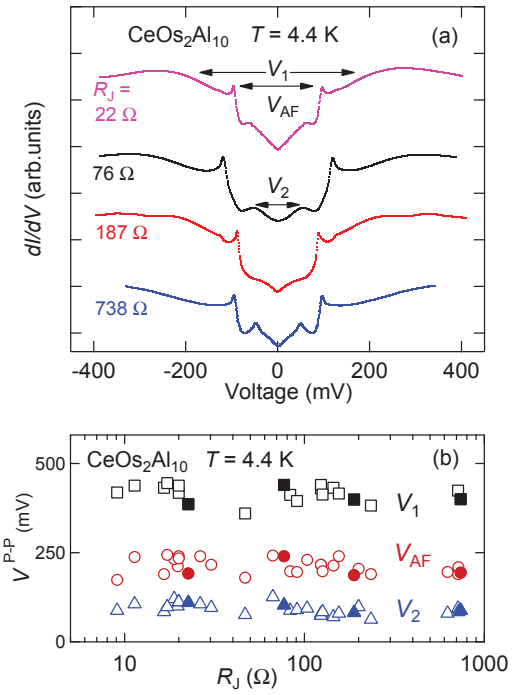

Figure 4.18: (a) Differential conductance spectra dI/dV vs bias voltage V at 4.4 K for $CeOs_2Al_{10}$ break-junctions with various resistances R_J, which is estimated as the inverse of the zero-bias conductance. (b) Peak-to-peak gap widths V_1, V_2, and V_{AF} for CeT_2Al_{10} break junctions as a function of the junction resistance R_J in a wide range of 9 – 800 Ω.

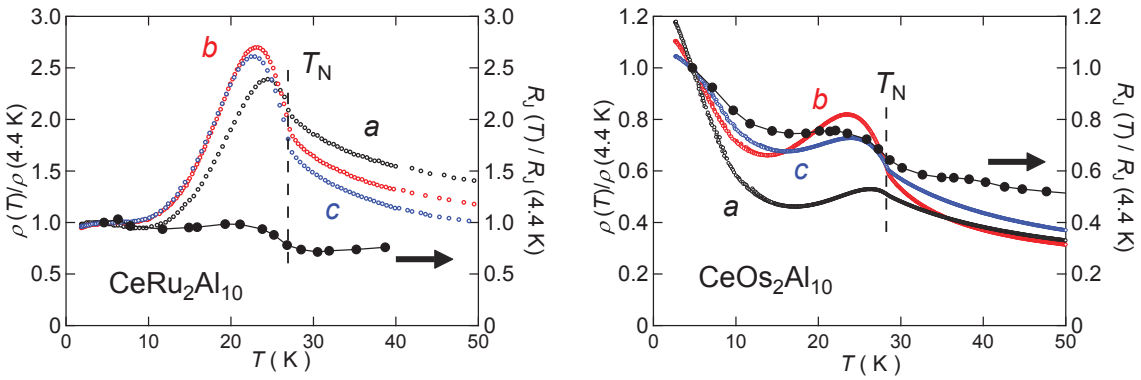

Figure 4.19: Temperature dependences of electrical resistivity $\rho(T)$ along the three principal axes and junction resistance R_J for CeT_2Al_{10} (T = Ru and Os) normalized by the value at 4.4 K.

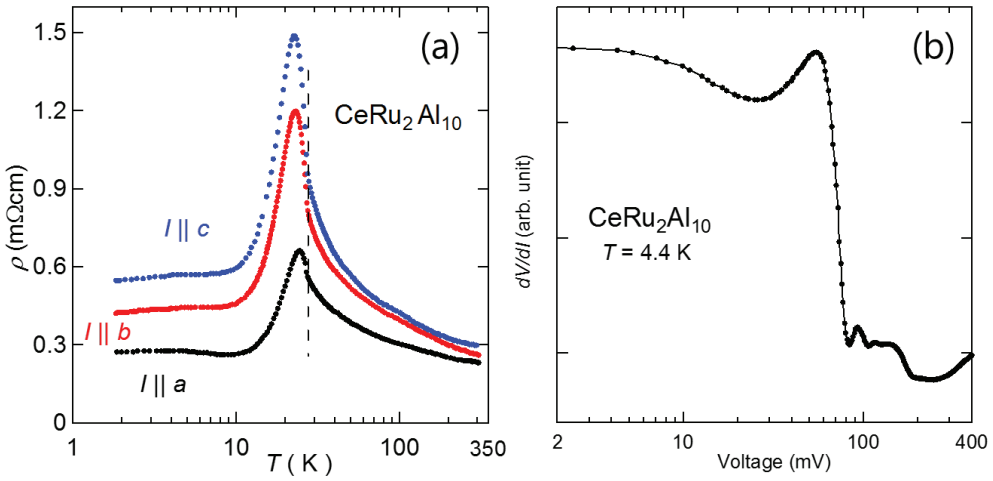

Figure 4.20: Temperature dependence of (a) electrical resistivity $\rho(T)$ and (b) bias voltage dependence of the differential resistance dV/dI at 4.4 K for $CeRu_2Al_{10}$.

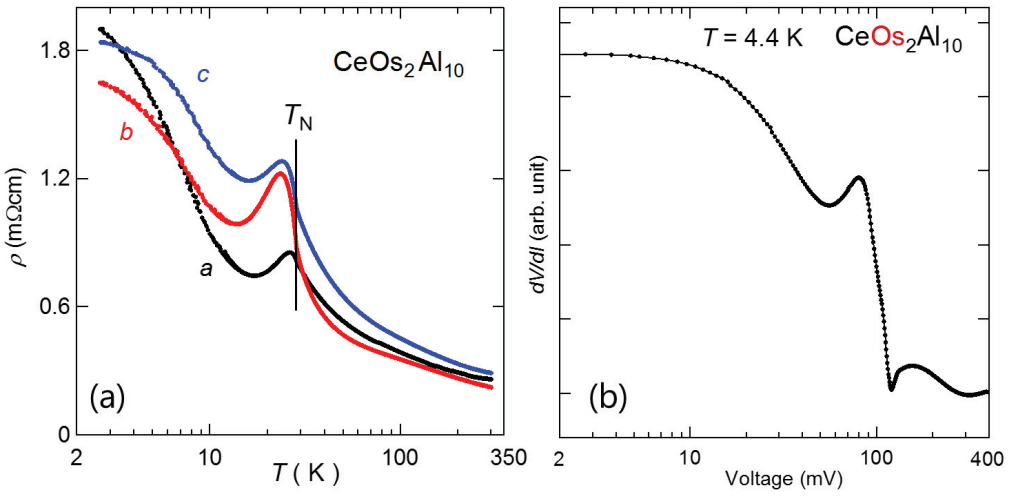

Figure 4.21: Temperature dependence of (a) electrical resistivity $\rho(T)$ and (b) bias voltage dependence of the differential resistance dV/dI at 4.4 K for $CeOs_2Al_{10}$.

4.2.2 Hybridization gaps and antiferromagnetic gap in CeT_2Al_{10} (T = Fe, Ru, and Os)

$CeFe_2Al_{10}$

Let us focus on the temperature dependence of the dI/dV spectra for T = Fe for $I \parallel a$, $I \parallel b$, and $I \parallel c$, respectively, shown in Figs. 4.16 (a)–(c). At temperature above 30 K, there are a pair of shoulders at ±300 mV, providing the shoulder-to-shoulder voltage V_1 = 600 mV. For $T < 30$ K, distinct peaks appear at ±75 mV, from which V_2 is given as 150 mV. For $I \parallel a$, an upward peak at $V = 0$ changes into a downward peak on cooling below 20 K, with the concomitant development of the peaks at $V_2/2$. On cooling, the structures at $V_1/2$ and $V_2/2$ become sharper.

$CeRu_2Al_{10}$

Because no significant anisotropy was observed in the tunneling spectra either in $CeFe_2Al_{10}$ or $CeOs_2Al_{10}$, we have measured the tunneling spectra for $CeRu_2Al_{10}$ with sample only along the b axis. The temperature variations are represented in Fig. 4.16 (d). The spectrum at 38.7 K is characterized by a V-shaped structure with a pair of shoulders at $V_1/2 = \pm 190$ mV. On cooling, the shoulders at $V_1/2$ become clearer. Below T_N = 27.0 K, other shoulders develop at V_{AF} and change into peaks. At $T < 15$ K, additional structures develop at $V_2/2$, changing into peaks. Let us focus on the shape in the vicinity of $V = 0$. The U-shaped form at 21.1 K transforms into an upward peak at 14.9 K. When the gap V_2 develops, a V-shaped structure appears at $V = 0$. Unlike in $CeFe_2Al_{10}$ with similar gap of V_2, the resistivity $\rho(T)$ for $CeRu_2Al_{10}$ does not increase at low temperature, whose reason will be discussed later.

$CeOs_2Al_{10}$ and $LaOs_2Al_{10}$

The temperature variations of dI/dV spectra for $CeOs_2Al_{10}$ are shown in Fig. 4.17(a)–(c). The spectrum for $I \parallel a$ at 78.5 K displays a V-shaped structure with a pair of shoulders at ±220 mV which are denoted as V_1. On cooling below T_N, another pair of shoulders appear and develop into peaks, which are denoted as the antiferromagnetic gap V_{AF}. When the gap edge of V_{AF} becomes sharper on cooling, the tail extends to the high

bias voltage, making the V_1 structure unobvious. On further cooling below 16 K, the third structure manifests itself as peaks inside the $V_{\rm AF}$, which are denoted as V_2. The V-shaped spectra with the gap V_2 are commonly observed in the three systems of CeT_2Al$_{10}$ (T = Fe, Ru, and Os) at low temperatures. For comparison, we show the tunneling spectra of the normal metal LaOs$_2$Al$_{10}$ without $4f$ electrons in Fig. 4.17 (d). The flat V-shaped spectrum reflects the tunneling probability in the metallic state which increases with the increase of the bias voltage V (as described in Fig. 3.15). The temperature independent spectrum is in contrast to those of CeT_2Al$_{10}$ (T = Fe, Ru, and Os), confirming that $4f$ electrons are indispensable for the gap opening.

Comparison of the tunneling gap with the optical gap and spin gap

The gaps V_1, $V_{\rm AF}$, and V_2 for CeT_2Al$_{10}$ (T = Fe, Ru and Os) were also observed by the photoemission spectroscopy and optical conductivity measurements [94, 95, 96]. The gap widths are listed in table 4.1. For the three systems, the tunneling gaps are 4–7 times larger than the optical gaps. Furthermore, the AFM gaps $\Delta_{\rm AF}$ for T = Ru and Os observed by break-junction experiments are 40 and 60 mV, which are also several times larger than the spin gaps of 8 and 11 meV observed by inelastic neutron scattering [83, 84]. These discrepancies in the energy scale remain unexplained and might be related to the broken symmetry at the surface of Kondo semiconductors.

Table 4.1: Gap widths $2\Delta_1$, $2\Delta_{\rm AF}$, and $2\Delta_2$ for CeT_2Al$_{10}$ observed by the break-junction tunneling, photoemission spectroscopy, and optical conductivity $\sigma(\omega)$ [94, 95, 96, 113, 114].

	BJTS [113, 114]			Optical $\sigma(E)$ [95, 96]		Photoemission [94]		
CeT_2Al$_{10}$	$V_1/2$ (meV)	$V_{\rm AF}/2$ (meV)	$V_2/2$ (meV)	$2\Delta_1$ (meV)	$2\Delta_{\rm CDW}$ (meV)	$2\Delta_1$ (meV)	$2\Delta_{\rm AF}$ (meV)	$2\Delta_2$ (meV)
Fe	300	–	75	55	–	60	–	10
Ru	190	80	25	40	20	40	20	–
Os	220	120	50	45	20	50	20	–

Discussion

Figure 4.22 (a) represents the typical spectra of dI/dV versus bias voltage V taken at 4.4 K for CeT_2Al$_{10}$ (T = Fe, Ru, and Os). The spectra are normalized by the values in the high-bias range at $V = -400$ mV outside the gap region. This normalization was done because the absolute value of dI/dV depends on $R_{\rm J}$, which is determined by the area and the thickness of insulating barrier d as expressed by Eq. 3.27. For CeFe$_2$Al$_{10}$ without exhibiting AFM transition, there are two gaps V_1 and V_2, while there is another gap $V_{\rm AF}$ in CeT_2Al$_{10}$ (T = Ru and Os). In the three spectra, the normalized zero-bias conductance (NZBC) at $V = 0$ is finite, ranging from 0.3 for T = Os to 0.7 for T = Fe. We note that [NZBC]$^{1/2}$ is proportional to the DOS at the $E_{\rm F}$ [46, 47]. Actually, the increasing trend in [NZBC]$^{1/2}$ on going from T = Os to T = Ru, and to T = Fe is in good agreement with the trend in the γ value in C/T as described in Fig. 1.36 (a). In the spectra for T = Ru, the shoulders at $\pm$180 mV and peak structures at $\pm$80, $\pm$25 mV are denoted as V_1, $V_{\rm AF}$, and V_2, respectively. The overall spectrum with three gaps for T = Os is similar to that for T = Ru. The gap width of $V_{\rm AF}$ = 160 mV for T = Ru is smaller than $V_{\rm AF}$ = 240 mV for T = Os, which is consistent with the lower $T_{\rm N}$ = 27.0 than 28.5 K for T = Os. Except for $V_{\rm AF}$, there are no significant differences in the gap structures among the three systems.

From the temperature dependent spectra in Figs. 4.16 and 4.17, we obtained the temperature dependences of the gap widths and [NZBC]$^{1/2}$ as shown in Fig. 4.22 (b, c). Upon cooling CeFe$_2$Al$_{10}$, V_1 gradually increases and then V_2 develops below 30 K, which is associated with the decrease in [NZBC]$^{1/2}$. On the other hand, V_1's for T = Ru and Os decrease rather sharply at $T < 28$ and 36 K, respectively, in concomitant with the decrease in [NZBC]$^{1/2}$. We define the characteristic temperature T^* as the onset of the decrease in the [NZBC]$^{1/2}$, as marked by the arrows in Fig. 4.22 (c). We recall that distinct anomalies at $T \leq T^*$ have been detected by experimental techniques which are sensitive to the temperature dependence of $N(E_{\rm F})$ [85, 86, 112]. When the system with T = Os is cooled below T^*, for example, clear decreases were found in both the thermopower along the b axis in Fig. 4.7 [112] and the nuclear spin-lattice relaxation rate of ^{27}Al nuclear quadruple resonance [85, 86].

Let us turn our attention to the gaps V_1 and V_2. In Fig. 4.23, we plot the data of $V_1/2$

and $V_2/2$ for CeT_2Al_{10} (T = Fe, Ru, and Os) together with those reported for orthorhombic Kondo semiconductors CeNiSn, CeRhSb [46, 47], and CeRhAs [48] as a function of T_K ($= 3 \times T_\chi$). The linear relations between V_i (i = 1, 2) and T_K indicate that these gaps are scaled by T_K. It should be mentioned that the data for the cubic system $Ce_3Bi_4Pt_3$ ($V_2/2$ = 85 mV and T_K = 240 K) [129] fall down on the line of V_2 in Fig. 4.23. The lack of data of $V_1/2$ for CeNiSn and CeRhSb may be attributed to the fact that the highest bias was lower than 100 mV in previous BJTS measurements. Moreover, the ratio V_1/V_2 at 4.4 K equals to 4 for these compounds. This value and the scaling of the two gaps with T_K are consistent with the calculation within the c-f hybridization gap model assuming the crystal-field ground state of $|J_z\rangle = |\pm 3/2\rangle$, where J_z is the z component of the total angular momentum $J = 5/2$ [38, 50, 51, 52]. Indeed, the analysis of anisotropic magnetic susceptibility and x-ray absorption spectra indicated that the crystal-field ground state of the $4f$ state in the systems with T = Ru and Os is dominated by $|J_z\rangle = |\pm 3/2\rangle$ when the c axis is taken as the quantization axis [80]. The consistency gives another evidence that V_1 and V_2 are c-f hybridization gaps. In addition, it is noteworthy that the scaling is not violated by the presence of AFM order occurring in the systems with T = Ru and Os.

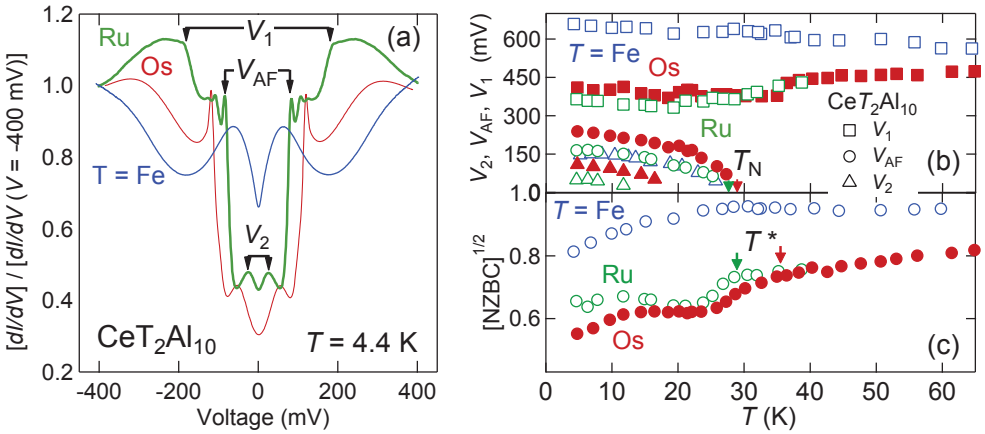

Figure 4.22: (a) Differential conductances dI/dV versus the bias voltage V normalized by the value at $V = -400$ mV for CeT_2Al_{10} (T = Fe, Ru, and Os) measured at 4.4 K. The gap widths V_1, V_{AF}, and V_2 denote the widths between the shoulders, between the peaks, and between inner peaks of the spectra, respectively. The arrows indicate the widths V_1, V_{AF}, and V_2 for the spectrum of T = Ru. The temperature dependences of (b) gap widths and (c) square root of the normalized zero-bias conductance, $[NZBC]^{1/2}$ for CeT_2Al_{10} (T = Fe, Ru, and Os). Here, $[NZBC]^{1/2}$ is the value of square root of normalized tunneling conductance at $V = 0$, which is proportional to the DOS at the Fermi energy E_F, $N(E_F)$.

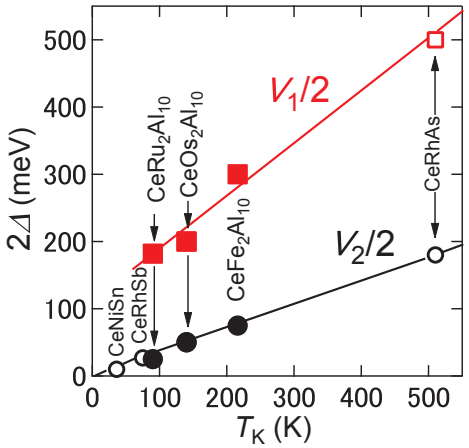

Figure 4.23: Hybridization gap widths $V_1/2$ and $V_2/2$ as a function of T_K. The V_1 and V_2 are measured by the BJTS on the orthorhombic Kondo semiconductors [46, 47, 48].

4.2.3 Doping effects on the hybridization gaps and antiferromagnetic gap in $CeOs_2Al_{10}$

For CeT_2Al_{10} (T = Fe and Os), we have measured the differential spectra with currents applied along the three principal axes, as described above. However, no significant differences were observed in gap widths with respect to the current direction. In addition, it was hard to grow the substituted single crystals whose size are large enough to be used for BJTS measurements, 2.5 mm in length. On these conditions, we used polycrystalline samples with substituted elements.

$4f$-hole doped system $Ce_{1-z}La_zOs_2Al_{10}$

Figure 4.24 shows the temperature dependences of dI/dV spectra for the $4f$-hole doped system $Ce_{1-z}La_zOs_2Al_{10}$ ($z \leq 0.35$). For $z = 0$, the V-shaped spectrum has shoulders at V_1 and the structure of $V_{\rm AF}$ which appears below $T_{\rm N}$. On further cooling below 16 K, the third structure V_2 develops inside the gap $V_{\rm AF}$. The three gap structures are broadened in the spectra for $z = 0.05$. The shoulders at V_1 become unclear on cooling, and shoulders of $V_{\rm AF}$ and V_2 appear at $\pm$80 and $\pm$25 mV, respectively. For $z = 0.2$, shoulders at V_1 and $V_{\rm AF}$ are still noticeable, and a weak anomaly of $V_{\rm AF}$ can be noticed even at around 30 K, far above $T_{\rm N} = 11.6$ K. It should be recalled that the jump of $\Delta C_{\rm m}/T$ at $T_{\rm N}$ is only 10% of the value for $z = 0$ (Fig. 4.10 (b)), probably due to the inhomogeneous environment around the Ce atoms. Note that one BJTS spectrum is an ensemble of tunneling processes at various junctions. If some junctions of microscopic area have higher $T_{\rm N}$ than the average $T_{\rm N}$, it may cause the $V_{\rm AF}$ structure even above the average $T_{\rm N}$ determined by the specific heat. For $z = 0.35$, C/T has no anomaly of AFM order and $\rho(T)$ shows a metallic behavior, whereas the dI/dV spectrum has faint shoulders at V_1. The result implies that the opening of V_1 does not reflect in the thermal activation-type behavior in $\rho(T)$ (see Fig. 4.6). In any case, a V-shaped structure at zero-bias is observed in the whole range $z \leq 0.35$. This V-shaped structure contradicts with an upward cusp obtained by the calculation for randomly distributed Kondo holes in the Ce sublattice on the basis of the PAM [62]. This disagreement suggests that the real role of the substituted La in $CeOs_2Al_{10}$ is to disturb the coherency of the hybridized

band.

5d-hole doped system $\mathbf{Ce(Os_{1-y}Re_y)_2Al_{10}}$

In Fig. 4.25, we show the temperature dependences of the dI/dV spectra for the 5d-hole doped system $Ce(Os_{1-y}Re_y)_2Al_{10}$. At a small doping level of $2y = 0.04$, the spectrum at 37.0 K displays a pair of shoulders at $V_1/2$. The shoulder changes to a peak at $T < 35$ K, and transform into a shoulder again below 30 K. On cooling below 27 K, another pair of shoulders manifest themselves at ± 90 mV and an upward cusp develops at zero bias. The cusp becomes sharper for $2y = 0.2$, in which the structures of V_1 and V_{AF} no longer exist. Because such development of the cusp at $V = 0$ is a characteristic of a metallic heavy fermion state [131], it is confirmed that the 4f state in $CeOs_2Al_{10}$ becomes more itinerant by the doping of 5d holes. These observations are consistent with the calculated gap structures in the DOS of the orthorhombic KSs on the basis of the PAM by taking account of weak dispersion of the 4f-band [63]. According to the theory, hole doping lowers E_F toward the top of the lower c-f hybridization band, making hole pockets in the vicinity of the E_F. Thereby, the semiconducting behavior of $\rho(T)$ changes to the metallic one for the valence fluctuating system as shown in Fig. 4.6. With increasing $2y$, we observed the decrease in the magnitude of V_1 in spite of the increase in T_K. This may be attributed to the growth of the cusp at zero bias.

5d-electron doped system $Ce(Os_{1-x}Ir_x)_2Al_{10}$

Figure 4.26 shows the temperature dependent tunneling spectra of the 5d-electron doped samples $Ce(Os_{1-x}Ir_x)_2Al_{10}$ ($x \leq 0.3$). For $2x = 0.08$, the pair of shoulders of V_1 change to peaks on cooling below 50 K, and the inner shoulders of V_{AF} appear below 25 K. At $T < 18$ K, an upward cusp develops at $V = 0$. For $2x = 0.3$, the dI/dV still exhibits the gap structure of V_1 although the thermal activation behavior in $\rho(T)$ is lost above T_N (Fig. 4.6). At $T < 20$ K, broad shoulders appearing inside the gap V_1 are assigned to V_{AF} because they become noticeable below T_N. It is remarkable that the shape at around zero bias changes from a V-shaped form for $2x = 0$, an upward cusp for $2x = 0.08$, then again to the V-shaped form for $2x = 0.3$. Theoretical studies of the electron doping effect on Kondo semiconductors showed that impurity bands appear at the E_F inside the gaps [64, 65]. This effect is consistent with the observed change in dI/dV at zero bias for the samples with $2x < 0.3$. For $2x = 0.3$, however, the temperature dependence of dI/dV with a V-shaped structure at $V = 0$ resembles that of a heavy fermion AFM metal $CeRh_2Si_2$ [130]. These facts indicate that the doping of 5d electrons in $CeOs_2Al_{10}$ changes the ground state from a KS for $2x = 0$ to a doped KS in the range $0 < 2x < 0.3$, and to a heavy fermion AFM metal for $2x = 0.3$. The suppression of V_1 with increasing x is ascribed to the weakened c-f exchange interaction. The magnitude of V_{AF} also decreases with x, whereas the ordered magnetic moments are reoriented and elongated from $\mu_{AF}//c = 0.3\ \mu_B$/Ce for $2x = 0$ to $\mu_{AF}//a = 0.9\ \mu_B$/Ce for $2x = 0.16$ [109]. This fact indicates that the magnitude of V_{AF} does not depend on either the magnitude and the direction of μ_{AF}.

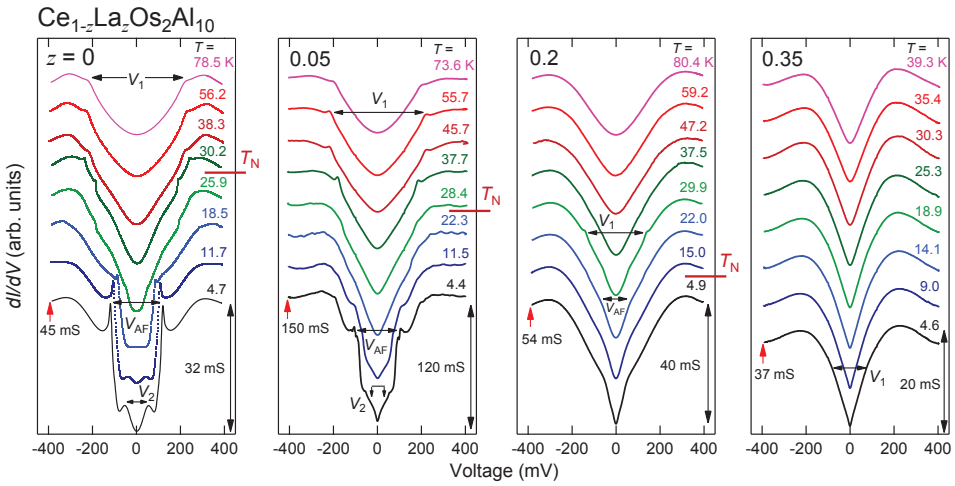

Figure 4.24: Temperature variations of the dI/dV spectra for the $4f$-hole doped system $Ce_{1-z}La_zOs_2Al_{10}$ for $z = 0$, 0.05, 0.2, and 0.35 with $T_N = 28.5$, 25.5, 11.6, and < 2.0 K, respectively. The gap widths V_1, V_{AF}, and V_2 are shown by horizontal arrows. Curves are vertically shifted for clarity.

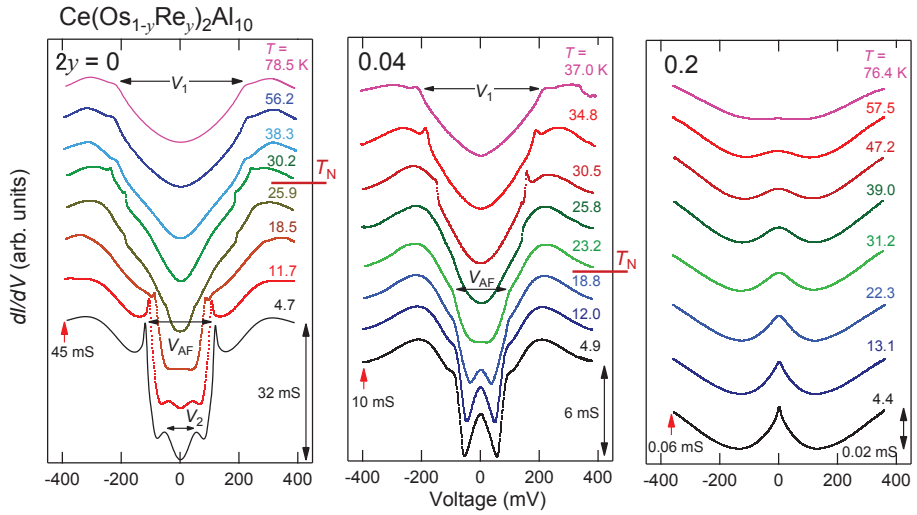

Figure 4.25: Temperature variations of the dI/dV spectra for the $5d$-hole doped system $Ce(Os_{1-y}Re_y)_2Al_{10}$ for $2y = 0$, 0.04 and 0.2 with $T_N = 28.5, 23.0, < 2.0$ K, respectively. The gap widths V_1, V_{AF}, and V_2 are shown by horizontal arrows. Curves are offset vertically for clarity.

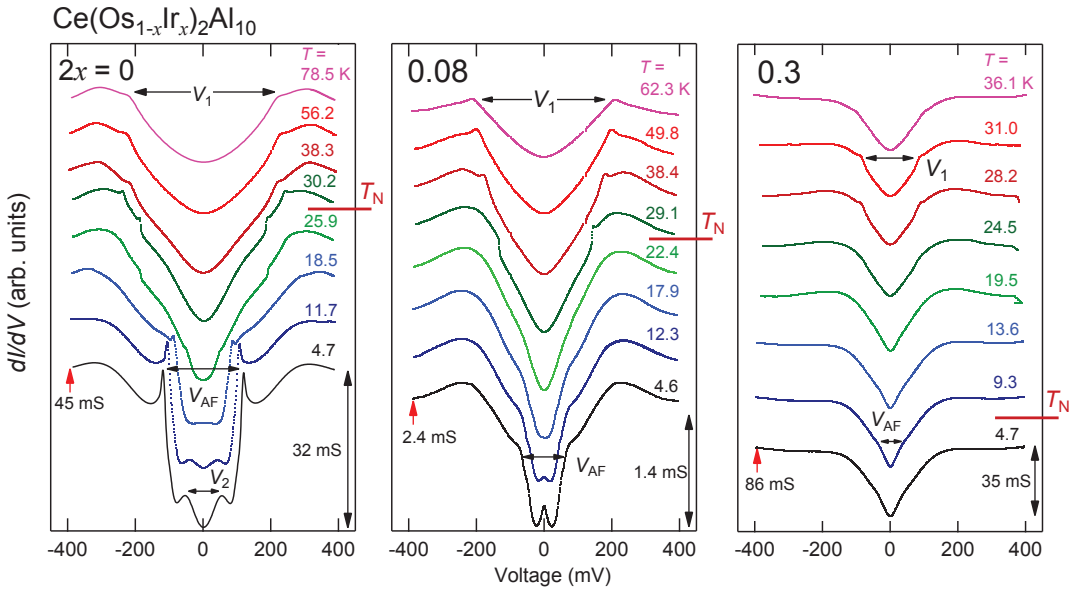

Figure 4.26: Temperature variations of the dI/dV spectra of the 5d-electron doped system $Ce(Os_{1-x}Ir_x)_2Al_{10}$ for $2x = 0$, 0.08 and 0.3 with $T_N = 28.5$, 26.5, and 7.0 K, respectively. The gap widths V_1, V_{AF}, and V_2 are shown by horizontal arrows. Curves are offset vertically for clarity.

Discussion

In order to gain insights into the relation between the AFM order and gap structures, we summarize in Fig. 4.27 the selected data sets of gap widths V_1 and $V_{\rm AF}$ in (a, c) and $[\rm NZBC]^{1/2}$ in (b, d) for three doped systems. The lightly and heavily doped ranges correspond to (a, b) and (c, d), respectively. As described above, the $4f/5d$-hole doping and $5d$-electron doping change the dI/dV spectrum in largely different ways. It is, however, common that V_1's decrease on cooling at around T^* ($> T_{\rm N}$) in the doping region where V_1 and $V_{\rm AF}$ coexist. In the heavily doped region, $z \leq 0.2$, the decreasing rate of V_1 with temperature is weakened. For $z = 0$, V_1 increases slightly when $V_{\rm AF}$ develops below $T_{\rm N}$. On the contrary, $V_{\rm AF}$ in doped samples seems to appear suddenly at around $T^* > T_{\rm N}$, and stays constant with decreasing temperature. As mentioned above, this may arise from the distribution of the local environment of the Ce atoms in doped samples.

We discuss the temperature variations of $[\rm NZBC]^{1/2}$, which is known to be proportional to $N(E_{\rm F})$. As shown in Fig. 4.27 (b), $[\rm NZBC]^{1/2}$ for the non-doped sample gradually decreases below 60 K and bends at $T^* = 36$ K. At the temperature T^*, the thermopower S only along b axis also decreases. For $z = 0.05$ and 0.2, similar bending occurs at $T^* = 35$ and 32 K, respectively, while no bend is seen for $z = 0.35$. For $2y = 0.04$, the initial decrease in $[\rm NZBC]^{1/2}$ turns to an increase below 27 K, which is the result of the development of zero-bias cusp. This upturn in $[\rm NZBC]^{1/2}$ masks the possible downward bend in the region from 40 to 27 K, where V_1 gradually decreases. For $2y = 0.2$ with no AFM transition, $[\rm NZBC]^{1/2}$ increases monotonically on cooling. For $2x = 0.08$, $[\rm NZBC]^{1/2}$ bends at $T^* = 32$ K and then increases below 18 K. For $2x = 0.3$, a weak bend is noticeable at $T^* = 26$ K. These observations reveal that the significant decrease in $[\rm NZBC]^{1/2}$ below $T^*(> T_{\rm N})$ occurs only in the doping region where V_1 and $V_{\rm AF}$ coexist.

The key parameters obtained by the BJTS experiments are plotted in Fig. 4.28 as functions of $2x$, $2y$, and z. The upper and lower panels display, respectively, the variations of the gap widths V_1 and $V_{\rm AF}$, and those of T^*, $T_{\rm S}$, $T_{\rm N}$, and $[\rm NZBC]^{1/2}$ at 4.4 K as functions of $2x$, $2y$, and z. The $T_{\rm N}$ is suppressed and $[\rm NZBC]^{1/2}$ is increased with $2x$ and $2y$, whose variations are more drastic as a function of $2y$. We note that the asymmetric change in $[\rm NZBC]^{1/2}$ resembles the asymmetric increase in the γ value (Fig. 4.15). On the other hand, $[\rm NZBC]^{1/2}$ initially decreases by 15% as z increases from 0 to 0.05, and then increases

with further increasing z. This increase in $[\mathrm{NZBC}]^{1/2}$ with z is much slower compared with that with $2y$.

Now, we focus on the relation between V_1 and V_{AF}. In all doping cases, the values of V_1, V_{AF}, and T_{N} are suppressed with the increase of $2x$, $2y$, and z. The weaker suppression with z than with $2y$ implies that the gaps and $N(E_{\mathrm{F}})$ in $CeOs_2Al_{10}$ are much weakly affected by $4f$ hole doping compared with $5d$ hole doping. Moreover, V_1 and V_{AF} disappear as $2y$ is increased to 0.1. By contrast, the dI/dV spectrum for $z = 0.35$ has only V_1, whose magnitude is reduced to 1/3 of that for $z = 0$. In the absence of V_{AF} and T_{N} for $z = 0.35$, V_1 still exists. On the other hand, T^* exists in the region where both V_1 and V_{AF} are observed. These relations strongly suggest that the decrease in $N(E_{\mathrm{F}})$ below T^* is a precursor of the AFM transition. In fact, the decrease in $N(E_{\mathrm{F}})$ occurring above T_{N} is consistent with the opening of the charge excitation gap found by the optical conductivity measurements [95, 96]. As noted in the Introduction, the optical conductivity in the energy region below 20 meV decreases on cooling below T^*. At the same temperature, bends are also observed in the nuclear spin-lattice relaxation rate of ^{27}Al NQR as shown in Fig. 4.29. Moreover, the changes of T^* with z and $2x$ are in agreement with those of T_S, where $S_{\mathrm{b}}(T)$ bends as shown in Fig. 4.28. Therefore, the bend in S_{b} is the result of the decrease in $N(E_{\mathrm{F}})$ on cooling, probably associated with a topological change in the Fermi surface.

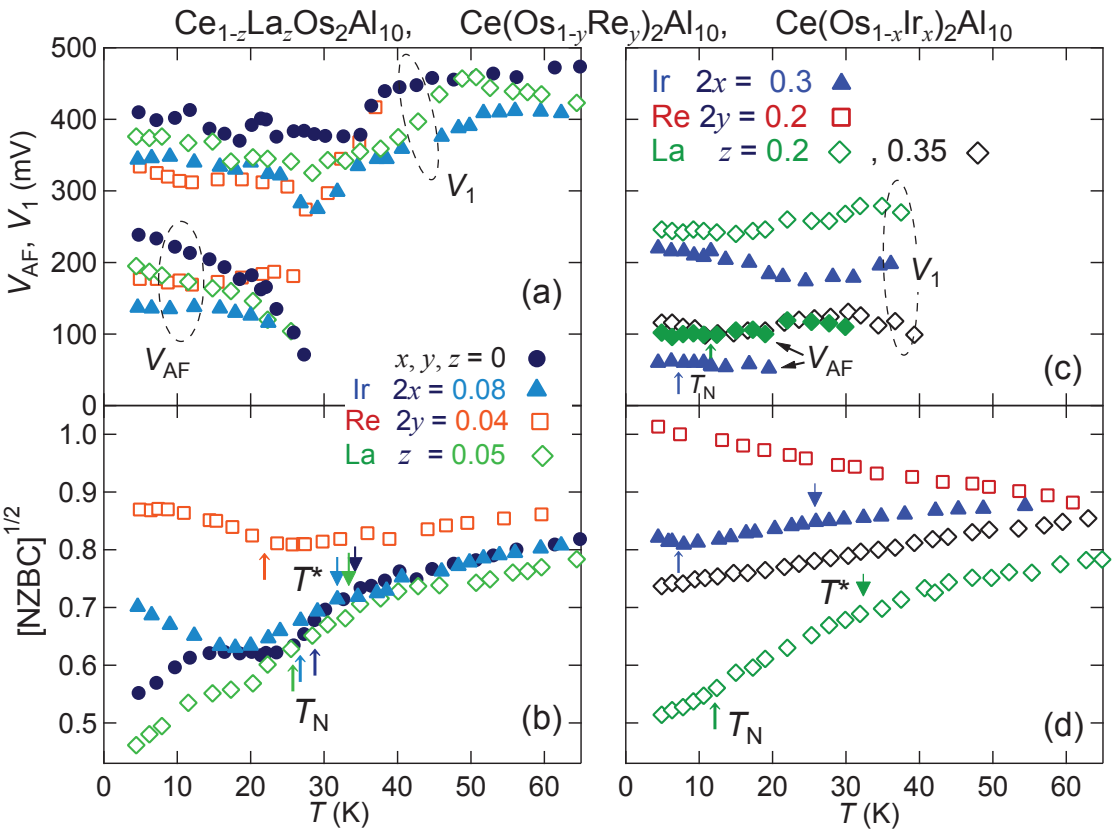

Figure 4.27: Temperature dependences of (a, c) gap widths V_1, $V_{\rm AF}$ and (b, d) $[\mathrm{NZBC}]^{1/2}$ for the substituted samples of $Ce_{1-z}La_zOs_2Al_{10}$, $Ce(Os_{1-y}Re_y)_2Al_{10}$, and $Ce(Os_{1-x}Ir_x)_2Al_{10}$. NZBC is the zero bias conductance $dI/dV(V = 0)$ normalized by the value at $V = -400$ mV. The $T_{\rm N}$'s are 28.5 K ($z, y, x = 0$), 26.5 K ($2x = 0.04$), 7.0 K($2x = 0.3$), 23 K($2y = 0.04$), 25.5 K ($z = 0.05$), 11.6 K ($z = 0.2$), and < 2 K ($2y = 0.2$, $z = 0.35$), respectively.

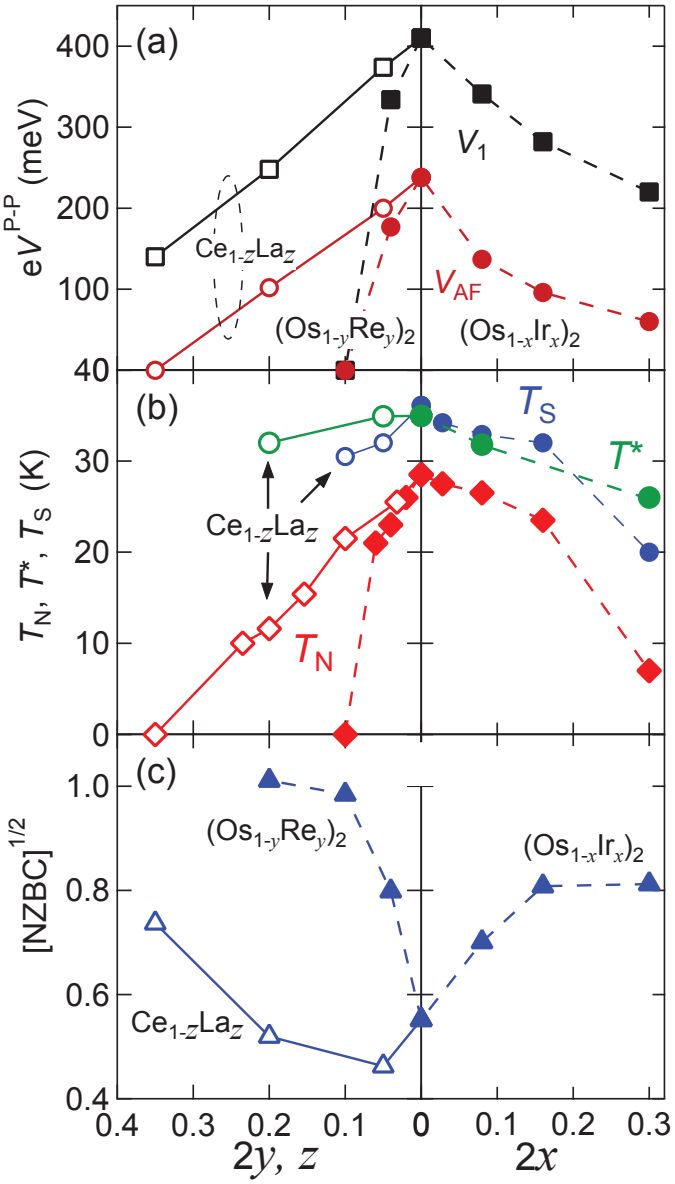

Figure 4.28: Variations of (a) gap widths V_1 and $V_{\rm AF}$, (b) characteristic temperature T^*, $T_{\rm S}$, and $T_{\rm N}$, and (c) $[{\rm NZBC}]^{1/2}$ at 4.4 K as functions of z, $2y$, and $2x$ in $Ce_{1-z}La_zOs_2Al_{10}$, $Ce(Os_{1-y}Re_y)_2Al_{10}$, and $Ce(Os_{1-x}Ir_x)_2Al_{10}$, respectively. $T_{\rm N}$ is the Néel temperature, T^* and $T_{\rm S}$ are the onset temperatures where $[{\rm NZBC}]^{1/2}$ and $S_{\rm b}$ decrease on cooling.

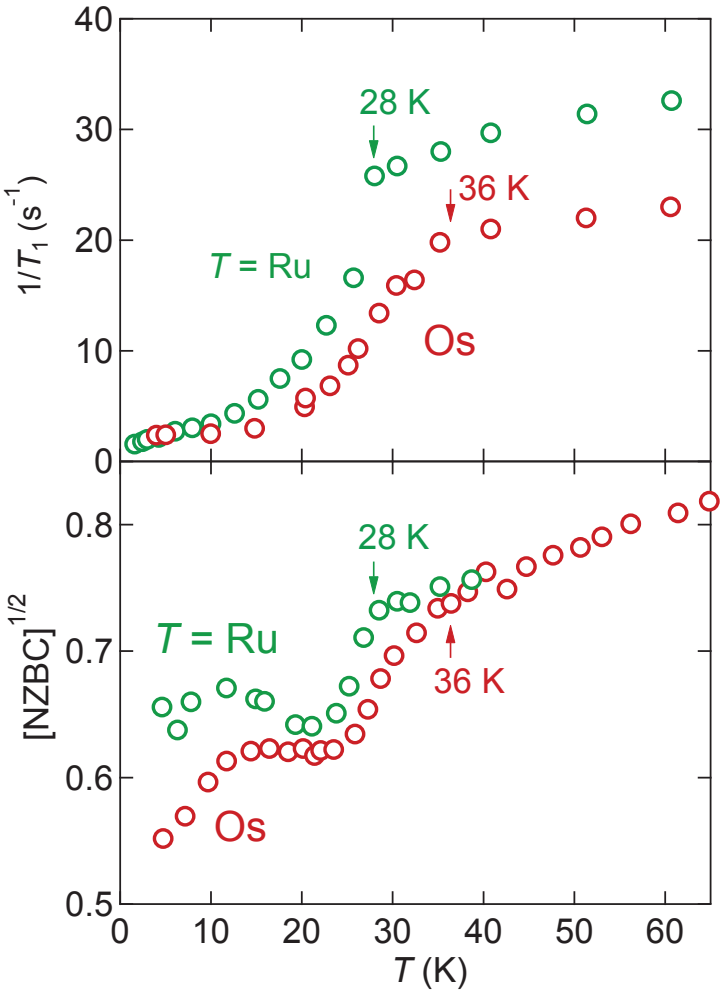

Figure 4.29: The temperature dependence of ^{27}Al nuclear spin-lattice relaxation rate [85, 86, 87] and $[\mathrm{NZBC}]^{1/2}$ for CeT_2Al_{10} (T = Ru and Os).The arrows denote the onset temperature T^* where$[\mathrm{NZBC}]^{1/2}$ decreases.

Chapter 5

Summary

The Ce-based compound $CeOs_2Al_{10}$ exhibits a thermal activation-type behavior in $\rho(T)$, and thus was classified into the Kondo semiconductor. It has been an enigma why this compound orders antiferromagnetically at a high temperature $T_N = 28.5$ K in spite of a small magnetic moment $\mu_{AF} = 0.3\ \mu_B$/Ce. The present study aimed to clarify the relation between the c-f hybridization gap and the unusual magnetic order in $CeOs_2Al_{10}$. For this purpose, we prepared La-, Re-, and Ir- substituted samples, i.e., $Ce_{1-z}La_zOs_2Al_{10}$, $Ce(Os_{1-y}Re_y)_2Al_{10}$, and $Ce(Os_{1-x}Ir_x)_2Al_{10}$, and performed the magnetic, transport, thermal, neutron scattering, and BJTS measurements.

The magnetization and neutron scattering measurements have revealed that the $4f/5d$-hole and $5d$-electron doping in $CeOs_2Al_{10}$ changes the c-f hybridization in very different ways. Specifically, the $4f$-hole doping does not alter the c-f hybridization at high temperatures. On the other hand, the $4f$ electron state becomes more delocalized by doping of $5d$ holes, but more localized by doping of $5d$ electrons. The opposite trend is also manifested in the thermopower $S(T)$. The doping of $4f/5d$ holes in $CeOs_2Al_{10}$ keeps the direction of μ_{AF} along the c axis, whereas doping of $5d$ electrons reorients μ_{AF} from the c axis to the a axis.

Despite of the significantly different effects in the three doped systems, we have observed common behaviors. Firstly, the γ value increases and both T_N and transport gap Δ concomitantly decrease. These observations imply that the doping of the holes/electrons in $CeOs_2Al_{10}$ induces in-gap states in the vicinity of E_F and destroys the transport gap. Secondly, the suppression of T_N is well correlated with that of transport gap as functions

of z, $2y$ and $2x$, suggesting that the hybridization gap is necessary for the unusual AFM order. However, it is noteworthy that the quasiparticle DOS for $CeOs_2Al_{10}$ has a pseudo-gap structure with a residual value at E_F. The finite $N(E_F)$ makes it difficult to judge the presence of the hybridization gap from the resistivity data. Therefore, we have conducted the BJTS studies to clarify the relation between hybridization gap and the unusual AFM orders.

In the differential conductances of the undoped compounds CeT_2Al_{10} (T = Fe, Ru, and Os) at 4.4 K, the presence of residual $N(E_F)$ has been confirmed as the finite normalized zero-bias conductance (NZBC), which is proportional to $[N(E_F)]^2$. The relation of $[\mathrm{NZBC}]^{1/2} = 0.7$ (T = Fe) > 0.4 (T = Ru) > 0.3 (T = Os) is consistent with that of Sommerfeld coefficient γ (mJ/K^{2}mol) = 18 (T = Fe) > 12 (T = Ru) > 7 (T = Os). Moreover, the temperature dependences of $[\mathrm{NZBC}]^{1/2}$ for T = Ru and Os exhibit downward bends below $T^* = 28$ and 36 K ($> T_N$), respectively. On cooling $CeFe_2Al_{10}$, two hybridization gaps successively manifest in the dI/dV spectra, while another gap V_{AF} develops below T_N in CeT_2Al_{10} (T = Ru and Os). The gap width of $V_{AF} = 160$ mV for T = Ru (T_N = 27.0 K) is smaller than that of $V_{AF} = 240$ mV for T = Os (T_N = 28.5 K).

In $Ce_{1-z}La_zOs_2Al_{10}$ with $z = 0.35$, the dI/dV spectrum remains V-shaped, whereas $\rho(T)$ no longer shows the semiconducting behavior. With increasing $2y$ in $Ce(Os_{1-y}Re_y)_2Al_{10}$, an upward cusp develops at $V = 0$, and then all gap structures disappear at $2y = 0.1$. In the region $0.08 \leq 2x < 0.3$ for $Ce(Os_{1-x}Ir_x)_2Al_{10}$, dI/dV exhibits an upward peak at $V = 0$ within the gap structures. On further increasing $2x$ up to 0.3, the peak vanishes while the V-shaped gap structure survives.

As noted above, doping of $4f/5d$ holes and $5d$ electrons in $CeOs_2Al_{10}$ changes the dI/dV spectra in very different ways although the suppressions of V_1 and V_{AF} are well correlated with that of T_N as functions of z, $2y$, and $2x$. Furthermore, in the doped region where V_1 and V_{AF} coexist, the temperature dependences of $[\mathrm{NZBC}]^{1/2}$ bend downward on cooling below T^* ($> T_N$), whose temperature agrees with the bending temperature in the thermopower $S_b(T)$. At the same temperature, anomalies are reported in the nuclear spin-lattice relaxation rate of ^{27}Al NQR and optical conductivity along the b axis. All the results indicate that the unusual AFM order in $CeOs_2Al_{10}$ is preceded by the decrease in $N(E_F)$ in the presence of the hybridization gap.

Acknowledgements

This work owes much to many collaborators. The encountering with them was fortunate for me. I feel highly honored to have worked during 5.5 years at the Magnetism Laboratory, Department of Advanced Sciences of Matter, Hiroshima University.

First and foremost, I would like to express the deepest gratitude to my supervisor Prof. T. Takabatake. Numerous helpful discussions as well as many enlightening suggestions have provided me with the helpful guidelines of my study. I learned from him the importances and interests of studying novel compounds, in addition, how to grasp the essence of physics. Without his persistent help, guideline, and encouragement, the thesis would not have materialized. I also wish to express great thanks to Profs. K. Umeo, T. Onimaru, K. Suekuni, T. Ekino, and A. Sugimoto for useful advise and fruitful discussions, leading to the present focus of my studies. They spent a lot of valuable time to assist me to perform the various measurements. Owing to their application, I could obtain a lot of experimental data to write this thesis. Furthermore, the study with the collaborators, Y. Yamada, Y. Okada, K. Hayashi, T. Takeuchi, and K. Yutani, was very pleasant because of their interesting and stimulative ideas. I appreciate their helpfulness on the large part of present study. The thesis could not be achieved without their helpfulness and enthusiasms.

I also acknowledge fruitful collaborations and valuable discussions with Profs. Y. Muro, H. Tanida, S. Kimura, T. Yokoya, Y. Ono, T. Yamada and D. T. Adroja. Their experimental data and theoretical works led me deeper understanding of the *c*-*f* hybridization gap and unusual antiferromagnetic order in Kondo semiconductors CeT_2Al_{10} (T = Fe, Ru, and Os) and substituted systems. A large part of the Introduction of this thesis is owed to their studies. In addition, special thanks to Mr. Y. Shibata for examining all the samples by the electron-probe microanalysis(EPMA) at the Cryogenics and Instru-

mental Analysis Division, Natural Science Center for Basic Research and Development (N-BARD), Hiroshima University.

During the five and half years of my Ph. D course, I have enjoyed my student life at Magnetism Laboratory. I would like to thank to the members of laboratory, K. T. Matsumoto, K. Wakiya, J. Izumi, K. Kajisa, N. Nagasawa, Y. Sugano, T. Iizuka, Y. Obayashi, Y. Yamada, H. Tanaka, K. Uenishi, F. Kim, T. Yamaguchi, Y. Yamane, Y. Kosaka, D. Watanabe, Y. Okada, K. Ohuka, K. Hashikuni, T. Takeuchi, G. B. Park, K. Miyoshi, T. Suenaga, M. Adachi, T. Ootaki, R. Yamada, S. Tsuda, K. Urashima, Y. Kusanose, S. Hara, R. Yamamoto, and Y. Arai. They create a harmonious and friendly atmosphere at the laboratory. In particular, my heartfelt appreciation goes to my friends, S. Sogabe, K. Niitani, Y. Shimada, K. Hayashi, and C. Yang. I could spend interesting and valuable time with them not only inside but also outside the laboratory. Last but not least, I would like to especially express my gratitude to my parents for their endless love and giving me the talents to achieve this accomplishment.

Bibliography

[1] J. Jensen and A. R. Mackintosh, *Rare Earth Magnetism Structures and Excitations* (Clarendon Press, Oxford, 1991).

[2] P. Misra, *Heavy - Fermion Systems* (Elsevier B. V., Oxford, 2008).

[3] A.C. Hewson, *The Kondo Problem to Heavy Fermions* (Cambridge University Press, Cambridge, 1993).

[4] P. Coleman, *Introdution to Many - Body Physics*, (Cambridge University Press, Cambridge, 2015.)

[5] C. Kittel, *Introduction to Solid State Physics*, 8th edition. (John Wiley and Sons, Hoboken, 2004).

[6] T. Takabatake, H. Iwasaki, G. Nakamoto, H. Fujii, H. Nakotte, F. R. de Boerb, and V. Sechovský, Physica B **183**, 108 (1993).

[7] M. D. Daybell, in *Magnetism*, Vol. V, ed. H. Suhl (Academic Press, New York and London, 1973).

[8] K. Samwer and K. Winzer, Z. Phys. B **25**, 269 (1976).

[9] S. Doniach, Physica B **91**, 231 (1977).

[10] Q. Z. Gao, E. Kanda, H. Kitazawa, M. Sera, T. Goto, T. Fujita, T. Suzuki, T. Fujimura, and T. Kasuya, J. of Magn. Magn. Mater., **47-48**, 69 (1985).

[11] B. Barbara, J. X. Boucherle, J. L. Buevoz, M. F. Rossignol, and J. Schweizer, Solid State Comm., **24**, 481 (1977).

[12] H. v. Löhneysen, M. Sieck, O. Stockert, and M. Waffenschmidt, Physica B, **223**, 471 (1996).

[13] J. D. Thompson, R. D. Parks, and H. Borges, J. Magn. Magn. Mater. **54-57**, 377 (1986).

[14] M. J. Besnus, P. Lehmann, and A. Meyer, J. Magn. Magn. Mater. **63-64**, 323 (1987).

[15] G. R. Stewart, Z. Fisk, and M. S. Wire, Phys. Rev. B **30**, 482(R) (1984).

[16] P. Gegenwart, Q. Si, and F. Steglich, Nat. Phys. **4**, 186 (2008).

[17] S. Hoshino and Y. Kuramoto, Phys. Rev. B **111**, 026401 (2013).

[18] K. H. J. Buschow and H. J. van Daal, Solid State Comm., **5**, 363 (1970).

[19] K. Kadowaki and S. B. Woods, Solid State Comm., **58**, 507 (1968).

[20] R. Settai, T. Takeuchi, and Y. Ōnuki, J. Phys. Soc. Jpn. **76**, 051003 (2007).

[21] T. Takabatake, G. Nakamoto, M. Sera, K. Kobayashi, H. Fujii, K. Maezawa, I. Oguro and Y. Matsuda, J. Phys. Soc. Jpn. **65**, Suppl. B 105 (1996).

[22] A. P. Reys, R. H. Heffner, P. C. Canfield, J. D. Thompson, and Z. Fisk, Phys. Rev. B **49**, 16321 (1994).

[23] K. Izawa, T. Suzuki, M. Kitaoka, T. Fujita, T. Takabatake, G. Nakamoto, and H. Fujii, J. Phys. Soc. Jpn. **65**, 3119 (1996).

[24] T. Takabatake, T. Yoshino, H. Tanaka, Y. Bando, H. Fujii, T. Fujita, H. Shiba, and T. Suzuki, Physica B **206-207**, 804 (1995).

[25] T. Sasakawa, T. Suemitsu, T. Takabatake, Y. Bando, K. Umeo, M. H. Jung, M. Sera, T. Suzuki, T. Fujita, M. Nakajima, K. Iwasa, M. Kohgi, Ch. Paul, St. Berger, and E. Bauer, Phys. Rev. B **66**, 041103(R) (2002).

[26] M. Matsumura, T. Sasakawa, T. Takabatake, S. Tsuji, H. Tou, and M. Sera, J. Phys. Soc. Jpn. **72**, 1030 (2003).

[27] P. S. Riseborough, Adv. Phys. **49**, 257 (2000).

[28] T. Takabatake, F. Iga, T. Yoshino, Y. Echizen, K. Katoh, K. Kobayashi, M. Higa, N. Shimizu, Y. Bando, G. Nakamoto, H. Fujii, K. Izawa, T. Suzuki, T. Fujita, M. Sera, M. Hiroi, K. Maezawa, S. Mock, H. v. Lohneysen, A. Brückl, K. Neumaier, and K. Andres, J. Magn. Mag. Mater. **177-181**, 277 (1998).

[29] T. Takabatake, T. Sasakawa, J. Kitagawa, T. Suemitsu, Y. Echizen, K. Umeo, M. Sera, Y. Bando, Physica B **328**, 53 (2003).

[30] M. F. Hundley, P. C. Canfield, J. D. Thompson, Z. Fisk, and J. M. Lawrence, Phys. Rev. B **42**, 6842 (1990).

[31] H. F. Hundley, P. C. Canfield, J. D. Thompson and Z. Fisk, Phys. Rev. B **50**, 18142 (1994).

[32] M. Kasaya, F. Iga, K. Negishi, S. Nakai, and K. Kasuya, J. Magn. Magn. Mater. **31-34**, 437 (1983).

[33] F. Iga, N. Shimizu, and T. Takabatake, J. Magn. Magn. Mater. **177-181**, 337 (1998).

[34] A. Menth, E. Buehler, and T. H. Geballe, Phys. Rev. Lett. **22**, 295 (1969).

[35] J. C. Cooly, M. C. Aronson, Z. Fisk, and P. C. Canfield, Phys. Rev. Lett. **74**, 1629 (1995).

[36] M. Kasaya, K. Katoh, and K. Takegahara, Solid State Comm. **78**, 797 (1991).

[37] E. D. Bauer, A. Slebarski, E. J. Freeman, C. Sirvent and M. B. Maple, J. Phys.: Cond. Matt. **13**, 5183 (2001).

[38] H. Ikeda and K. Miyake, J. Phys. Soc. Jpn. **65**, 1769 (1996).

[39] M. Kyogaku, Y. Kitaoka, H. Nakamura, K. Asayama, T. Takabatake, F. Teshima, and H. Fujii, J. Phys. Soc. Jpn. **59**, 1728 (1990).

[40] K. Nakamura, Y. Kitaoka, K. Asayama, T. Takabatake, H. Tanaka, and H. Fujii, J. Phys. Soc. Jpn. **63**, 433 (1994).

[41] S. Nishigori, H. Goshima, T. Suzuki, T. Fujita, G. Nakamoto, H. Tanaka, T. Takabatake, and H. Fujii, J. Phys. Soc. Jpn. **65**, 2614 (1996).

[42] H. Kumigashira, T. Sato, T. Yokoya, T. Takahashi, S. Yoshii, and M. Kasaya, Phys. Rev. Let. **82**, 1943 (1999).

[43] T. Susaki, Y. Takeda, M. Arita, K. Mamiya, A. Fujimori, K. Shimada, H. Namatame, M. Taniguchi, N. Shimizu, F. Iga, and T. Takabatake, Phys. Rev. Let. **82**, 992 (1999).

[44] M. Matsunami, H. Okamura, T. Nanba, T. Suemitsu, T. Yoshino, T. Takabatake, Y. Ishikawa, and H. Harima, J. Phys. Soc. Jpn. **71**, 291 (2002).

[45] H. Okamura, S. Kimura, H. Shinozaki, T. Nanba, F. Iga, N. Shimizu, and T. Takabatake, Phys. Rev. B. **58**, R7496 (1998).

[46] T. Ekino, T. Takabatake, H.Tanaka, and H. Fujii, Phys. Rev. Let. **75**, 4262 (1995).

[47] D. N. Dacydov, S. Kambe, A. G. M . Jansen, P. Wyder, N. Wilson, G. Lapertot, and J. Flouquet, Phys. Rev. B. **55**, R7299 (1997) .

[48] T. Ekino, T. Takasaki, T. Suemitsu, T. Takabatake, and H. Fujii, Physica B **312-313**, 221 (2002).

[49] T. Ekino, H. Umeda, J. Klijn, F. Iga, T. Takabatake, and H. Fujii, Physica B **281-282**, 278 (2000).

[50] M. Miyazawa and K. Yamada, J. Phys. Soc. Jpn **72**, 2033 (2003).

[51] J. Moreno and P. Coleman, Phys. Rev. Lett. **84**, 342 (2000).

[52] T. Yamada and Y. Ono, Phys. Rev. B **85**, 165114 (2012).

[53] Y. Echizen, K. Umeo, S. Hamashima, T. Fujita, T. Takabatake, N. Kobayashi, and I. Oguro, Solid State Comm. **115**, 587 (2000).

[54] K. Kobayashi, T. Takabatake, G. Nakamoto, M. Higa, T. Yoshino, H. Fujii, and M. Sera, Physica B **230**, 676 (1997).

[55] A. Brückl, K. Neumaier, Ch. Probst, K. Andres, S. J. Flaschin, A. Kratzer, G. M. Kalvius, and T. Takabatake, Physica B **240**, 199 (1997).

[56] Y. Bando, Y. Echizen, T. Takabatake, Physica B **281 & 282** 294 (2000).

[57] J. Sakurai, A. Iwasaki, Q. Lu, D. Huo, Y. Ishikawa, Jesuś Rodríguez Fernández, and Jóse Carlos Gómez Sal, J. Phys. Soc. Jpn **71**, 2829 (2002).

[58] T. Ohyama, J. Sakurai, and K. Komura, J. Magn. Magn. Mater. **63**, 581 (1987).

[59] D.T. Adroja, B. D. Rainford, J. M. de Teresa, A. del. Moral, M. R. Ibarra, K. S. Knight, Phys. Rev. B **52**, 12790 (1995).

[60] Y. Bando, T. Takabatake, T. Tanaka, H. Iwasaki, H. Fujii, S. K. Malik, Physica B **194 & 196** 1179 (1994).

[61] T. Ekino, H. Miyaoka, T. Sasakawa, T. Takabatake, and A. M. Gabovich, Physica B **383**, 26 (2006).

[62] T. Mutou, Phys. Rev. B. **64**, 165103 (2001).

[63] P. S. Riseborough and S. G. Magalhaes, J. Magn. Magn. Mater. **400**, 3 (2016).

[64] P. Schlottmann, Phys. Rev. B. **46**, 998 (1992).

[65] P. S. Riseborough, Phys. Rev. B. **68**, 235213 (2003).

[66] A. M. Strydom, Physica B **404**, 2981 (2009).

[67] V. M. T. Thiede, T. Ebel, and W. Jeitschko, J. Mater. Chem. **8**, 125 (1998).

[68] M. Sera, D. Tanaka, H. Tanida, C. Moriyoshi, M. Ogawa, Y. Kuroiwa, T. Nishioka, M. Matsumura, J. Kim, N. Tsujo, and M. Takata, J. Phys. Soc. Jpn **82**, 024603 (2013).

[69] D. T. Adroja, A. D. Hillier, Y. Muro, T. Takabatake, A. M. Strydom, A. Bhattacharyya, A. Daoud-Aladin, and J. W. Taylor, Phys. Scr. **88**, 068505 (2013).

[70] K. Hanzawa, J. Phys. Soc. Jpn. **79**, 043710 (2010).

[71] T. Nishioka, Y. Kawamura, T. Takesaka, R. Kobayashi, H. Kato, M. Matsumura, K. Kodama, K. Matsubayashi, and Y. Uwatoko, J. Phys. Soc. Jpn. **78**, 123705 (2009).

[72] Y. Muro, J. Kajino, K. Umeo, K. Nishimoto, R. Tamura, and T. Takabatake, Phys. Rev. B **81**, 214401 (2010).

[73] H. Tanida, D. Tanaka, M. Sera, C. Moriyoshi, Y. Kuroiwa, T. Takesaka, T. Nishioka, H. Kato, and M. Matsumura, J. Phys. Soc. Jpn. **79**, 083701 (2010).

[74] H. Tanida, Y. Nonaka, D. Tanaka, M. Sera, T. Nishioka, and M. Matsumura, Phys. Rev. B **86**, 085144 (2012).

[75] Y. Muro, K. Motoya, Y. Saiga, and T. Takabatake, J. Phys. Soc. Jpn. **78**, 083707 (2009).

[76] J. Kawabata, T. Takabatake, K. Umeo, and Y. Muro, Phys. Rev. B **89**, 094404 (2014).

[77] H. Tanida, M. Nakamura, M. Sera, A. Kondo, K. Kindo, T. Nishioka, and M. Matsumura, J. Phys. Soc. Jpn. **83**, 084708 (2009).

[78] D. D. Khalyavin, A. D. Hillier, D. T. Adroja, A. M. Strydom, P. Manuel, L. C. Chapon, P. Peratheepan, K. Knight, P. Deen, C. Ritter, Y. Muro, and T. Takabatake, Phys. Rev. B **82**, 100405(R) (2010).

[79] F. Strigari, M. Sundermann, Y. Muro, K. Yutani, T. Takabatake, K.-D. Tsuei, Y. F. Liao, A. Tanaka, P. Thalmeier, M.W. Haverkort, L.H. Tjeng, and A. Severing, J. Electron Spectr. Rel. Phenom, **199**, 56 (2015).

[80] F. Strigari, T. Willers, Y. Muro, K. Yutani, T. Takabatake, Z. Hu, S. Agrestini, C. Y. Kuo, Y. Y. Chin, H. J. Lin, T. W. Pi, C. T. Chen, E. Weschke, E. Schierle, A. Tanaka, M. W. Haverkort, L. H. Tjeng, and A. Severing, Phys. Rev. B **87**, 125119 (2013).

[81] F. Strigari, T. Willers, Y. Muro, K. Yutani, T. Takabatake, Z. Hu, Y.-Y. Chin, S. Agrestini, H.-J. Lin, C. T. Chen, A. Tanaka, M. W. Haverkort, L. H. Tjeng, and A. Severing, Phys. Rev. B **86**, 081105(R) (2012).

[82] T. Kikuchi, S. Hoshino, and Y. Kuramoto, J. Phys. Soc. Jpn. **83**, 114706 (2014).

[83] D. T. Adroja, A. D. Hillier, P. P. Deen, A. M. Strydom, Y. Muro, J. Kajino, W. A. Kockelmann, T. Takabatake, V. K. Anand, J. R. Stewart, and J. Taylor, Phys. Rev. B **82**, 104405 (2010).

[84] H. Kato, R. Kobayashi, T. Takesaka, T. Nishioka, M. Matsumura, K. Kaneko, and N. Metoki, J. Phys. Soc. Jpn. **80**, 073701 (2011).

[85] H. Kato, T. Takesaka, R. Kobayashi, T. Noshioka, M. Matsumura, Y. Tokunaga, and S. Kambe, J. Phys.: Conf. Ser. **273**, 012037 (2011).

[86] M. Matsumura, T. Inagaki, H. Kato, T. Nishioka, H. Tanida, and M. Sera, J. Phys.: Conf. Ser., **400**, 032052 (2012).

[87] M. Matsumura, N. Tomita, S. Tanimoto, Y. Kawamura, R. Kobayashi, H. Kato, T. Nishioka, H. Tanida, and M. Sera, J. Phys. Soc. Jpn. **82**, 023702 (2013).

[88] Y. Muro, J. Kajino, T. Onimaru, and T. Takabatake, J. Phys. Soc. Jpn. **80**, SA021 (2011).

[89] G. Morrison, N. Haldoaarachchige, D. P. Young and J. Y. Chan, J. Phys.: Cond. Matt. **24**, 356002 (2012).

[90] H. Miwa, Prog. Theor. Phys. **28**, 208 (1962).

[91] D. D. Khalyavin, A. D. Hillier, D. T. Adroja, A. M. Strydom, P. Manuel, L. C. Chapon, P. Peratheepan, K. Knight, P. Deen, C. Ritter, Y. Muro, and T. Takabatake, Phys. Rev. B **82**, 100405(R) (2010).

[92] N. B. Brandt and V. V. Moshchalkov, Adv. Phys. **33**, 373 (1984).

[93] J. Kawabata, T. Ekino, Y. Yamada, Y. Sakai, A. Sugimoto, Y. Muro, and T. Takabatake, Phys. Rev. B **92**, 201113 (2015).

[94] T. Ishiga, T. Wakita, R. Yoshida, H. Okazaki, K. Tsubota, M. Sunagawa, K. Uenaka, K. Okada, H. Kumigashira, M. Oshima, K. Yutani, Y. Muro, T. Takabatake, Y. Muraoka, and T. Yokoya, J. Phys. Soc. Jpn. **83**, 094717 (2014).

[95] S. Kimura, T. Iizuka, H. Miyazaki, A. Irizawa, Y. Muro, and T. Takabatake, Phys. Rev. Lett. **106**, 056404 (2011).

[96] S. Kimura, T. Iizuka, H. Miyazaki, T. Hajiri, M. Matsunami, T. Mori, A. Irizawa, Y. Muro, J. Kajino, and T. Takabatake, Phys. Rev. B. **84**, 165125 (2011).

[97] K. Umeo, T. Ohsuka, Y. Muro, J. Kajino, and T. Takabatake, J. Phys. Soc. Jpn. **80**, 064709 (2012).

[98] H. Tanida, Y. Nonaka, D. Tanaka, M. Sera, T. Nishioka, and M. Matsumura, Phys. Rev. B. **86**, 085144 (2012).

[99] H. Tanida, D. Tanaka, M. Sera, C. Moriyoshi, Y. Kuroiwa, T. Takesaka, T. Nishioka, H. Kato, and M. Matsumura, J. Phys. Soc. Jpn. **79**, 063709 (2010).

[100] D. T. Adroja, A. D. Hillier, C. Ritter, A. Bhattacharyya, D. D. Khalyavin, A. M. Strydom, P. Peratheepan, B. Fåk, M. M. Koza, J. Kawabata, Y. Yamada, Y. Okada, Y. Muro, T. Takabatake, and J. W. Taylor, Phys. Rev. B **92**, 094425 (2015).

[101] H. Tanida, H. Nohara, M. Sera, T. Nishioka, M. Matsumura, and R. Kobayashi, Phys. Rev. B. **90**, 165124 (2014).

[102] A. Bhattacharyya, D. D. Khalyavin, D. T. Adroja, A. M. Strydom, A. D. Hillier, P. Manuel, T. Takabatake, J. W. Taylor, and C. Ritter, Phys. Rev. B. **90**, 174412 (2014).

[103] R. Kobayashi, Y. Ogane, D. Hirai, T. Nishioka, M. Matsumura, Y. Kawamura, K. Matsubayashi, Y. Uwatoko, H. Tanida, and M. Sera, J. Phys. Soc. Jpn. **82**, 093702 (2013).

[104] H. Tanida, H. Nohara, F. Nakagawa, K. Yoshida, M. Sera, and T. Nishioka, Phys. Rev. B. **94**, 165137 (2016).

[105] R. Kobayashi, K. Kaneko, K. Saito, J. M. Mignot, G. André, J. Robert, S. Wakimoto, M. Matsuda, S. Chi, Y. Haga, T. D. Matsuda, E. Yamamoto, T. Nishioka, M. Matsumura, H. Tanida, and M. Sera, J. Phys. Soc. Jpn. **83**, 104707 (2014).

[106] K. Yoshida, R. Okubo, H. Tanida, T. Matsumura, M. Sera, T. Nishioka, M. Matsumura, C. Moriyoshi, and Y. Kuroiwa, Phys. Rev. B **91**, 235124 (2015).

[107] S. Kimura, H. Tanida, M. Sera, Y. Muro, T. Takabatake, T. Nishioka, M. Matsumura, and R. Kobayashi, Phys. Rev. B. **91**, 241120(R) (2015).

[108] Y. Okada, J. Kawabata, Y. Yamada, Y. Muro, and T. Takabatake, J. Phy.: Conf. Ser., in press.

[109] D. D. Khalyavin, D. T. Adroja, P. Manuel, J. Kawabata, K. Umeo, T. Takabatake, and A. M. Strydom, Phys. Rev. B **88**, 060403(R) (2013).

[110] D. D. Khalyavin, D. T. Adroja, A. Bhattacharyya, A. D. Hillier, P. Manuel, A. M. Strydom, J. Kawabata, and T. Takabatake, Phys. Rev. B **89**, 064422 (2014).

[111] A. Bhattacharyya, D. T. Adroja, A. M. Strydom, J. Kawabata, T. Takabatake, A. D. Hillier, V. Garcia Sakai, J. W. Taylor, and R. I. Smith, Phys. Rev. B **90**, 174422 (2014).

[112] Y. Yamada, J. Kawabata, T. Onimaru, and T. Takabatake, J. Phys. Soc. Jpn. **84**, 084705 (2015).

[113] J. Kawabata, T. Ekino, Y. Yamada, Y. Sakai, A. Sugimoto, Y. Muro, and T. Takabatake, Phys. Rev. B **92**, 201113 (2015).

[114] J. Kawabata, T. Ekino, Y. Yamada, A. Sugimoto, Y. Muro, and T. Takabatake, J. Phys.: Conf. Ser., submitted.

[115] F. Izumi and T. Ikeda, Mater. Sci. Forum, **321-324**, 198 (2000).

[116] Quantum Design, San Diego, CA 92121-1311, *QuantumDesign* MPMS MultiVu Application User's Manual (2004).

[117] Quantum Design, San Diego, CA 92121-1311, *QuantumDesign* PPMS AC Measurement System Option User's Manual (2009).

[118] Quantum Design, San Diego, CA 92121-1311, *QuantumDesign* PPMS Heat Capacity Option User's Manual (2009).

[119] J. M. Ziman,*Electrons and Phonons*(Oxford University press, 1960).

[120] A. A. Valamov, V. S. Egoror, and A. V. Pantsulaya, Adv. Phys. **38**, 469 (1989).

[121] E. Mun, S. L. Bud'ko, M. S. Torikachvili, P. C. Canfield, Meas. Sci. Technol. **21** 055104 (2010).

[122] E. L. Wolf, *Principles of Electron Tunneling Spectroscopy*, 2nd ed. (Oxford University Press, New York, 2012).

[123] B. Cornut and B. Coqblin, Phys. Rev. B **5**, 4541 (1972).

[124] J. Sakurai, K. Hasegawa, A. A. Menovsky, and J. Schweizer, Solid State Commun. **97**, 689 (1996). 31)

[125] C. Bareille, F. L. Boariu, H. Schwab, P. Lejay, F. Reinert, and A. F. Santander-Syro, Nat. Commun. **5**, 4326 (2014).

[126] W. C. Lee, W. K. Park, H. Z. Arham, L. H. Green, and P. Phillips, Proc. Natl. Acad. Sci. U.S.A. **112**, 651 (2015).

[127] C. J. Muller, J. M. van Ruitenbeek, and L. J. de Jongh, Physica C **191**, 485 (1992).

[128] K. Flachbart, K. Gloos, E. Konovalova, Y. Paderno, M. Reiffers, P. Samuely, and P. Svec, Phys. Rev. B **64**, 085104 (2014).

[129] T. Ekino, H. Umeda, K. Katoh, T. Takabatake, and H. Fujii, J. Magn. Magn. Mater. **177-181**, 379 (1998).

[130] A. Maldonado, H. Suderow, S. Vieira, D. Aoki, and J. Flouquet, J. Phys.: Cond. Matt. **24** 475602 (2012).

[131] G. Motoyama, S. Ogawa, K. Matsubayashi, K. Fujiwara, K. Miyoshi, S. Nishigori, T. Mutou, A. Yamaguchi, A. Sumiyama, and Y. Uwatoko, Phys. Proc. **75**, 296 (2015).

公表論文

(1) Doping effects on the hybridization gap and antiferromagnetic order in the Kondo semiconductor $CeOs_2Al_{10}$ studied by break-junction experiments,
J. Kawabata, T. Ekino, Y. Yamada, Y. Okada, A. Sugimoto, Y. Muro, and T. Takabatake,
Physical Review B **95**, 035144 /1-9 (2017)

(2) Interplay between hybridization gaps and antiferromagnetic gap in the hole-doped Kondo semiconductor $Ce(Os_{1-y}Re_y)_2Al_{10}$,
J. Kawabata, T. Ekino, Y. Yamada, A. Sugimoto, Y. Muro, and T. Takabatake,
Journal of Physics: Conference Series **807**, 012008 /1-6 (2017).

(3) Hybridization gaps and antiferromagnetic gap in the Kondo semiconductors CeT_2Al_{10} (T = Fe and Os) observed by break-junction tunneling spectroscopy,
J. Kawabata, T. Ekino, Y. Yamada, Y. Sakai, A. Sugimoto, Y. Muro, and T. Takabatake,
Physical Review B **92**, 201113(R) /1-5 (2015).

(4) Suppression of antiferromagnetic order and hybridization gap by electron and hole doping in the Kondo semiconductor $CeOs_2Al_{10}$,
J. Kawabata, T. Takabatake, K. Umeo, and Y. Muro,
Physical Review B **89**, 094404 /1-7 (2014).

(5) Transition from a Kondo semiconducting antiferromagnet to a heavy-fermion antiferromagnet in $Ce(Os_{1-x}Ir_x)_2Al_{10}$,
J. Kawabata, K. Yutani, K. Umeo, T. Takabatake, and Y. Muro,
Journal of Physical Society Conference Proceedings **3**, 012023 /1-6 (2014).

参考論文

(1) Uniaxial pressure effects on the unusual antiferromagnetic transition in the Kondo semiconductor $CeOs_2Al_{10}$,
K. Hayashi, K. Umeo, Y. Yamada, J. Kawabata, Y. Muro, and T. Takabatake,
Journal of Physics: Conference Series **807**, 022002 /1-6 (2017).

(2) Dilution effects on the antiferromagnetic Kondo semiconductor $CeOs_2Al_{10}$,
Y. Okada, J. Kawabata, Y. Yamada, Y. Muro, and T. Takabatake,
Journal of Physics: Conference Series **807**, 022003 /1-5 (2017).

(3) Doping effects on the electronic structure of an anisotropic Kondo semiconductor $CeOs_2Al_{10}$: An optical study with Re and Ir substitution,
S. Kimura, H. Takao, J. Kawabata, Y. Yamada, and T. Takabatake,
Journal of the Physical Society of Japan **85**, 123705 /1-4 (2016).

(4) Effect of Si substitution on the antiferromagnetic ordering in the Kondo semiconductor $CeRu_2Al_{10}$,
K. Hayashi, Y. Muro, T. Fukuhara, J. Kawabata, T. Kuwai, and T. Takabatake,
Journal of the Physical Society of Japan **85**, 034714 /1-4 (2016).

(5) Contrasting effect of La substitution on the magnetic moment direction in the Kondo semiconductors $Ce\mathit{T}_2Al_{10}$ (T = Ru, Os),
D. T. Adroja, A. D. Hillier, C. Ritter, A. Bhattacharyya, D. D. Khalyavin, A. M. Strydom, P. Peratheepan, B. Fåk, M. M. Koza, J. Kawabata, Y. Yamada, Y. Okada, Y. Muro, T. Takabatake, and J. W. Taylor,
Physical Review B **92**, 094425 /1-10 (2015).

(6) Anisotropic thermopower of the antiferromagnetic Kondo semiconductor $CeOs_2Al_{10}$ doped with 5d electrons and holes,
Y. Yamada, J. Kawabata, T. Onimaru, and T. Takabatake,
Journal of the Physical Society of Japan **84**, 084705 /1-5 (2015).

(7) Anisotropic chemical pressure effect on the antiferromagnetic Kondo semiconductor $Ce(Ru_{1-x}Fe_x)_2Al_{10}$,
K. Hayashi, Y. Muro, T. Fukuhara, T. Kuwai, J. Kawabata, and T. Takabatake,
Physics Procedia **75**, 121-126 (2015).

(8) Contrasting carrier doping effects in the Kondo insulator $CeOs_2Al_{10}$: The influential role of *c-f* hybridization in spin-gap formation,
A. Bhattacharyya, D. T. Adroja, A. M. Strydom, J. Kawabata, T. Takabatake, A. D. Hillier, V. G. Sakai, J. W. Taylor, and R. I. Smith,
Physical Review B **90**, 174422 /1-9 (2014).

(9) Effects of Ga and Si substitutions for Al in $CeRu_2Al_{10}$ on the unusual antiferromagnetic order in the Kondo semiconducting state,
Y. Muro, K. Hida, T. Fukuhara, J. Kawabata, K. Yutani, and T. Takabatake,
Journal of Physical Society Conference Proceedings **3**, 012017 /1-7 (2014).

(10) Magnetic ordering with reduced cerium moments in hole-doped $CeOs_2Al_{10}$,
D. D. Khalyavin, D. T. Adroja, A. Bhattacharyya, A. D. Hillier, P. Manuel, A. M. Strydom, J. Kawabata, and T. Takabatake,
Physical Review B **89**, 064422 /1-5 (2014).

(11) Change of magnetic ground state by light electron doping in $CeOs_2Al_{10}$,
D. D. Khalyavin, D. T. Adroja, P. Manuel, J. Kawabata, K. Umeo, T. Takabatake, and A. M. Strydom,
Physical Review B **88**, 060403(R) /1-4 (2013).